A NUMERICAL STUDY OF AIRFLOW THROUGH HUMAN UPPER AIRWAYS

ZHU JIANHUA

NATIONAL UNIVERSITY OF SINGAPORE

2012

A NUMERICAL STUDY OF AIRFLOW THROUGH HUMAN UPPER AIRWAYS

ZHU JIANHUA
(B.ENG., Shanghai Jiao Tong University)

A THESIS SUBMITTED

FOR THE DEGREE OF DOCTOR OF PHILOSOPHY

DEPARTMENT OF MECHANICAL ENGINEERING

NATIONAL UNIVERSITY OF SINGAPORE

2012

DECLARATION

I hereby declare that this thesis is my original work and it has been written by me in its entirety. I have duly acknowledged all the sources of information which have been used in the thesis.

This thesis has also not been submitted for any degree in any university previously.

Zhu Jianhua

Zhu Jianhua
Date: 25th Jul 2012

ACKNOWLEDGEMENT

I would like to express my deepest gratitude to my supervisors A/Prof. H. P. Lee and A/Prof. K. M. Lim for their invaluable direction, support and encouragement throughout my PhD studies.

I would like to thank Dr. De Yun Wang, Dr. Shu Jin Lee, Dr. Xiao Bing Chen and Dr. Bruce R. Gordon for the interesting and insightful discussion on human upper airway pathophysiologies.

I would also like to thank Kwong Ming Tse, Shi Feng Guo, Yi Lin Liu, Han Zhuang, Yong Chin Seow, Arpan Gupta, my best friends in Singapore, for the unforgettable happiness and hardship shared with me.

Finally, I want to dedicate all my success to my wife and parents for their constant support and encouragement in my academic pursuits in National University of Singapore.

TABLE OF CONTENTS

SUMMARY

As a rather complicated component, there are few non-invasive techniques, either for diagnosis or for research, to examine respiratory physiopathologies in human upper airway. Recently, the combination of numerical methods with computerized tomography (CT) and magnetic resonance imaging (MRI) scans, has been proven to be a valid and efficient tool to study human respiratory mechanisms (see Keyhani et al., 1995). Therefore, this PhD study aims to investigate airflow patterns in human upper airway using numerical simulation as a non-invasive approach.

Firstly, we evaluated the effects of different nasal morphologies among ethnic groups on nasal airflow. Nasal models of three individuals, one Caucasian, one Chinese and one Indian, were reconstructed to simulate and compare inspirational nasal airflow patterns using computational fluid dynamics (CFD) simulation. The results show that more airflow tended to pass through the middle passage of the nasal airway in the Caucasian model, and through the inferior portion in the Indian model. The anterior nasal structures were associated with the direction of airflow and the production of vortexes.

Furthermore, the influences of other factors that may alter upper airway and airflow were evaluated using CFD. For example, nasal models of pre- and post-operative conditions of a patient with orbito-maxillary bone fracture were reconstructed, to investigate effects of bone fracture and surgical intervention on nasal morphology and airflow. The operation was found to significantly restore the collapse of the left nasal airway induced by the fracture, with decreased nasal resistance, more even flow partitioning between left and right airways and more continuous streamlines. In addition, the effects of deviated external noses on nasal airflow were also studied with three typical models (one with S-shaped, one with C-shaped and one with slanted noses). It was found that the deviation collapsed one of the anterior airways accompanying with internal nasal blockage along the turbinates, which increased nasal resistance, produced vortexes around the anterior nasal roof and disturbed the streamlines. The S-shaped deviation caused the largest nasal resistance, followed by slanted and C-shaped cases.

Despite folded nasal airway, the human maxillary sinus, shielded by surrounding structures, is more difficult to approach. The natural ostium (NO) is the only connection between nasal airway and sinus in the absence of accessory ostium (AO). A nasal model of a subject with two left AOs and one right AO was constructed, thereafter compared to an identical control model with all AOs sealed, to study the effects of AO on maxillary sinus ventilation. The CFD simulation demonstrated that AOs markedly increased sinus airflow rates and altered sinus air circulation patterns.

Finally, a fluid-structure interaction model was prepared to investigate the interaction between respiratory airflow and soft palate in human pharynx during calm respiration. The results show that the soft palate was almost stationery during inspiration, and moved towards the posterior pharyngeal wall during expiration. The posterior movement tendency of soft palate could be one of the causes of expiratory occlusion of human upper airway during sleep.

LIST OF FIGURES

LIST OF TABLES

NOMENCLATURE

English alphabets

A	area of cross section
D_H	equivalent hydraulic diameter
$\vec{e}$	velocity strain tensor of airflow
E	Young's modulus
g	gap function between two points of two contact surfaces
G	shear modulus
$\vec{I}$	second order unit tensor
k	turbulent kinetic energy
$\vec{n}$	normal of cross section
p	pressure of air
P	perimeter of cross section
Q_A	airflow rate through cross section A
R	flow resistance

Re	Reynolds number
R^d	scaled displacement residual over the FSI interface in ADINA
R^f	scaled force residual over the FSI interface in ADINA
R^Φ	scaled residual for variable Φ in FLUENT
S	modulus of the mean rate-of-strain tensor
t	time
$\vec{u}$	velocity vector
$\vec{u}_f$	displacement vector of FSI interface in fluid computational domain
v	displacement of structure
$\vec{v}_s$	displacement vector of FSI interface in structural computational domain
V	volume flow rate
$\vec{w}$	moving coordinate velocity
Δd	increment of displacement during FSI simulation
Δp	pressure drop

Greek symbols

δ	Kronecker's delta
ε	strain tensor
λ	normal contact force function on two contact surfaces
μ	dynamic viscosity
μ_t	turbulent viscosity
ν	Poisson's ratio
ρ	density of ambient air
ρ'	density of structure
σ	Cauchy stress tensor
τ	stress tensor of fluid
ω	specific dissipation rate

ACRONYMS

ABD	Abdominal
ALE	Arbitrary Lagrangian Eulerian
AO	Accessory Ostium
CFD	Computational Fluid Dynamics
CSA	Cross Sectional Area
CT	Computerized Tomography
DNS	Direct Numerical Simulation
FEM	Finite Element Method
FSI	Fluid/Structure Interaction
FVM	Finite Volume Method
LES	Large Eddy Simulation
LRN	Low Reynolds Number
MCA	Minimum Cross Sectional Area
MRI	Magnetic Resonance Imaging

NO	Natural Ostium
ORIF	Open Reduction Internal Fixation
OSAHS	Obstructive Sleep Apnea-hypopnea Syndrome
PNIF	Peak Nasal Inspirational Flow
RANS	Reynolds averaged Navier-Stokes
RC	Rib Cage
SST	Shear Stress Transport
SVR	Surface-area-volume Ratio

Chapter 1 Introduction

1.1 Background

The human upper airways connect the ambient environment and the lower portion of the human respiratory system, providing human beings with warm and humidified air, protecting them from deleterious particles, viruses and bacteria, and enabling them with olfaction. The dysfunctions of human upper airways, however, account for a lot of prevalent pathologies such as allergy, rhinitis and airway obstruction. Most of these functions and pathologies are closely associated with upper airway airflow. Although the concepts of various upper airway physiopathologies can be established from the perspective of otolaryngology, the detailed mechanisms of upper airway airflow have not yet received a great deal of attention due to the complexity of the upper airway morphology and limited experimental technologies. Recently, with the development of computer resources, researchers began to look thoroughly into the detailed airflow patterns and airflow-related fields using numerical simulations (Chen et al., 2011; Chen et al., 2012; Ge et al., 2012; Hahn et al., 1993; Jeong et al., 2007; Na et al., 2012; Subramaniam et al., 1998). The numerical simulations rely on an accurate geometric model representing the upper airway morphology, which will be introduced below.

1.1.1 Morphology of human nasal cavity and pharynx

The morphology of human nasal cavity is quite complex compared to the pharynx. As shown in Figure 1.1, the nasal cavity is separated into two nasal airways by a fin named nasal septum. Along each of the nasal airways lie three curved bones (the inferior, the middle and the superior turbinates). The two separated airways merge near the end of the turbinates towards the pharynx. At the superior of the airway, the olfactory receptors are located, which equips human beings with sense of smell. The cross section of the nasal airway is usually recognized as different meatuses, such as inferior meatus, middle meatus, superior meatus and common meatus. As divided by the three turbinates, the entire passage is quite narrow (less than 2 mm in width compared to 8 cm in length). The narrowest area along the nasal cavity is usually around the nasal valve region located right after the nostrils. In addition to the main passage of the nasal airway, there are extra lumens named maxillary sinuses in which the airflow ventilation is considered to be particularly low (Rennie et al., 2011).

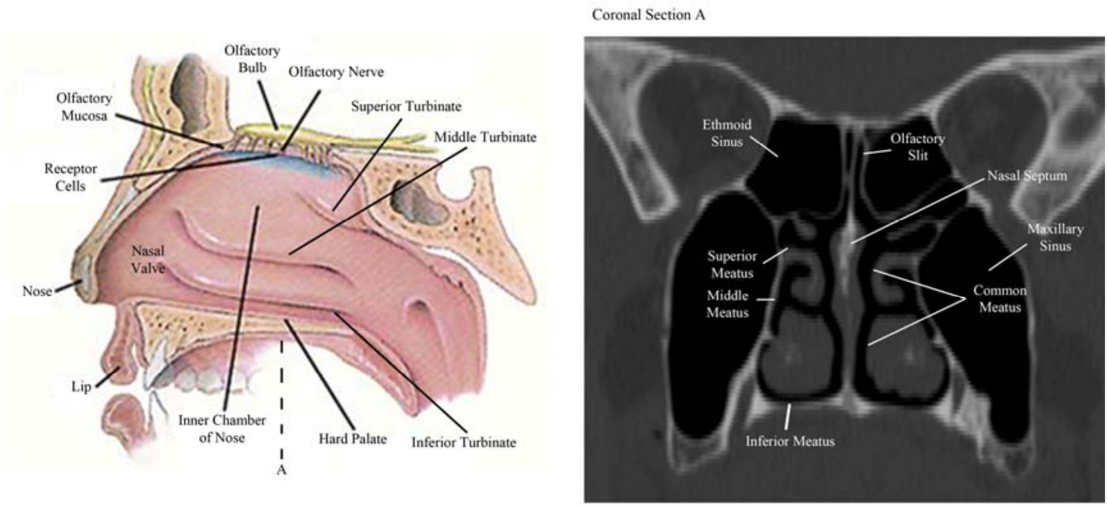

Figure 1.1 Schematic of human nasal cavity.

The pharynx, right after the nasal cavity, consists of three airways: the nasopharynx, the oropharynx and the laryngopharynx (shown in Figure 1.2). The pharynx is surrounded by human tongue, soft palate, pharyngeal wall and other soft tissues which can, to some extent, compromise the airway during respiration mainly due to the pressure of the airflow. Overall, the respiratory airflow experiences two bends in the upper airway to reach the lower airway: one is around the nasal valve, and the other is in the nasopharynx.

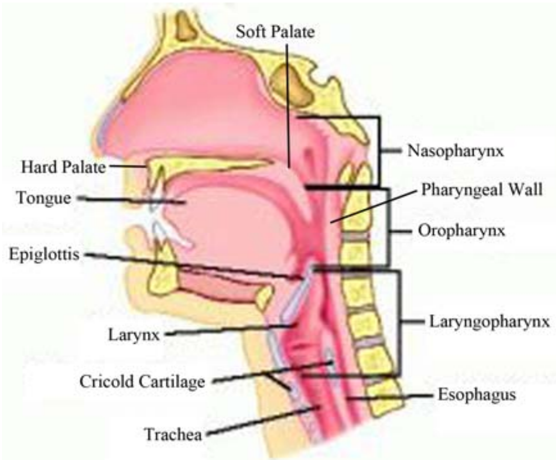

Figure 1.2 Schematic of human pharynx.

1.1.2 Dynamic properties of upper airway morphology

There are several dynamic factors that might influence the airway geometry. One of these factors is the lined mucus at the surface of upper airways. Nasal mucus is produced by the nasal mucosa, and mucal tissues lining the airways are produced by specialized airway epithelial cells and sub-mucosal glands. The mucus continually moves toward the oropharynx preventing foreign objects from entering the lungs during breathing. Since the transportation speed of the mucous layer is rather low compared to respiratory airflow (Kim et al., 1986), usually the mucus could be simplified as a static layer at the surface of the airway. However, as shown in Figure 1.3, the accumulation of the mucus within the upper airway due to low ventilation in maxillary sinus or obstruction of the airway can significantly alter the airway morphology and cause intranasal diseases such as persistent sinusitis (Chung et al., 2002; Kane, 1997; Matthews and Burke, 1997).

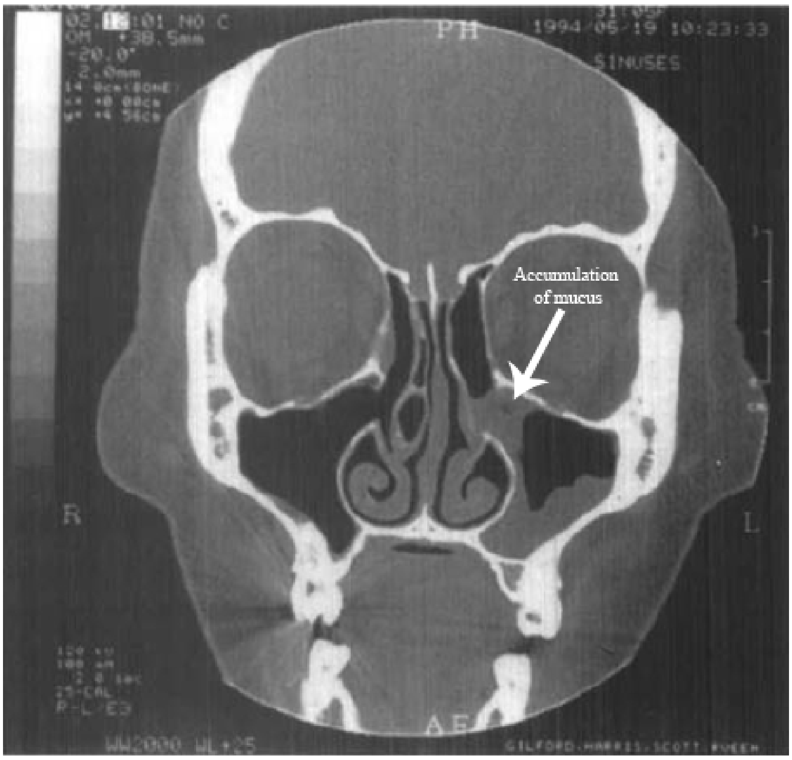

Figure 1.3 CT scan showing continuing infection in left maxillary antrum. Endoscopically the patient had recirculation of mucus between her antrostomy and an accessory ostium (Kane, 1997).

Another dynamic factor of upper airway morphology is the elastic deformation of upper airway structures due to the pressure of the respiratory airflow. Firstly, the sub-atmospheric pressure during inspiration or above atmospheric pressure during expiration tends to contract or dilate the airways (Schwab et al., 1993). Secondly, the human soft palate, lying behind the human tongue, also exhibits dynamic motions during respiration due to the interaction between airflow and soft palate (Lee et al., 2009). These dynamic factors might influence the morphology of human upper airways as well as the upper airflow patterns.

1.2 Literature Review

1.2.1 Airflow in human nasal cavity

1.2.1.1 Breathing patterns

During respiration, human subjects respire cyclically to breathe in oxygen (inspiration) or breathe out carbon dioxide (expiration). The breathing frequency of normal human subjects was reported to be between 6 and 31 breaths per minute, and the duration of inspiration was usually smaller than expiration (Benchetrit, 2000). The average minute ventilation rate (total volume of gas entering the lungs per minute) is approximately 7.5 L during sleep, 9.0 L at sitting position, 25 L at light exercise and 50 L at heavy exercise (Roy et al., 1994). Although the peak nasal inspirational flow (PNIF) rate could be as high as 143 L/min among male subjects and 122 L/min among female subjects (Ottaviano et al., 2006), naturally a healthy subject would switch from nasal to oronasal breathing around ventilation rate of 35 L/min before the PNIF rate is reached (Niinimaa et al., 1980). Since any oral or oronasal respiration is not considered in the scope of this dissertation, the minute ventilation rate is restricted to be below 35 L through all the studies to maintain the fidelity of the simulations that have been carried out.

As shown in Figure 1.4, the breathing process, certainly, is a transient phenomenon with the flow rate varying between inspiration and expiration and from breath to breath (Tobin et al., 1983). Due to the low Strouhal number (< 0.25) and low Womersley number (< 3) of the nasal airflow for quiet breathing at a frequency of 15 breaths per minute, the quasi-steady approximation is considered to be suitable for analysis of airflow properties in human upper airway, if other properties are not involved such as particle deposition on nasal wall, transfer of odorant molecules and heat transfer (Doorly et al., 2008a).The quasi-steady assumption has been utilized in many computational fluid dynamics (CFD) simulation studies on human nasal airflow (Höschler et al., 2003; Subramaniam et al., 1998; Wen et al., 2008). However, by comparing flow patterns of unsteady flow with steady flow at the same rate using CFD, Horschler et al. (2010) reported that at transition from inspiration to expiration the unsteady results, to some extent, differed from the steady state solutions; while at high flow rates the results between steady and unsteady conditions were closer. Lee et al. (2010) suggested that the inertial effect associated with unsteady flow is more important during expiration period than inspiration period.

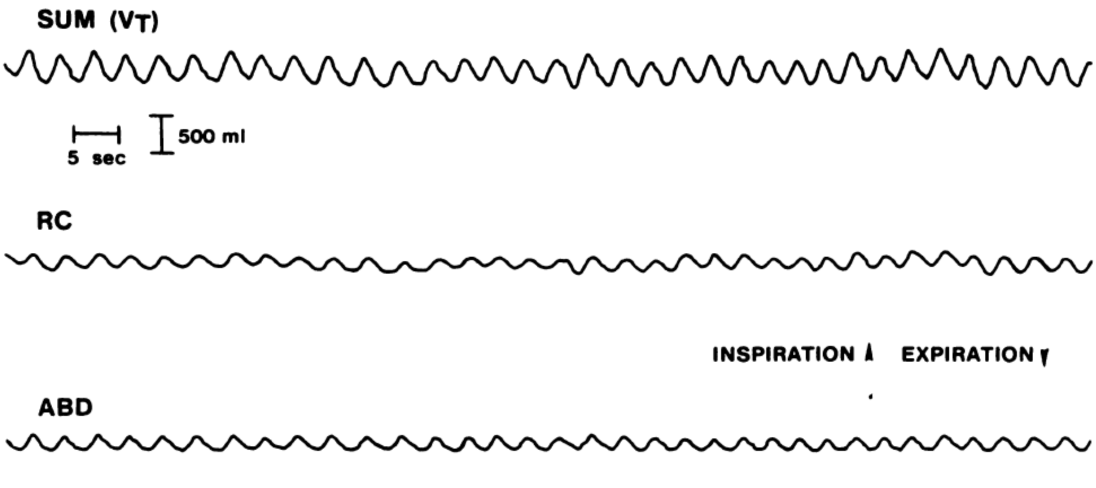

Figure 1.4 Representative breathing pattern in a young normal adult. SUM(V_T) designates the sum of the rib cage (RC) and abdominal (ABD) excursion (Tobin et al., 1983).

1.2.1.2 Flow regime

The fluid flow is laminar at low flow rate, while transitions to turbulent flow when the Reynolds number of the flow exceeds a particular value. As a transient process, the respiratory airflow rate in human upper airway accelerates first and then decelerates until the end of the inspiration and expiration. The acceleration and deceleration could have changed the flow regime of the airflow since turbulence might be involved. Hahn et al. (1993), by measuring velocity magnitude in a large scale anatomically correct cast model of a human adult right nasal cavity, proved that for normal breathing laminar flow may be present in much of the nasal cavity. With the same model and by CFD simulation, Keyhani et al. (1995) further testified that the flow was laminar during quiet breathing with half-nasal flow rate below 200 ml/s (12 L/min); With higher flow rate the transition from laminar flow to turbulent flow would begin. In addition, with a large scale model of human nasal cavity, Schreck et al. (1993) claimed that the onset of turbulence was around 200 ml/s (12 L/min) per nasal airway; and the fully developed turbulence was not reached until 500 ml/s (30 L/min). Therefore, a breath usually involves three flow regimes: the laminar flow at lower flow rate (< 12 L/min), the transition between laminar flow and turbulent flow at medium flow rate (12-30 L/min) and the full turbulent flow at high flow rate (> 30 L/min). In addition, the respiratory air is usually considered incompressible Newtonian due to the low Mach number (< 0.3) (Bailie et al., 2006).

1.2.1.3 Flow patterns in nasal cavity

The detailed distribution of airflow through the nasal cavity during respiration is quite important since it is related to all the nasal functions of olfaction, particle deposition, temperature regulation and humidification. By measuring velocity magnitude along a cast model of nasal airway, it has been found that 50% of inspired air flows through the combined middle and inferior airways and 14% through the olfactory region (Hahn et al., 1993). With a cadaver head model, Simmen et al. (1999) agreed that the main flow passed over the head of the inferior turbinate through the middle meatus. The olfactory region was found to be aerated only toward the end of inspiration and during the entire expiration phase. Through both flow visualization and particle image velocimetry measurement in a cast model of human nasal cavity, Doorly et al. (2008b) reported that the airflow accelerated in the nasal vestibule, entering the main cavity through the internal nasal valve as a high-velocity jet where it impacted on the middle turbinate (Figure 1.5). Low flow was observed in the olfactory region as well as the lower meatus.

Figure 1.5 A cast of nasal cavity fabricated by Doorly et al. (2008b).

Besides in vivo measurement in human subjects or ex vivo measurement in human nasal models of cadaver or plastic cast, another convenient method to investigate human upper airway airflow patterns is CFD simulation based on computerized tomography (CT) or magnetic resonance imaging (MRI) scans. Figure 1.6 shows a typical 3D model of human nasal cavity and surrounded tissues extracted from CT scans. The 3D models would firstly be discretized with elements, and then used for numerical simulations and result analysis. The validation of CFD simulation of human nasal airflow has been testified by comparing airflow properties generated from simulation with in vitro experiments (Croce et al., 2006; Segal et al., 2008; Weinhold and Mlynski, 2004). By reconstructing nasal models of normal subjects, most of the airflow was found to pass through the common and middle meatuses (Wen et al., 2008; Xiong et al., 2008) with less than 14% airflow reached the olfactory region (Zhao et al., 2004). The flow velocity was found to be maximal in the common meatus, followed by the middle, inferior and superior meatus during both inspiration and expiration (Xiong et al., 2008).

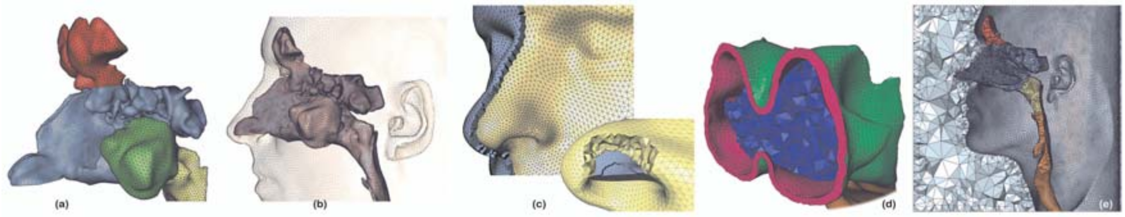

Figure 1.6 Geometric model of the nasal airflow domain: Remeshed non-manifold tissue boundaries (a, b), unstructured, hybrid (mixed-element grid) (c, d), complete volumetric grid with anterior inflow region (e) (Zachow et al., 2009).

Vortexes could usually be found along the nasal cavity. Keyhani et al. (1997), by modifying the anterior nasal roof with an abrupt change in a half nasal model, observed a separated recirculating zone around the anterior nasal roof region; while no vortex was found in the original nasal model. Indeed, this kind of vortex can be found in the anterior nasal roof of a normal nasal cavity (Schreck et al., 1993). The existence of vortex around human nasal roof might bring the airflow up to the olfactory region to promote the function of olfaction. Besides, as demonstrated in Figure 1.7, vortexes can also appear around the nostrils, along the nasal bottom and in the pharynx due to the curvature of the nasal geometry (Wen et al., 2008).

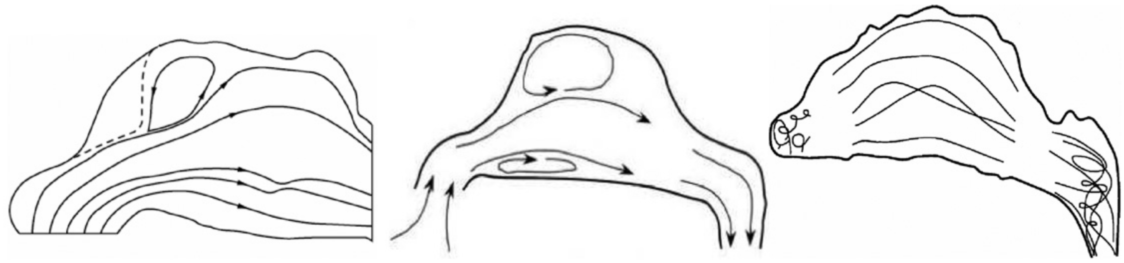

(a) (b) (c)

Figure 1.7 Representation of flow streamlines in nasal cavities: (a) Keyhani et al. (1997), (b) Schreck et al. (1993) and (c) Subramaniam et al. (1998).

The flow resistance of the airway, defined as

$$R = \frac{\Delta p}{V} \tag{1.1}$$

where R is the flow resistance, Δp is the pressure drop along the airway and V is the volume flow rate through the airway, is a parameter to measure how much efforts from the subjects are needed to make during respiration. Flow resistance is related with a number of factors such as geometry of the airway, nasal congestion and deformation of the nasal cavity. High flow resistance could induce nasal obstruction where more efforts are needed to breathe in the same amount of air. Temperature and humidification have influences on nasal resistance as well (Fontanari et al., 1996). It was reported that the first 2-cm segment from the nostril accounted for above 50% of the nasal resistance (Hirschberg et al., 1995). Wen et al. (2008) confirmed that the majority of the nasal resistance to airflow was produced in the frontal region. This could be because the narrowest region with minimum cross sectional area (MCA) along the nasal airway appears in this region (Roithmann et al., 1995).

1.2.1.4 Nasal airflow and nasal morphology

Despite the factors of surrounding environment such as temperature, humidification and wind speed which can affect nasal airflow patterns from time to time, the shape of the nasal cavity is a fixed determination of the nasal airflow. For example, ethnic group (groups of subjects of different ancestral origins) is a factor to cause variation of nasal morphologies among individuals. The evolutionary adaptation of the nose to climate and natural selection for a suitable nose to facilitate airflow are hypothesized to have made the shape and dimensions of the nasal cavities of ethnic groups different due to different living environments. One of the prominent differences of nasal geometry among ethnic groups is the nasal index. Defined by the ratio between nasal breadth and nasal height multiplied by 100, the nasal indices were reported to be significantly different among ethnic groups (Davies, 1932; Leong and Eccles, 2009). However, Leong and Eccles (2009) also claimed that instead of ethnic group as a non-scientific terminology, the nasal index is a more reliable discriminator to differentiate human nasal cavities. In addition, the shapes of nostrils also vary among ethnic groups. As shown in Figure 1.8, with a larger nasal index, the shape of nose of Negroid is more transverse; while with a smaller nasal index, the shape of nose of Caucasian is more longitudinal. With an intermediate nasal index, a roundish shape of nose appears on Oriental. Nevertheless, using acoustic rhinometry to measure the cross sectional area (CSA) along the nasal cavity, Huang et al. (2001) claimed that there was no significant difference in the internal nasal airway among Chinese, Malays and Indians. Possibly due to the differences of nasal morphology, the nasal cavities of different ethnic groups also exhibit different nasal functions. For example, Bennett and Zeman (2005) reported that African Americans had a reduced nasal efficiency for uptake of fine particles compared to Caucasians. Besides, other factors, such as body mass index and gender, are also associated with nasal morphology and nasal airflow patterns (Crouse and Laine-Alava, 1999; Segal et al., 2008). However, there have not been many studies on the effects of these factors on nasal airflow patterns.

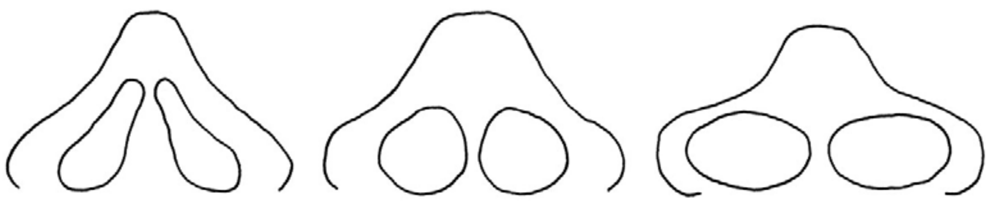

Figure 1.8 Shapes of noses of Caucasian (left), Oriental (middle) and Negroid (bottom) modified from Leong and Eccles (2009).

In addition to variations of nasal cavities among ethnic groups, genders, living habits and body mass index, there are other factors which can deform the nasal morphology and damage nasal airflow patterns and functions. For example, the nasal morphology can be easily distorted due to the compromise of surrounding structures or nasal pathological reasons such as aesthetic rhinoplasty, septal deviation, nasal trauma and facial bone fracture (Haarmann et al., 2009; Higuera et al., 2007; Kocer, 2001). Acoustic rhinometry has been used to evaluate the effectiveness of facial bone fracture reduction by measuring the MCA of the nose at the nasal valve, where the MCA in deformed nasal cavity was reported to be significantly smaller than normal subjects (Chun et al., 2009; Gosepath et al., 2000). Haarmann et al. (2009) studied the changes of nasal airway morphology and flow resistance resulted from Le Fort I osteotomy and functional rhinosurgery using acoustic rhinometry and rhinomanometry. After the operation, the cross sectional areas

(CSAs) and the nasal volume were largely increased, accompanied by a significant decrease of flow resistance. However, the effects of nasal bone fracture and surgical operation on nasal airflow patterns have not yet been thoroughly investigated with CFD.

Moreover, the distortion of anterior nasal airway was found to have much larger impact on nasal airflow patterns than middle and posterior nasal airway (Garcia et al., 2010). Deviated nose, referring to appearance of deviated external nose due to deformity of nasal bones, upper and lower cartilages, nasal septum or a combination of any of these elements, is one cause of anterior airway distortion. As shown in Figure 1.9, the external appearance of deviated nose could be S-shaped, C-shaped and slanted (or I-shaped). The cause of deviated nose may be congenital or acquired secondary to previous trauma or surgery (Rohrich et al., 2002). Either endonasal or external rhinoplasty is required to cosmetically straighten the nose and functionally restore the nasal cavity. However, correction of the deviated nose remains one of the most challenging problems for septorhinoplasty possibly due to the complex nasal structures and surgical techniques involved. A number of correction techniques have been proposed to treat crooked nose resulting from different deformed locations such as upper, middle or inferior third of external nose (Hoffmann, 1999; Okur et al., 2004; Pontius and Leach, 2004; Porter and Toriumi, 2002; Rohrich et al., 2002; Zoumalan et al., 2009). Nevertheless, the current techniques mainly concentrate on straightening and symmetrising the nose, with minimal focus on restoration of nasal airflow patterns. Based upon 260 patients, Foda (2005) reported that breathing was improved in 80% of the patients with both deviated nose and nasal obstruction mainly resulted from straightening of the nasal septum and widening of the nasal valve region. Yet the nasal morphology in the other 20% of the patients did not obtain sufficient correction through surgical intervention to restore a normal breathing. More efforts are therefore needed for restoration of nasal airflow in deviated nose during surgery.

Figure 1.9 Twisted noses. (A) C-shaped deformity with upper and middle thirds markedly displaced to the right and lower third near to the midline. (B) S-shaped deformity with upper third close to midline, middle third to the right, and the tip displaced slightly to the left. (C) Upper third in midline with lower two thirds deflected to the left. These images were modified from Hoffmann (1999).

1.2.2 Airflow in maxillary sinus

The human maxillary sinus, lying beside the nasal airway, is particularly susceptible to infection, since excess fluid cannot be easily drained out of them by gravity (Hood et al., 2009). The maxillary sinus natural ostium (NO), connecting the sinus and the nasal airway, is the only passage for fluid exchange between these two lumens, except when there exists an accessory ostium (AO). Figure 1.10 demonstrates the maxillary sinuses, NO and AO. In Figure 1.10(A), two AOs were found in a cadaver right behind the NO. Figure 1.10(B) and Figure 1.10(C) show the coronal CT image of a subject with two AOs on the left side and one AO on the right side of the airway. The NO connects the maxillary sinus to the superior portion of the middle meatus of the nasal airway, while the location of AO is quite arbitrary along the interior wall of sinus. The prevalence of AO was estimated to be between 4 and 50 percent (Jog and McGarry, 2003). In addition, the existence of AO was found to be associated with mucus circulation between AO and NO (Chung et al., 1999), which was thought to be a major cause of persistent rhinosinusitis and chronic maxillary sinusitis (Kane, 1997; Matthews and Burke, 1997).

Since the NO is often shielded from direct access by the uncinate process, turbinates and ethmoid cells, direct physical measurements of maxillary sinus ventilation are difficult without sinus puncture. In the past, the functional size of the NO has been determined by measuring the pressure rise in the maxillary antrum and comparing it with a nomogram (Aust and Drettner, 1974a). Using an oxygen electrode, ostium patency was reported to be associated with the partial pressure of oxygen inside the maxillary sinus (Aust and Drettner, 1974b). And, since the sinuses are sites for nitric oxide production, nitric oxide concentrations can also be used to assess maxillary ventilation (Granqvist et al., 2006; Weitzberg and Lundberg, 2002). However, there is still very limited information on maxillary sinus ventilation, especially airflow patterns through sinuses with more than one ostium.

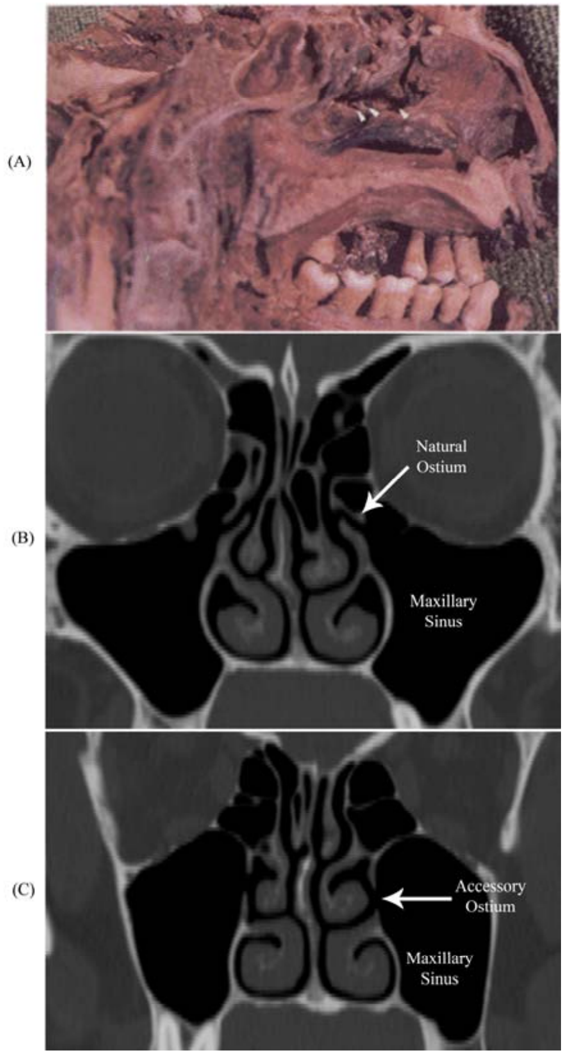

Figure 1.10 Maxillary sinuses and ostia. (A), twin AOs in the cadaver nasal cavity along with a large NO in the anterior (Kumar et al., 2001). (B) CT image of NO. (C) CT image of AO.

Xiong et al. (2008), constructed a 3D model of a healthy nasal cavity and paranasal sinuses, and showed very little air exchange between the paranasal sinuses and nasal cavity during stable airflow. Hood et al. (2009) built simplified 3D models with/without AO by characterizing the sinus as a large truncated cone joining to a rectangular channel which represents the middle meatus of the nasal cavity, to evaluate maxillary sinus gas exchange. They found that the presence of an AO could increase the sinus ventilation rate by several orders of magnitude. Their findings were confirmed with a replica of this simplified model (Rennie et al., 2011). However, any minor change of nasal geometry (Garcia et al., 2010; Zhao et al., 2004) or differences of boundary conditions (Taylor et al., 2010) in these prior studies could significantly influence the output of numerical simulation of nasal airflow which may alter the sinus ventilation. Therefore, a high resolution, life-like 3D nasal cavity and maxillary sinus model, with and without AO, is still preferred to accurately assess the effects of AO on maxillary sinus ventilation.

1.2.3 Airflow in human pharynx with motion of surrounding tissues

Unlike nasal airway, the geometry of human upper airway is subjected to considerably change during respiratory activity due to the compliance of surrounding pharyngeal soft tissues. The compliance of tissues could lead to serious problems such as snoring or obstructive sleep apnea-hypopnea syndrome (OSAHS). These OSAHS patients suffer from recurrent episodes of partial or complete occlusion of the upper airway with symptoms of excessive daytime sleepiness, choking or gasping during sleep, daytime fatigue and impaired concentration (Randerath et al., 2006). The occurrence of OSAHS was reported to be as high as 2% among adult women and 4% among adult men (Young et al., 1993).

The compromise of human pharyngeal airway during cyclic breathing has become a hotspot to researchers driven by the complicated mechanisms of pharyngeal occlusion and the related prevalent diseases such as OSAHS. The occlusion of human upper airway was found to be related to pharyngeal morphology (Schwab et al., 1995), properties of respiratory airflow (Hollandt and Mahlerwein, 2003), properties of surrounded tissues of pharyngeal airway (Cheng et al., 2011) and intensity of muscle activation (Huang et al., 2005a; Sauerland and Harper, 1976). In the past, CT and MRI scans have been used to examine the compromise of the upper airway and the surrounding tissues (Caballero et al., 1998; Koren et al., 2009; Schwab et al., 1993; Schwab et al., 1995; Schwab et al., 1996; Schwab et al., 2006). Using dynamic MRI imaging, Schwab et al. (1993) reported that the upper airway CSA slightly decreased during inspiration while increased during expiration (Figure 1.11). This is reasonable as the inspirational sub-atmospheric pressure of the airflow applies inward forces on the surrounded walls to shrink the lumen, and the expiratory above-atmospheric pressure applies outward forces to dilate the airway. However, recently more and more evidences show that the upper airway patency of OSA patients occluded to a minimum at the end of expiration (Dempsey et al., 2010; Morrell et al., 1998; Verbraecken and De Backer, 2009) which conflicts with Schwab et al. (1993)'s findings. This controversy has not been fully understood yet, which may require more detailed study of occlusive mechanisms of human pharyngeal airway for an explanation.

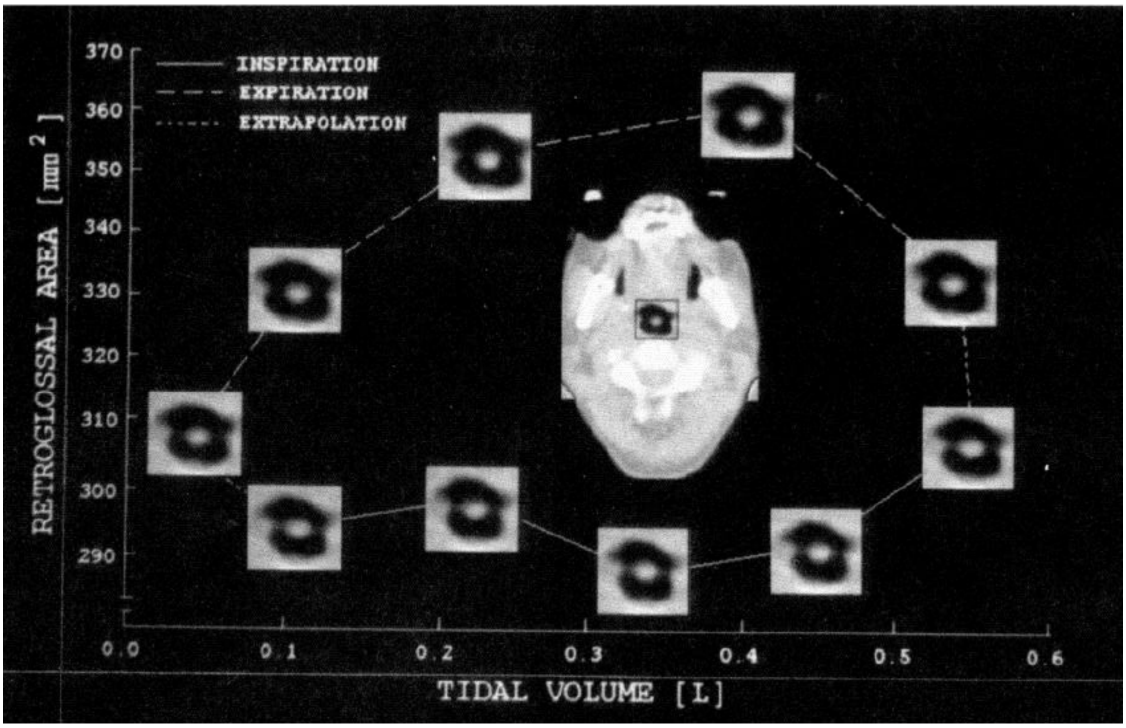

Figure 1.11 Images throughout respiration at retroglossal level demonstrating respiratory variation in upper airway area of a normal subject. Size of airway remains relatively constant during inspiration and expands during expiration (Schwab et al., 1993).

Despite morphology analysis, CFD simulations have also been carried out to investigate the pharyngeal airflow patterns in patients with OSAHS in a number of studies (Jeong et al., 2007; Shome et al., 1998; Sung et al., 2006). Using CFD simulation, Jeong et al. (2007) evaluated the aerodynamic force of the upper airway of patient with OSAHS (Figure 1.12). They concluded that the velopharynx might be the most collapsible area in the pharyngeal airway due to the minimum intraluminal pressure and maximum aerodynamic force. However, since the pharyngeal tissues such as tongue and soft palate could experience substantial displacement to collapse the air space, the interaction between airflow and soft tissues is also crucial to the pharyngeal occlusion mechanisms, which cannot be investigated with sole CFD models. Instead, this interaction has been predicted using fluid/structure interaction (FSI) models (Chouly et al., 2008; Huang et al., 2005a; Huang et al., 2005b; Sun et al., 2007). Huang et al. (2005a), by reconstructing a 2D human upper airway, successfully reproduced the inspirational airway occlusion using FSI simulation (Figure 1.13). Sun et al. (2007) reconstructed a 3D FSI model including all the nasal cavity, pharynx and oral airway to simulate the movement of human soft palate during respiration. Nevertheless, the mesh in this model is rather coarse, and the boundary at side walls of the soft palate was not been properly prescribed. A more comprehensive 3D FSI model of human upper airway is still needed to more precisely predict the dynamic change of upper airway tissues and airway morphology during respiration.

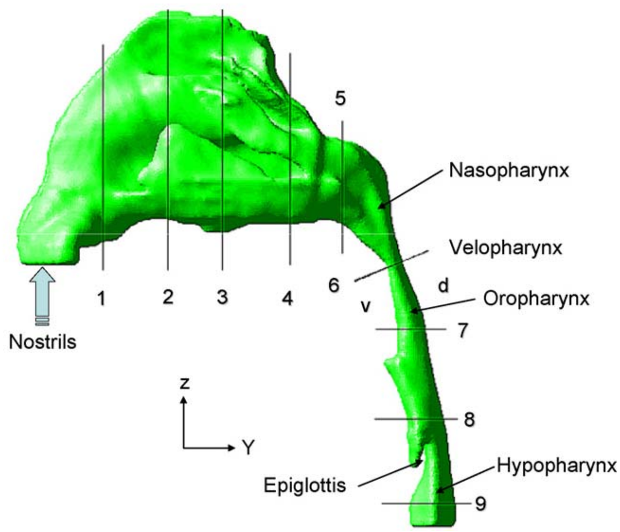

Figure 1.12 3D model of nasal and pharyngeal airway built by Jeong et al. (2007).

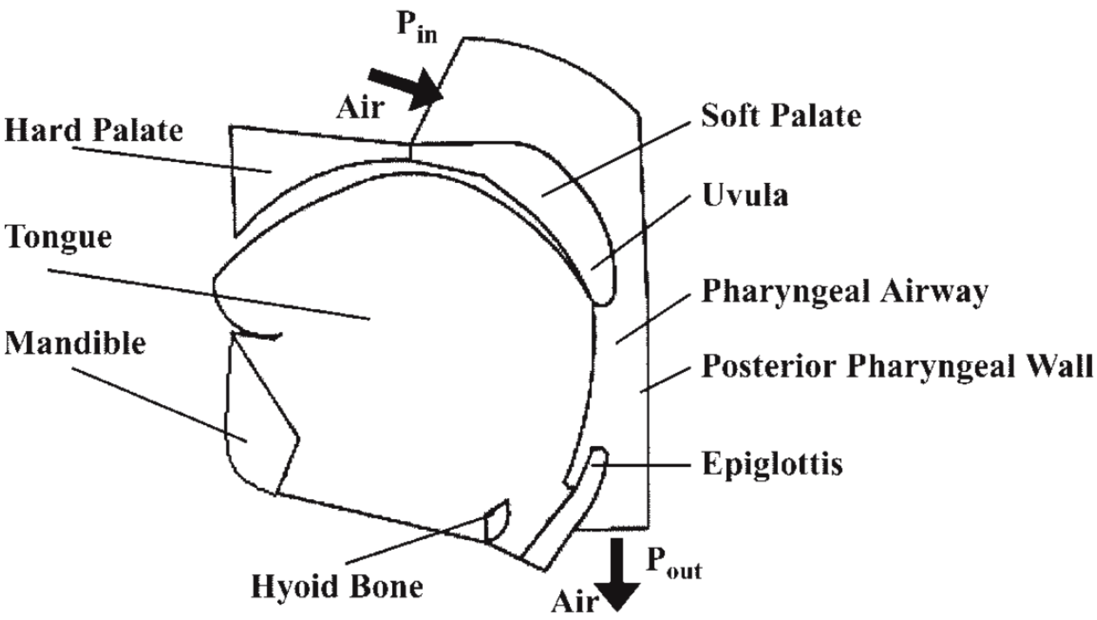

Figure 1.13 2D FSI model of human pharyngeal airway created by Huang et al. (2005a).

1.3 Objectives and scope of the study

1.3.1 Motivations

As mentioned above, the adaptation of nose to various environments induces different efficiencies of nasal functions among ethnic groups. However, since nasal airflow is the major determinant of nasal functions, knowledge on how the nasal morphologies of different ethnic groups interact with nasal airflow patterns is important but is still lacking. The deformation of the nasal airway, such as distortion of nasal cavity caused by nasal bone fracture or deviation of external nose, can produce impairment of daily respiratory activity and nasal functions to certain patients. A comprehensive investigation on how the nasal airflow is influenced by airway distortion and possible suggestions of restoration of the nasal airway and airflow is needed to improve breathing activities of the relative patients. Besides nasal cavity, the air ventilation through maxillary sinuses is crucial since sinus diseases affect around 15% of human beings. Nevertheless, as one of the major causes of sinus diseases, effects of the existence of AO on maxillary sinus ventilation are yet to be examined. In addition, the compromise of human pharyngeal airway to airflow in the pharynx is one of the major causes of certain prevalent diseases such as OSA and snoring. However, the mechanisms of pharyngeal occlusion are quite complex and still not fully understood.

1.3.2 Objectives

The objectives of this thesis are therefore:

- to evaluate the effects of morphological difference of nasal airways among ethnic groups on nasal airflow patterns.
- to evaluate the effects of bone fracture and surgical operation on nasal airflow patterns.
- to evaluate the effects of deviated external noses on nasal airflow patterns
- to evaluate the existence of accessory maxillary ostium on maxillary sinus ventilation.
- and to evaluate the interaction between human soft palate and upper airway flow during calm respiration.

1.3.3 Scope

Within this thesis, the nasal airflow is assumed as incompressible Newtonian. The airflow is assumed to flow through nostrils, with the oral airway closed. Laminar model is used for lower ventilation rate below 20 L/min, and low Reynolds k-ω turbulent model is used for higher flow rate. The nasal wall is considered to be rigid, and the mucus is assumed as a static layer lining on the nasal wall to simplify the mathematical model. The material property of human soft palate is simplified as elastic, isotropic and homogeneous. In addition, only the airflow properties of human upper airway are examined, yet the upper airway functions are not considered.

1.3.4 Organization of the thesis

The remaining part of this thesis is organized as follows. Chapter 2 describes how the simulations are carried out. 3D models of human upper airway are firstly reconstructed. The models would then be discretized into tetrahedron elements coated with prism layers. CFD and FSI are used to simulate the nasal airflow and the movement of human soft palate, respectively.

Chapter 3 evaluates the differences of nasal airflow patterns among nasal cavities of individuals from three ethnic groups using CFD simulation, namely, one Caucasian, one Chinese and one Indian.

Chapter 4 presents two case studies of nasal airflow through deformed nasal cavities using CFD simulation. Firstly, effects of bone fracture and surgical operation on airflow through nasal cavity with orbito-maxillary bone fracture are evaluated. Secondly, three

3D nasal models of subjects with typical crooked noses are simulated, namely, one with S-shaped crooked nose, one with C-shaped crooked nose and one with slanted crooked nose.

Chapter 5 evaluates the airflow ventilation through human maxillary sinuses with/without accessory ostia using CFD simulation. A 3D nasal model is constructed from an adult CT scans with two left maxillary AOs and one right AO, then compared to an identical control model with all AOs sealed.

Chapter 6 assesses the mechanisms of the movement of human soft palate during respiration using FSI simulation. A 3D FSI model of a healthy male subject is reconstructed and simulated. The fluid domain consists of the nasal cavity, nasopharynx and oropharynx. The human soft palate is the only structure which displaces during respiration.

The final chapter summarizes the results of this thesis and proposes possible future works.

Chapter 2 Methodology

Prior to numerical simulations, CT or MRI scans are firstly collected for reconstruction of 3D models of human upper airway. Sections 2.1 and 2.2 introduce the process of reconstruction and discretization of 3D models from CT and MRI scans. In chapters 3, 4 and 5, CFD simulations are carried out to investigate airflow patterns through human nasal cavities and maxillary sinuses. The governing equations for CFD simulation, the numerical methods to discretize and solve these equations, and the validation of the CFD models are presented in section 2.3. In chapter 6, an FSI model is developed to evaluate the interaction between movement of human soft palate and upper airway airflow. The governing equations of FSI simulation, the procedure to solve these equations and the grid independence test are described in section 2.4.

2.1 3D model reconstruction of human upper airway

CT or MRI scans of heads of human subjects are obtained for model reconstruction of human upper airways. The CT images are pixel maps of the linear X-ray attenuation coefficient of tissue. The pixel values are scaled so that the linear X-ray attenuation coefficient of air equals -1024 and that of water equals 0. In this scale, fat is around -110, muscle is around 40, trabecular bone is in the range of 100 to 300 and cortical bone extends above trabecular bone to about 2000. Similarly, MRI scans also exhibit such feature, where the minimum pixel value corresponds to the cavity and the maximum value corresponds to hard bone. Therefore, from both the CT and MRI scans, different components of human body such as soft tissues, bones and cavities can be easily identified from each other. During the imaging process, the subjects are under supine condition and are told to breathe quietly so that the shape of human upper airway is more or less unchanged through the scanning process.

The commercial software MIMICS (Version 12.1.0.12, Materialise Group, Leuven, Belgium. http://biomedical.materialise.com/) is used to build the 3D models. The procedures of reconstructing 3D models from CT or MRI scans using MIMICS are listed as follows:

- CT or MRI images are firstly imported into MIMICS. As shown in Figure 2.1, other than the original images (axial view), images in the other two directions (sagittal and coronal views) would be automatically generated from the original images by interpolating the values of the pixels within the images.

- Function of thresholding in MIMICS is then applied to separate the pixels of targeting region from the rest pixels of the image. For example, by setting the span of thresholding to be between -1024 and -250, pixels of the airway would be selected and isolated from the rest of the image.

- The selected pixels in the previous step (defined as "mask" in MIMICS) are then modified to refine the shape of the targeting region, since it is nearly impossible to use one thresholding span to perfectly segment the entire targeting region. For example, Figure 2.2(A) shows the coronal view of the mask. The airway (green color) has been separated from the rest pixels by thresholding. However, there are some regions, which initially are separated from each other (depicted by white arrow in Figure 2.2(C)), merging together (depicted by white arrow in Figure 2.2(B)) in the created mask by the automatic thresholding process. Further modifications are therefore required to make the morphology of the mask to be more representative for the targeting component.

- Thereafter, the Region Growing function of MIMICS is applied to the mask. This function is implemented to make sure that all the chosen pixels are connected to each other thus form one enclosed volume. The pixels that are not connected with the selected pixel will be abandoned.

- 3D model will then be built from the modified mask as shown in Figure 2.3

- After that, the surface of the 3D model is discretized with triangular elements. These triangular elements are finally optimized and exported as Nastran files for further manipulation. During the optimization process, the maximum length of triangular element edge is set to be 1.5 mm to ensure that the geometrical characteristics of the targeting component are well captured by the elements.

Note: The accuracy of the segmented 3D models relies on the resolution of the CT images. The resolution of the original CT or MRI images (the distance between two adjacent pixels) in this thesis is less than 0.39 mm. This is fine enough since the dimension of the upper airway is usually several millimeters. Besides, the resolution in the other two interpolated views relies on the number of CT images. The distance between two consecutive CT images is 0.6 mm for all the reconstructed models in this work, which is fine enough to allow MIMICS to smoothly capture the characteristics of the airway morphology during the interpolating process.

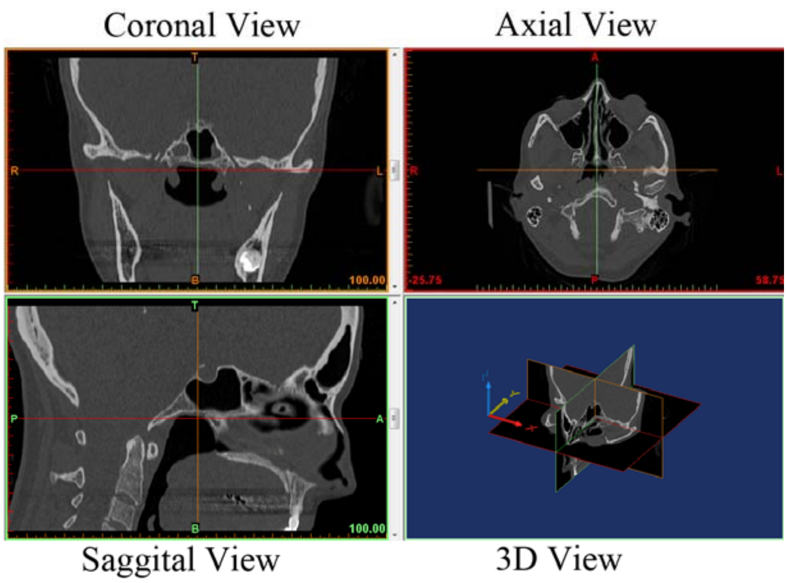

Figure 2.1 Coronal, axial, sagittal and 3D views of imported CT images shown in MIMICS. The letters L, R, A, P, T and B stand for left, right, anterior, posterior, top and bottom, respectively.

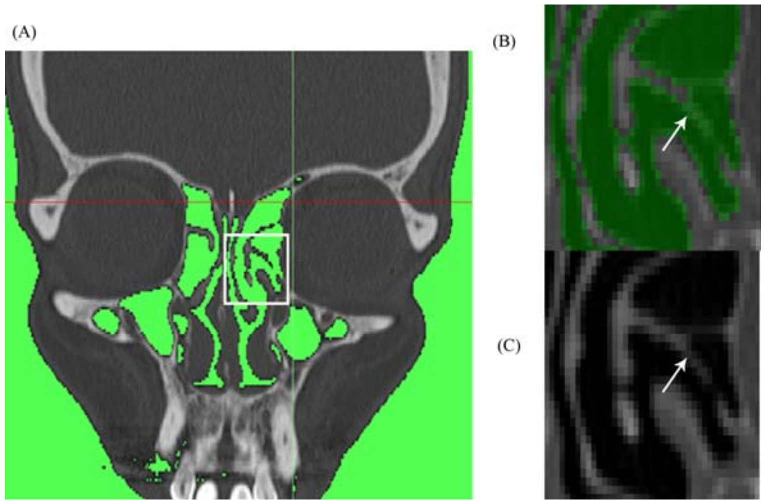

Figure 2.2 Thresholding in MIMICS. (A), mask created by thresholding. (B) enlarged view of the rectangular. (C) the original CT image within the rectangular.

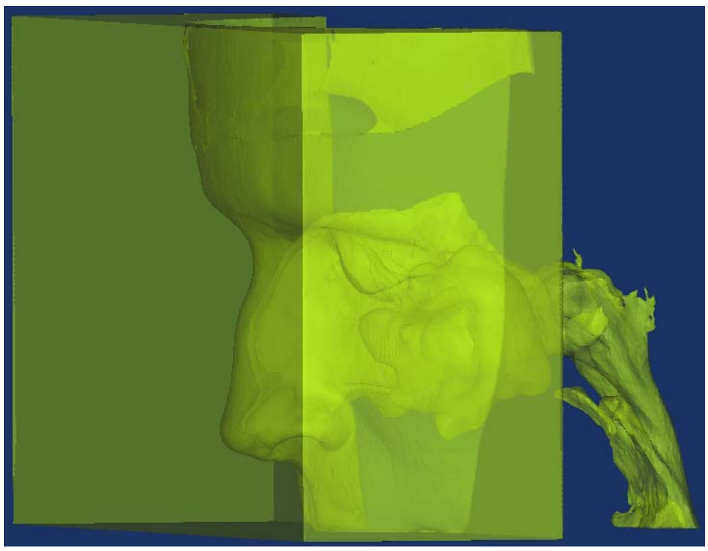

Figure 2.3 3D model of human upper airway built in MIMICS.

2.2 Mesh generation

HYPERMESH (Version 10.1, Altair Engineering Inc., MI, USA. http://www.altairhyperworks.com) is used to generate 3D meshes for the models from the above two-Dimensional triangular elements. The nastran file created from MIMICS is firstly imported into HYPERMESH. As shown in Figure 2.4, the upper airway is extended in HYPERMESH by a 40 mm-radius semi sphere which is assembled around the human face to totally enclose the nostril entrance. The center of the hemi sphere is selected to locate on the human face right below the nostrils. The edge of the hemi sphere is on the intersection between the sphere and the human face. This semi sphere is used to represent natural static air around the human face during simulation, which would ensure a realistic inflow boundary condition. The element size around the human face and the hemi sphere is retained to be 1.5 mm since the morphology in these areas is relatively smooth and far from the domain of interest, while the element size on the wall of the internal nasal airway is refined to 0.6 mm. Due to the complexity of nasal morphology and the narrowness of the nasal airways, some of the elements could be highly distorted, collapsed or connected in the wrong form, such as silver elements (elements that are very close to each other), T-connection elements (elements that belong to two isolated volumes sharing one edge) and elements with tiny holes (Figure 2.5). These elements need to be repaired to avoid possible mathematical singularity during the simulations. The quality of the 2D triangular elements are then optimized according to the aspect ratio of the elements, the minimal length of the elements, the minimal angle of the elements, the maximal angle of the elements and the skewness of the elements. Finally, 3D tetrahedron elements are created based on the triangular elements. As shown in Figure 2.6, five boundary layers with width of each layer to be 0.05 mm are created around the tetrahedron elements. These boundary layers can more precisely predict the near-wall laminar viscosity effect of the airflow during the simulations. The 3D elements are exported as *.cas file for CFD simulation in ANSYS FLUENT (Version 12.1, ANSYS Fluent Inc., PA, USA. http://www.ansys.com), or nastran file for FSI simulation in ADINA (Version 8.6.5, ADINA R & D, Inc., MA, USA. http://www.adina.com).

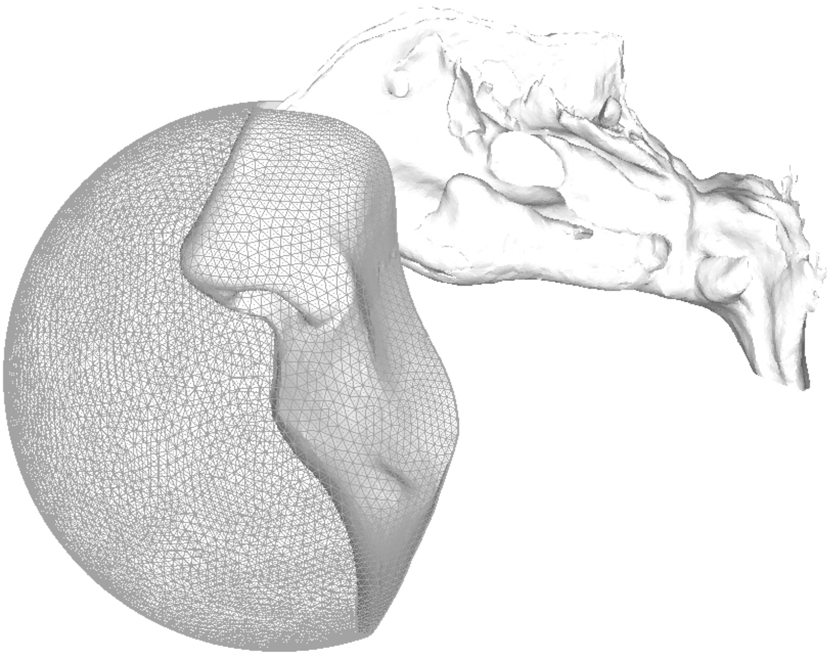

Figure 2.4 3D model of human nasal cavity. A hemi sphere is assembled around the human face for zero ambient gauge pressure prescription.

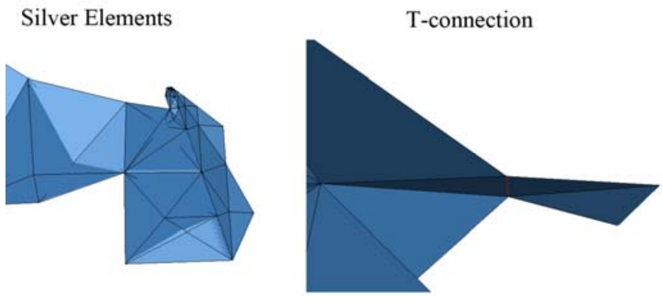

Figure 2.5 Impaired triangular elements.

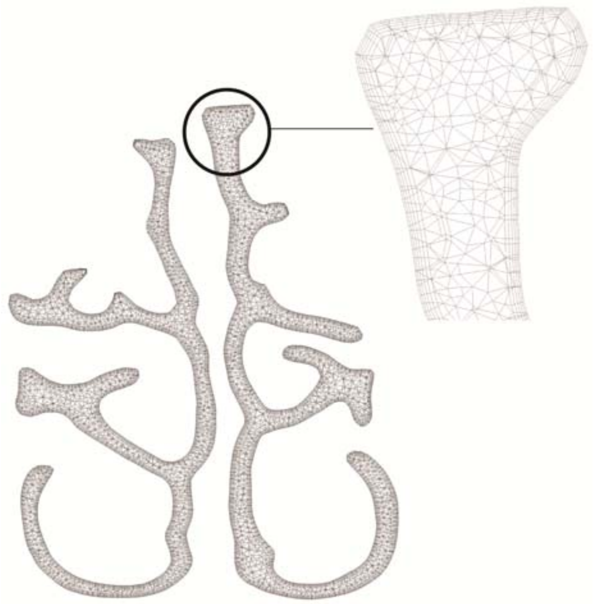

Figure 2.6 Coronal view of the elements.

2.3 CFD simulation

2.3.1 Governing equations for CFD

The nasal airflow is considered as incompressible due to low Mach number (Doorly et al., 2008a). As mentioned in Chapter 1, the nasal airflow is laminar below half-nasal flow rate of 12 L/min (Keyhani et al., 1995), and the full turbulence is not reached until half-nasal flow rate of 30 L/min (Schreck et al., 1993). Therefore, for global ventilation rate less than 24 L/min the airflow is assumed as laminar, and laminar model is used for the CFD simulations. The continuity and Navier-Stokes equations for transient incompressible laminar case are given by:

$$\nabla \bullet \vec{u} = 0 \tag{2.1}$$

$$\rho \frac{\partial \vec{u}}{\partial t} + \rho \vec{u} \bullet \nabla \vec{u} - \nabla \vec{\tau} = 0 \tag{2.2}$$

where $\vec{u}$ is the velocity vector, ρ is the density of ambient air, p is the pressure of airflow, μ is the dynamic viscosity of air and τ is the stress tensor equals to

$$\tau = \text{-}p\vec{I} + 2\mu\vec{e} \tag{2.3}$$

here $\vec{I}$ is the second order unit tensor, and $\vec{e}$ is the velocity strain tensor in the form of

$$\vec{e} = \frac{1}{2}(\nabla \vec{u} + \nabla \vec{u}^{T}) \tag{2.4}$$

For quasi steady-state condition, the Navier-Stokes equations (equation 2.2) reduce to

$$\rho \vec{u} \bullet \nabla \vec{u} - \nabla \vec{\tau} = 0 \tag{2.5}$$

In this thesis, ρ and μ are constants with values of 1.225 kg/m^3 and 1.7894×10^{-5} kg/(m·s), respectively (corresponding to air properties at 15 degree centigrade).

While for ventilation rate above 24 L/min, the transition from laminar flow to turbulent flow begins. A proper turbulent model is needed to simulate nasal airflow regarding both the transition between laminar and turbulent flows and the full turbulent flow. Among the most commonly used approaches, Reynolds averaged Navier-Stokes (RANS) equations along with the k-ε, k-ω or shear stress transport (SST) turbulent model were used to calculate single-phase turbulent flow (Liu et al., 2007). Direct numerical simulation (DNS) and large eddy simulation (LES) have also been used to a lesser degree. However, DNS is normally impractical for complex geometries, while both DNS and LES are computationally much more expensive than the RANS approach. Considering the complexity of the nasal geometry and the large scale of the computational domain, RANS approach is chosen for turbulent modeling. Particularly, low Reynolds number (LRN) k-ω model of Wilcox (1998) is used to simulate turbulence in this thesis. This model was reported to be suitable for simulating both laminar-transitional-turbulent and turbulent flows in constricted tubes such as nasal cavity (Xi and Longest, 2008; Zhang and Clement, 2003). The model has also been applied to simulate particle deposition in human tracheobronchial airways, and the results agreed well with reported experimental data (Li et al., 2007). Besides conservation of mass and momentum, the LRN k-ω model solves two additional equations below for the turbulent kinetic energy and specific dissipation rate:

$$\rho\frac{\partial k}{\partial t}+\rho\frac{\partial(ku_i)}{\partial x_i}=\frac{\partial}{\partial x_j}[(\mu+\frac{\mu_t}{\sigma_k})\frac{\partial k}{\partial x_j}]+\mu_t S^2-\rho\beta^* f_{\beta^*}k\omega \tag{2.6}$$

$$\rho\frac{\partial \omega}{\partial t}+\rho\frac{\partial(\omega u_i)}{\partial x_i}=\frac{\partial}{\partial x_j}[(\mu+\frac{\mu_t}{\sigma_\omega})\frac{\partial \omega}{\partial x_j}]+\alpha\frac{\omega}{k}\mu_t S^2-\rho f_\beta \omega^2 \tag{2.7}$$

here k is the turbulence kinetic energy, ω is the specific dissipation rate, μ_t is the turbulent viscosity defined as

$$\mu_t = \alpha^* \frac{\rho k}{\omega} \tag{2.8}$$

where

$$\alpha^* = \frac{0.024 + Re_t / 6}{1 + Re_t / 6} \tag{2.9}$$

$$Re_t = \frac{\rho k}{\mu \omega} \tag{2.10}$$

S is the modulus of the mean rate-of-strain tensor defined as

$$S \equiv \sqrt{2 S_{ij} S_{ij}} \tag{2.11}$$

where

$$S_{ij} = \frac{1}{2}\left(\frac{\partial u_j}{\partial x_i} + \frac{\partial u_i}{x_j}\right) \tag{2.12}$$

and

$$f_{\beta^*} = \begin{cases} 1 & \chi_k \leq 0 \\ \frac{1+680\chi_k^2}{1+400\chi_k^2} & \chi_k > 0 \end{cases} \tag{2.13}$$

where

$$\chi_k \equiv \frac{1}{\omega^3}\frac{\partial k}{\partial x_j}\frac{\partial \omega}{\partial x_j} \tag{2.14}$$

and

$$\beta^* = 0.09 \times \frac{\frac{4}{15} + (Re_t/8)^4}{1 + (Re_t/8)^4} \tag{2.15}$$

The coefficient f_β is defined as

$$f_\beta = 0.072 \times \frac{1 + 70\chi_\omega}{1 + 80\chi_\omega} \tag{2.16}$$

where

$$\chi_\omega = \left| \frac{\Omega_{ij}\Omega_{jk}S_{ki}}{(\beta^*_\infty \omega)^3} \right| \tag{2.17}$$

$$\Omega_{ij} = \frac{1}{2}\left(\frac{\partial u_i}{\partial x_j} - \frac{\partial u_j}{\partial x_i}\right) \tag{2.18}$$

The coefficient α is given by

$$\alpha = \frac{1}{\alpha^*}\frac{1/9 + Re_t/R_\omega}{1 + Re_t/R_\omega} \tag{2.19}$$

the other coefficients are constants such as σ_k=σ_ω=2, β^*_∞=0.09 and R_ω=2.95.

The continuity and momentum equations for LRN k-ω turbulent model would become:

$$\frac{\partial u_i}{\partial x_i} = 0 \tag{2.20}$$

$$\rho\frac{\partial u_i}{\partial t} + \rho u_j\frac{\partial u_i}{x_j} = -\frac{\partial p}{\partial x_i} + \frac{\partial}{\partial x_j}[(\mu + \mu_t)(\frac{\partial u_i}{\partial x_j} + \frac{\partial u_j}{\partial x_i})] \tag{2.21}$$

For quasi steady-state condition, equations 2.6, 2.7 and 2.21 reduce to

$$\rho\frac{\partial(ku_i)}{\partial x_i} = \frac{\partial}{\partial x_j}[(\mu + \frac{\mu_t}{\sigma_k})\frac{\partial k}{\partial x_j}] + \mu_t S^2 - \rho\beta^* f_{\beta^*} k\omega \tag{2.22}$$

$$\rho\frac{\partial(\omega u_i)}{\partial x_i} = \frac{\partial}{\partial x_j}[(\mu + \frac{\mu_t}{\sigma_\omega})\frac{\partial \omega}{\partial x_j}] + \alpha\frac{\omega}{k}\mu_t S^2 - \rho f_\beta \omega^2 \tag{2.23}$$

$$\rho u_j\frac{\partial u_i}{x_j} = -\frac{\partial p}{\partial x_i} + \frac{\partial}{\partial x_j}[(\mu + \mu_t)(\frac{\partial u_i}{\partial x_j} + \frac{\partial u_j}{\partial x_i})] \tag{2.24}$$

2.3.2 Numerical methods

As a popular commercial CFD package, ANSYS FLUENT is utilized to solve the above equations using finite volume method (FVM). This technique consists of:

- Integration of the governing equations on the individual control volumes (elements) to construct algebraic equations for the discrete dependent variables ("unknowns") such as velocities, pressure and conserved scalars.
- Linearization of the discretized equations and solution of the resultant linear equation system to yield updated values of the dependent variables.

The second-order upwind scheme is used where quantities at cell faces are computed using a multidimensional linear reconstruction approach. The pressure-based segregated algorithm is chosen where the governing equations are solved sequentially. The SIMPLEC algorithm is chosen for pressure-velocity coupling. The following convergence criterion is used for all the solved variables to decide when to stop the iteration process:

$$R^{\Phi} < 10^{-5} \tag{2.25}$$

where R^{Φ} is the scaled residual for variable Φ. More details could be found in ANSYS FLUENT's manual (ANSYS, 2009).

2.3.3 Grid independence test and validation of reconstructed model

Grid independence test is carried out by refining the surface elements of the nasal wall and the outlet using element sizes of 0.8 mm, 0.7 mm, 0.6 mm and 0.55 mm in a nasal model of a healthy male subject. The element size of hemispherical inlet and the human face is retained 1.5 mm. The total numbers of 3D tetrahedron elements generated according to the original mesh and these refined element sizes are 410,418, 1,345,404, 1,750,428, 2,660,094 and 3,148,381, respectively. As shown in Figure 2.7, the mean pressure of the outlet and the mean wall shear stress of the whole nasal wall converge as the surface element size approaches 0.6 mm.

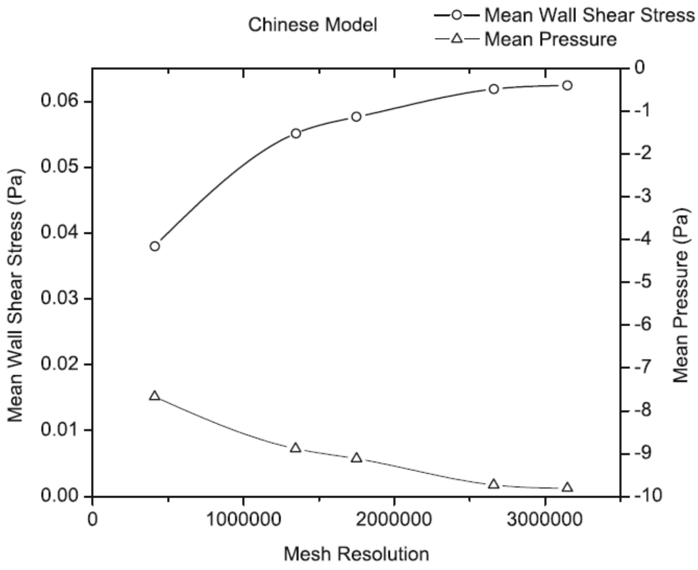

Figure 2.7 Mean wall shear stress of the whole nasal wall and mean pressure at the nasopharynx according to different mesh resolutions.

Subsequently, the whole surface of this model is meshed with element size of 0.6 mm, where 3,975,102 tetrahedron elements are generated. Compared to results from model refined with 0.6 mm element size at nasal wall and outlet only, the discrepancies of the mean outlet pressure and the mean wall shear stress in this model are found to be smaller than 0.4%. Therefore, while the coarse element size on the hemisphere and the human face could reduce the computational cost, the accuracy of the simulation would also be retained. To make a compromise between the computational cost and the accuracy of the simulations, surface element size of 0.6 mm is used to discretize nasal wall and nasopharyngeal outlet with the element size on the hemispherical inlet and the human face retained 1.5 mm.

The validation of the CFD methodology is evaluated by comparing the pressure drops at flow rates up to 667 ml/s in a healthy nasal model with experimental data reported by Weinhold and Mlynski (2004). As shown in Figure 2.8, the patterns of pressure drop with increasing flow rate at nasopharynx from simulation agree well with data collected by the experiments.

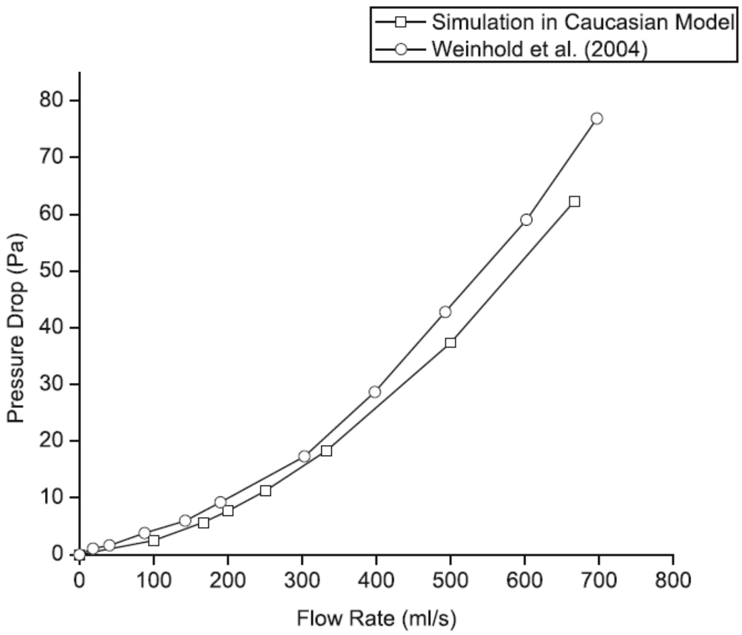

Figure 2.8 Comparison of pressure drop at nasopharynx as a function of flow rates between simulation and reported experimental data.

A nasal model with 80 mm radius hemi sphere was built to investigate whether the 40 mm radius hemi sphere is large enough or not to allow the nasal airflow naturally developing into the nostrils. As shown in Figure 2.9, the velocity contours in both models with 80 mm radius hemi sphere and 40 mm hemi sphere are comparable. In addition, the difference of maximum velocity magnitude between the two models is around 0.34%. Therefore the 40 mm radius hemi sphere is accurate enough for the simulations.

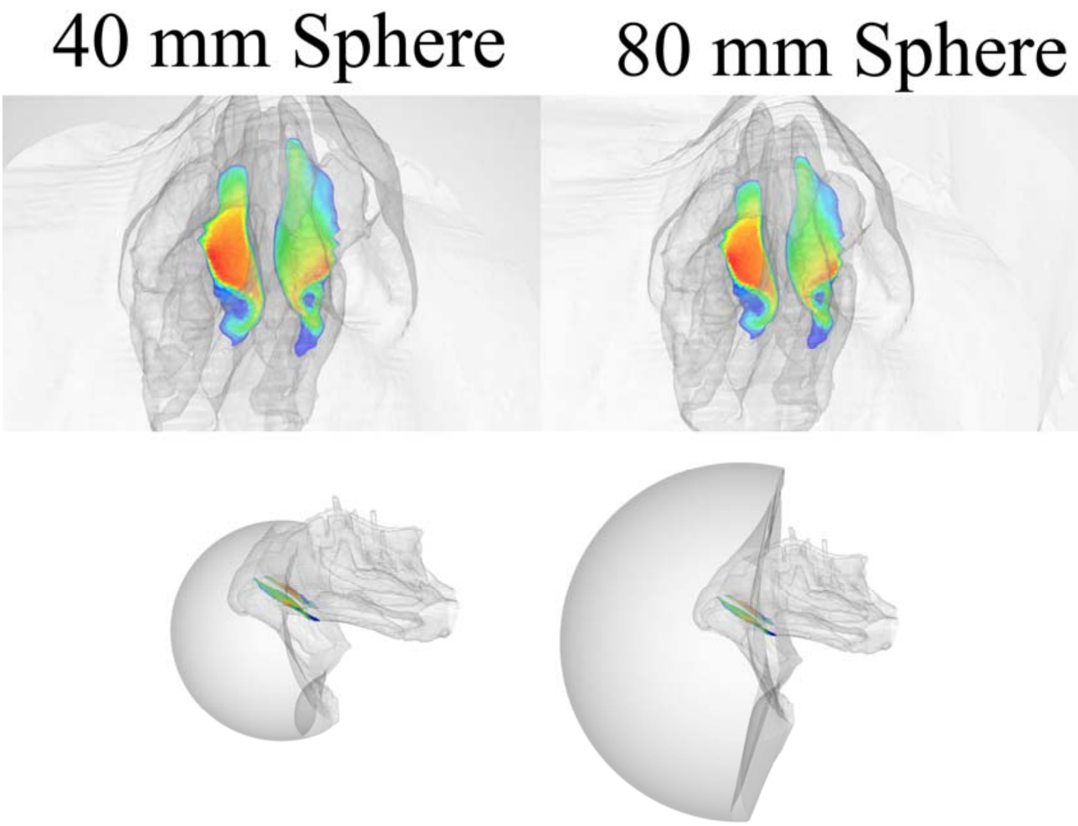

Figure 2.9 Velocity contours around nasal valve in models with different sizes of hemi sphere.

2.4 FSI simulation

2.4.1 Governing equations for FSI

In Chapter 6, FSI simulations are carried out to evaluate the interaction between upper airway airflow and movement of human soft palate. The airflow is considered as incompressible and laminar. The human soft palate is simplified as linear elastic, isotropic and homogeneous. The following governing equations for linear elastic materials are solved during the simulation:

$$\sigma_{ji,j} = \rho' \frac{\partial^2 v_i}{\partial t^2} \tag{2.26}$$

$$\varepsilon_{ij} = \frac{1}{2}\left(\frac{\partial v_i}{\partial x_j} + \frac{\partial v_j}{\partial x_i}\right) \tag{2.27}$$

$$\sigma_{ij} = \frac{E\nu}{(1-2\nu)(1+\nu)}\varepsilon_{kk}\delta_{ij} + \frac{E}{1+\nu}\varepsilon_{ij} \tag{2.28}$$

where σ is the Cauchy stress tensor, ρ' is the density of the structure, v is the displacement of the palate, ε is the strain tensor, δ is the Kronecker's delta, E is the Young's modulus and υ is the Poisson's ratio. Finite element method (FEM) was utilized to solve the governing equations for soft palate.

In the fluid domain, CFD is used to simulate airflow through human upper airway. The FSI requires iteratively update of the interface movement in both the fluid and structural domains. However, the CFD uses Eulerian coordinate for all the variables such as pressure and velocity, and with Eulerian coordinate all the nodes are presumed as fixed points through the whole simulation process; while the FEM, using Lagrangian coordinate, allows the mesh to move with the materials of structure. Therefore a finite element formulation, Arbitrary Lagrangian Eulerian (ALE) method, is introduced in to the fluid domain to allow all the nodes moving along with the FSI interface. The equations for computational fluid domain, governed by ALE formulation, are given below:

$$\nabla \bullet \vec{u} = 0 \tag{2.29}$$

$$\rho \frac{\partial \vec{u}}{\partial t} + \rho(\vec{u} - \vec{w}) \bullet \nabla \vec{u} - \nabla \bullet \vec{\tau} = 0 \tag{2.30}$$

here $\vec{w}$ denotes the moving coordinate velocity. In order to automatically determine the displacements of the nodes that can arbitrarily be moved, the Laplace equation below is solved to update the nodes of fluid domain with the deformation of the FSI interface

$$\nabla^2 \Delta \vec{d} = 0 \tag{2.31}$$

where $\Delta \vec{d}$ is the increment of the displacement. The latest displacements of nodes in fluid domain are then updated by adding the incremental solutions.

The displacement compatibility and traction equilibrium of the fluid/structure interface are governed by the equations below (Bathe and Zhang, 2004):

$$\vec{u}_f = \vec{v}_s \tag{2.32}$$

$$\vec{n}_f \bullet \vec{\tau} = \vec{n}_s \bullet \vec{\sigma} \tag{2.33}$$

where $\vec{u}_f$ is the displacement of the interface in fluid computational domain and $\vec{v}_s$ is the displacement of the interface in structural computational domain.

2.4.2 Numerical methods

Commercial software ADINA is used for solving all the equations of fluid, structure and FSI interface. FEM is applied for the structure and FVM is applied for the fluid. Iterative computing of two-way coupling is used to solve the equations as described below:

- Solve the fluid solution from the fluid equations
- Check whether the stress over the FSI interface is converged against the preset tolerance
- Solve the solid solution from the structural equations
- Update the fluid nodal positions from the displacement of FSI interface in the structural domain
- Check the displacement residual against the preset tolerance. If the iteration has not converged yet, the program goes back to the first step and continues for the next iteration. When both the displacement and stress tolerances are satisfied, the program will stop and save the fluid and solid solutions.

The convergence criteria for stopping the FSI iteration process are given by the equations below:

$$R_f < 0.001, \quad R_d < 0.001 \tag{2.34}$$

where R_f is the scaled force residual over the FSI interface, and R_d is the scaled displacement residual over the FSI interface.

As a well-tested software, ADINA has been extensively utilized to simulate FSI-related biomechanical problems such as interaction between blood flow and arterial wall (Tang et al., 1999a; Tang et al., 1999b; Valencia and Baeza, 2009), blood flow and human heart (Cheng et al., 2005; Doyle et al., 2010; Shim et al., 2003), blood flow and aneurysm

(Leung et al., 2006; Molony et al., 2009; Valencia and Solis, 2006), and blood flow and atherosclerotic plaques (Tang et al., 2004). Particularly, Malve et al. (2010), by simulating the interaction between airflow and human trachea using ADINA, proved that the results agreed well with experiments. This case is quite similar to the current study as an air/soft tissue interaction project in human respiratory system. ADINA has been used to simulate FSI mechanisms around the retropalatal region as well (Huang and Rong, 2010; Huang et al., 2007). More details could be found in ADINA manual (ADINA R & D, 2010).

2.4.3 Grid dependency test

The same mesh criteria as mentioned in section 2.3.3 is used for this study, where the airway and soft palate are discretized with element size of 0.6 mm using tetrahedron elements. The total numbers of elements of the airway and soft palate are 1,092,029 and 30,226, respectively. By refining the model to double of the current element numbers for both the fluid and structure domains, the differences of the maximum displacement of the soft palate and the total integrated force over the FSI interface are less than 2%. Therefore the current discretization method is converged and is utilized in the simulations to reduce the computational cost.

Chapter 3 Nasal Airflow Patterns among Caucasian, Chinese and Indian Individuals

During the evolution, human beings have developed different attributes of nasal morphologies among different ethnic groups (groups of subjects of different ancestral origins). Evolutionary adaptation of the nose to climate to optimize respiratory heat and moisture exchange in nasal mucosa, primarily to prevent ciliary and lung alveoli damage, as well as to moderate body water loss and maintain thermal equilibrium was considered to be one of the main reasons for such differences (Franciscus and Long, 1991). For example, nasal indices, defined as the ratio between nasal breadth and nasal height multiplied by 100, are different among ethnic groups (Davies, 1932; Leong and Eccles, 2009). The nasal indices are associated with latitude, which underlies variation in temperature and humidity (Franciscus and Long, 1991; Newman, 1953). However, the profound mechanism of how the nasal airflow interacts with variation of nasal morphology among ethnic groups is still unknown.

The current chapter, therefore, compared nasal airflow patterns among nasal cavities of three individuals: one Caucasian, one Chinese and one Indian. Three 3D nasal models were constructed from CT scans of these subjects. CFD simulations at a flow rate of 10 L/min were carried out using the three models by solving equations 2.1 and 2.5 presented in chapter 2. The velocity, pressure and streamlines of the airflow in nasal cavities of these three subjects were evaluated and compared.

3.1 Materials and methods

The ages of the subjects range between 26 and 41. The process depicted in sections 2.1 and 2.2 of chapter 2 were processed to build and discretize the models using MIMICS and HYPERMESH. As shown in Figure 3.1, three coronal cross sections were defined along the nasal passage: section A was located near the head of the inferior turbinate; section B was located at the middle nasal airway and right below the olfactory bulb; and section C was located at the end of the middle turbinate. All of these cross sections were created perpendicular to the bottom section. In section B, four meatuses were defined to study the airflow flux distribution in the olfactory region, the middle meatus, the inferior meatus and the common meatus. In nasal airway domain, the airflow was considered as incompressible and quasi steady state. Zero-gauge pressure was prescribed on the semi sphere, and velocity magnitude corresponding to ventilation rate of 166.7 ml/s (10 L/min) was applied to the nasopharynx of the models.

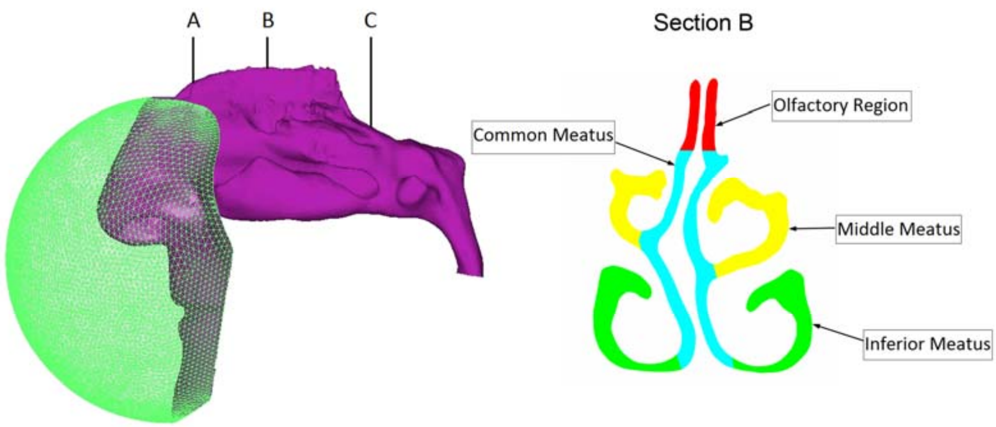

Figure 3.1 Model of the nasal cavity (Caucasian). Three coronal cross sections were defined: (A) at the inferior turbinate head; (B) at the middle nasal airway and right below the olfactory bulb; (C) at the end of the turbinates.

3.2 Results

3.2.1 Representation of the models

External shape and size of the nose. The nasal index is one of the most popular characteristics of the nose shape. A nasal index below 70 is described as leptorrhine and when above 85 it is platyrrhine. An intermediate index of 70-85 is described as mesorrhine. The leptorrhine, mesorrhine and platyrrhine nasal types are commonly associated with Caucasians, Asians and Africans, respectively (Leong and Eccles, 2009).

Table 3.1 shows general attributes of the nasal cavities of these three models. The nasal indices of Caucasian and Chinese models are comparable to the average nasal indices of their respective ethnic groups. The nasal index of Indian model is 88.5, which shows platyrrhine feature; the average indices reported among aboriginal tribes of India are between 74.3 and 95.1 (Macfarlane and Sarkar, 1941). As a high index indicates a broad nose and a low index a narrow nose, Figure 3.2 shows the nostril shapes of the three models, where the Caucasian nostrils are more longitudinal and the Indian nostrils are more transverse. The nostril shapes of these three models are similar to the nostril shapes of typical leptorrhine, mesorrhine and platyrrhine noses.

Table 3.1 General nasal attributes of the subjects.

	Nasal Breadth (cm)	Nasal Height (cm)	Nasal Index	Nasal Surface Area (cm^2)	Nasal Volume (cm^3)	Surface-area-to-volume ratio (1/cm)	Nasal Index[a]
Caucasian	3.50	5.17	67.81	220.38	33.41	6.60	64.20
Chinese	3.72	5.18	71.95	256.49	39.53	6.49	73.2-80.2
Indian	3.96	4.47	88.53	207.01	31.43	6.59	-

[a] average nasal indices of males according to ethnicity in Leong and Eccles (2009).
- data not available

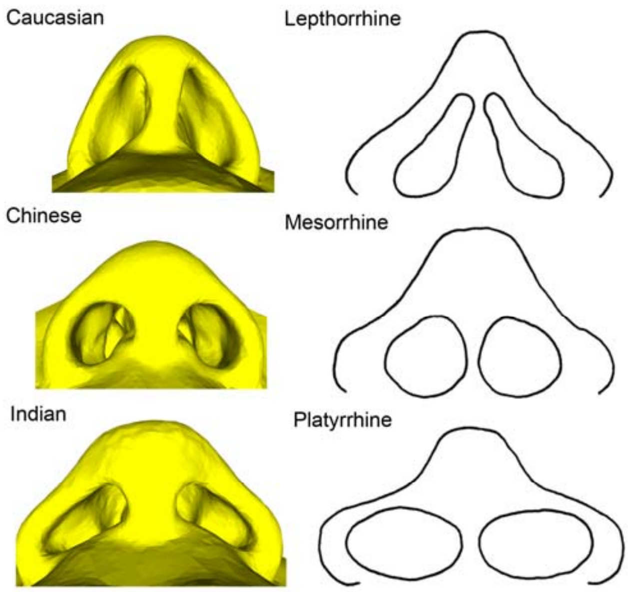

Figure 3.2 Nostril shapes of leptorrhine, mesorrhine and platyrrhine. Nostril shapes from current models are on the left, from Leong and Eccles (2009) are on the right.

Internal nasal cavity. The internal nasal cavity has mainly been studied in terms of cross-sectional area (CSA) and surface-area-volume ratio (SVR, defined as surface area of one domain divided by the volume of the domain), while knowledge for geometrical differences of nasal cavities among races is limited. Yokley (2009) reported that the epithelial SVRs were not significantly different between the two groups of European American and African American. As shown in Table 3.1, the SVRs of the volumes between the nostrils and the end of the nasopharynx in these three models are also similar.

Acoustic rhinometry was used to evaluate the CSAs of the nasal cavity. Huang et al. (2001), studying a cohort of Chinese, Malays and Indians, reported no statistical differences among the MCAs. According to their report, the inter-individual variations of the CSA along the coronal direction could be large. It is therefore difficult to extract any common ethnic characteristics of internal nasal morphology among the current three models. Figure 3.3 shows the CSAs of the three models along the coronal distance. The CSAs between the Indian and the Caucasian models are comparable. The CSAs in the Chinese model are generally larger than the other two. The average MCAs reported for Chinese and Indians are 1.5 cm^2 (Huang et al., 2001). In this study, the MCA of the nasal airway was obtained by measuring CSAs at a number of locations on planes with different surface normals and finding the smallest CSA near the nasal valve region. The mean MCAs of the left and the right nasal valve regions in Caucasian, Chinese and Indian models were determined to be 1.57 cm^2, 2.15 cm^2 and 1.27 cm^2, respectively. In the past, models with MCAs of 1.4 cm^2, 1.6 cm^2, 1.9 cm^2 and 2.0 cm^2 have been reconstructed and simulated (Wen et al., 2008).

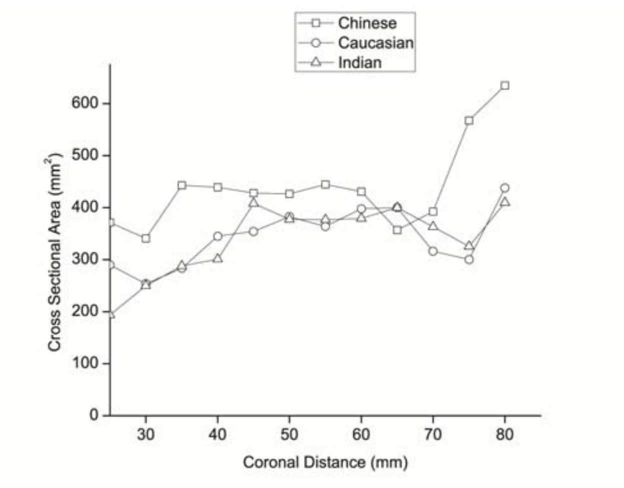

Figure 3.3 Cross sectional areas along the coronal direction. Location zero is at the nasal tip.

3.2.2 Velocity profiles of cross sections

Figure 3.4 shows the velocity profiles in the three cross sections. At the head of the inferior turbinate, velocity profile is similar between left and right nasal airways in the Chinese model, where the mainstream distributes at the lower two thirds of the cross section; velocity magnitude in the upper portion is approaching zero. In the Caucasian and Indian models, the mainstream of the right airway is constrained to be in the lower half portion, with the mainstream of the left airway distributing in the lower two thirds. In sections B and C, as the airflow develops in the middle nasal airway, the velocity distributes more evenly through the airways compared to the turbinate head. Compared to the other two models, the superior region in the Indian model experienced lower flow velocity magnitude in all the three sections.

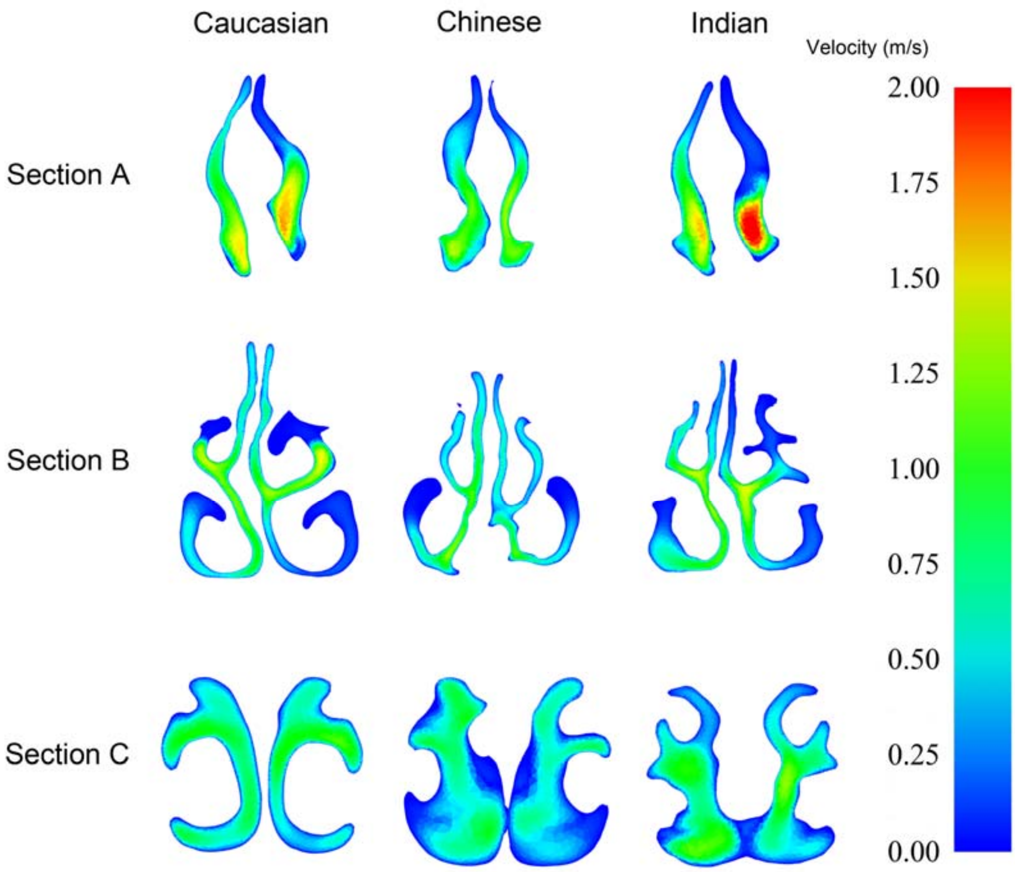

Figure 3.4 Velocity contours of cross sections of the three subjects.

Table 3.2 shows the equivalent hydraulic diameters and Reynolds number of the three cross sections calculated by the equation below:

$$D_H = \frac{4A}{P} \tag{3.1}$$

where D_H is the equivalent hydraulic diameter of the cross section, A is the area of the cross section and P is the perimeter of the cross section. The Reynolds number is given by

$$\mathrm{Re} = \frac{\rho u D_H}{\mu} \tag{3.2}$$

where Re is the Reynolds number.

The hydraulic diameters are comparable in cross sections A and B among the three models. Hydraulic diameters in cross section B are apparently smaller than in the other two sections which might be due to the curvature of the geometry of middle and inferior meatuses. The Reynolds number along the middle turbinate in the three models ranges between 82 and 240, which is below the critical Reynolds number for laminar-turbulent transition.

Table 3.2 Equivalent hydraulic diameters and Reynolds number of the three cross sections.

	Reynolds Number					
	Caucasian		Chinese		Indian	
	Left	Right	Left	Right	Left	Right
Anterior	220.81	226.92	185.21	181.41	239.30	236.27
Middle	105.35	93.81	86.13	82.89	111.77	104.28
Posterior	184.26	189.57	159.82	165.51	186.65	190.46

3.2.3 Flow distribution in the nasal airway

To determine flow flux through one specific plane, normal velocity was integrated over the given area using the equation listed below:

$$Q_A = \iint_A \vec{n} \bullet \vec{u} dA \tag{3.3}$$

where Q_A is the flow flux through the plane A, $\vec{n}$ is the normal vector of the plane.

Figure 3.5 shows the flow flux distribution through the three parts of the coronal cross sections: the superior, the middle portion and the inferior. In section A, the height of the airway was divided evenly into three parts; Section B was separated at the olfactory slit and the middle turbinate; Section C was separated at the middle and the inferior turbinate. At the turbinate head, the flow flux mainly passes through the lower third of the nasal cavity, followed by the middle portion in the Chinese and Indian models. In Caucasian model, the flow flux in middle portion is slightly larger than that in the inferior portion. In section B, the middle portion turns out to be the main passage of the airflow in the middle nasal airway in the Chinese model, while the inferior portion remains to be the main passage in the Indian model. The highest flow flux in the middle portion of all the three coronal cross sections appears in the Caucasian model, while in sections A and B, the highest flow flux in the inferior appears in the Indian model. The superiors of the three sections were found with the least flow flux in all the three models, especially in the Indian model.

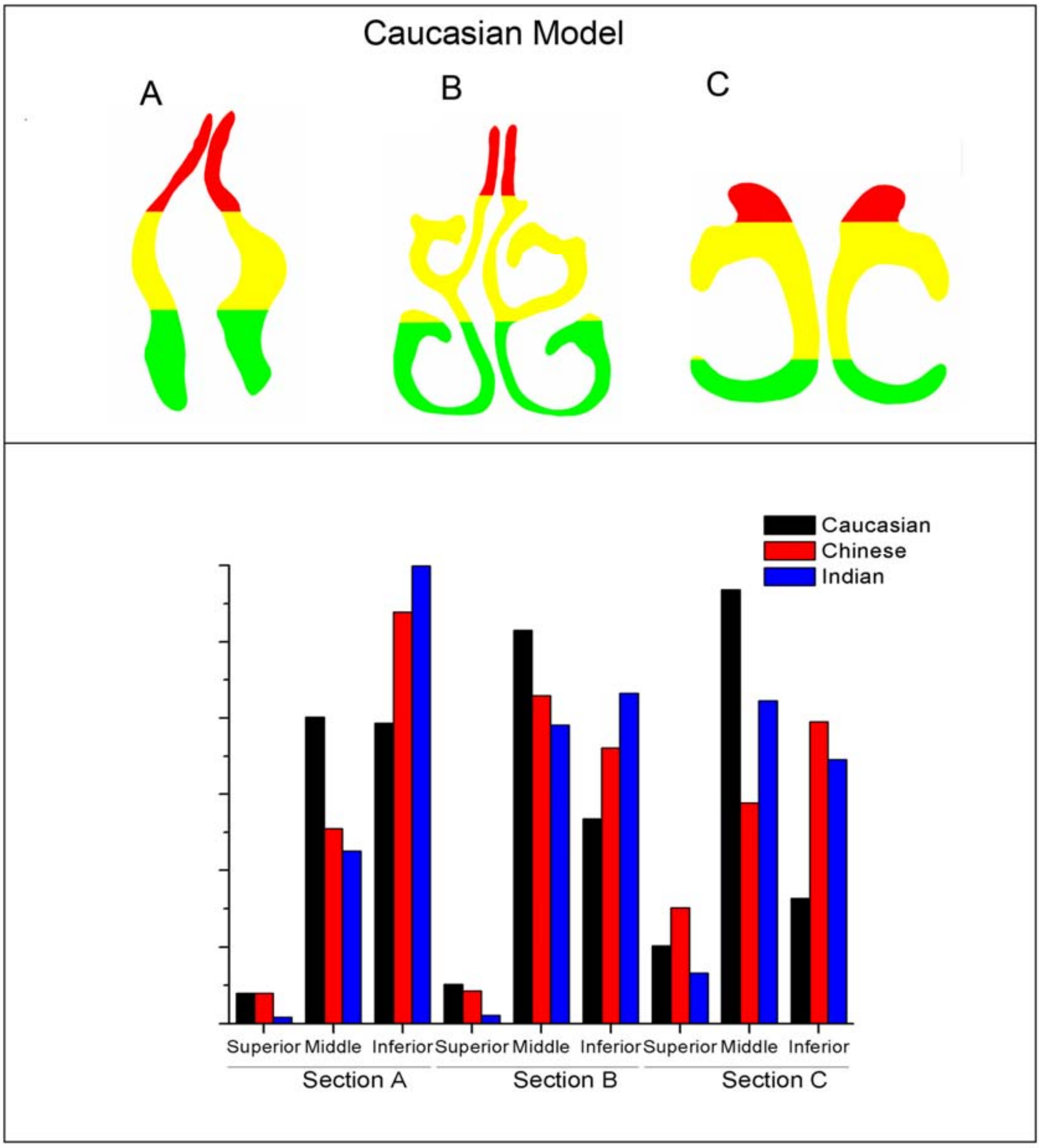

Figure 3.5 Flow flux through the superior, the middle and the inferior portions in the three cross sections of the three subjects.

Table 3.3 shows the flow flux through different meatuses of the two middle airways in section B. Among all the three cases, flow fluxes through the left nostrils are larger than the right ones. The common meatuses were found with the most flow fluxes passing through except for the right passage in Caucasian model, where more than 35% airflow passes through the right middle meatus. Less than 10% flow flux was found to flow through the olfactory region in Caucasian (6.16%) and Chinese (5.18%) models. This is consistent with reported studies, where the flow flux through the olfactory region accounted for 5-14% of the gross flow rate (Keyhani et al., 1997; Zhao et al., 2004). However, only 1.31% flow flux was found in the olfactory region in the Indian model. The flow flux through the left olfactory region is generally larger than through the right olfactory region. In addition, the highest flow flux in the inferior meatuses was found in the Indian model, and in the middle meatuses was found in the Caucasian model.

Table 3.3 Flow flux through the four meatuses of left and right nasal airways in cross section B.

	Caucasian		Chinese		Indian	
	Left Flow Flux (ml/s)	Right Flow Flux (ml/s)	Left Flow Flux (ml/s)	Right Flow Flux (ml/s)	Left Flow Flux (ml/s)	Right Flow Flux (ml/s)
Olfactory Region	5.90	4.36	6.31	2.32	1.70	0.48
Middle Meatus	16.41	35.94	14.30	14.42	20.15	19.41
Inferior Meatus	19.17	6.40	13.21	14.22	33.55	8.10
Common Meatus	47.12	31.50	63.33	38.64	37.22	46.06
Total	88.60	78.20	97.15	69.60	92.62	74.05

3.2.4 Average pressure of the CSAs

Figure 3.6 shows the mean pressure of the three cross sections in the three cases. Pressure at location x=0 represents zero ambient gauge pressure at the nasal tip. The decreasing patterns of pressure along coronal direction in Caucasian and Chinese models are almost the same. Compared to the other two models, the pressure was found to decrease faster between the nostrils and the turbinate head in Indian model; between sections B and C, the gradient of the pressure drop is similar among these three models.

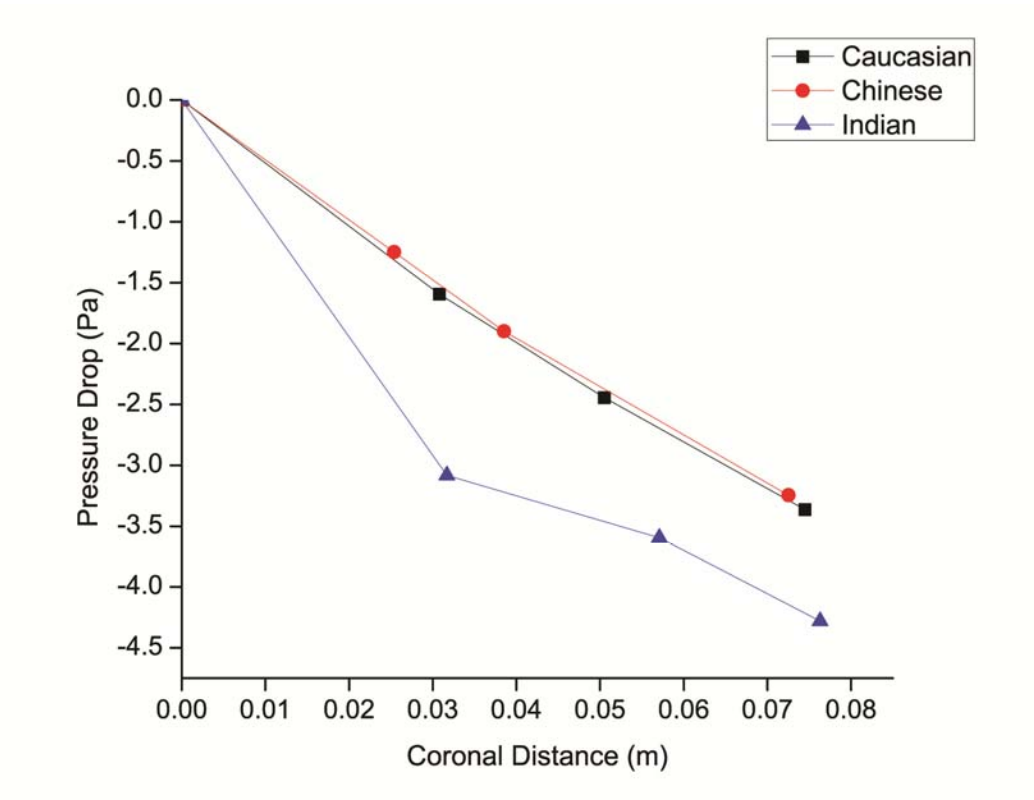

Figure 3.6 Mean gauge pressure of the cross sections. The gauge pressure at location zero stands for the zero ambient gauge pressure at the nasal tip.

3.2.5 Streamlines of left and right nasal airways

Figure 3.7 shows the streamlines of left and right nasal cavities of the three models. The velocity magnitude within the hemisphere is apparently lower than that at the nasal vestibules, which shows good agreement with the ambient static assumption at the hemispheric inlet. The airflow passing through the hemisphere accelerates at the nasal vestibule. After that, patterns of jet flow are shown due to the expansion of the anterior nasal passage where the velocity magnitude at the middle passage is larger than the sideways. The main stream of the jet is guided to be parallel to the nasal wall at the nasal valves.

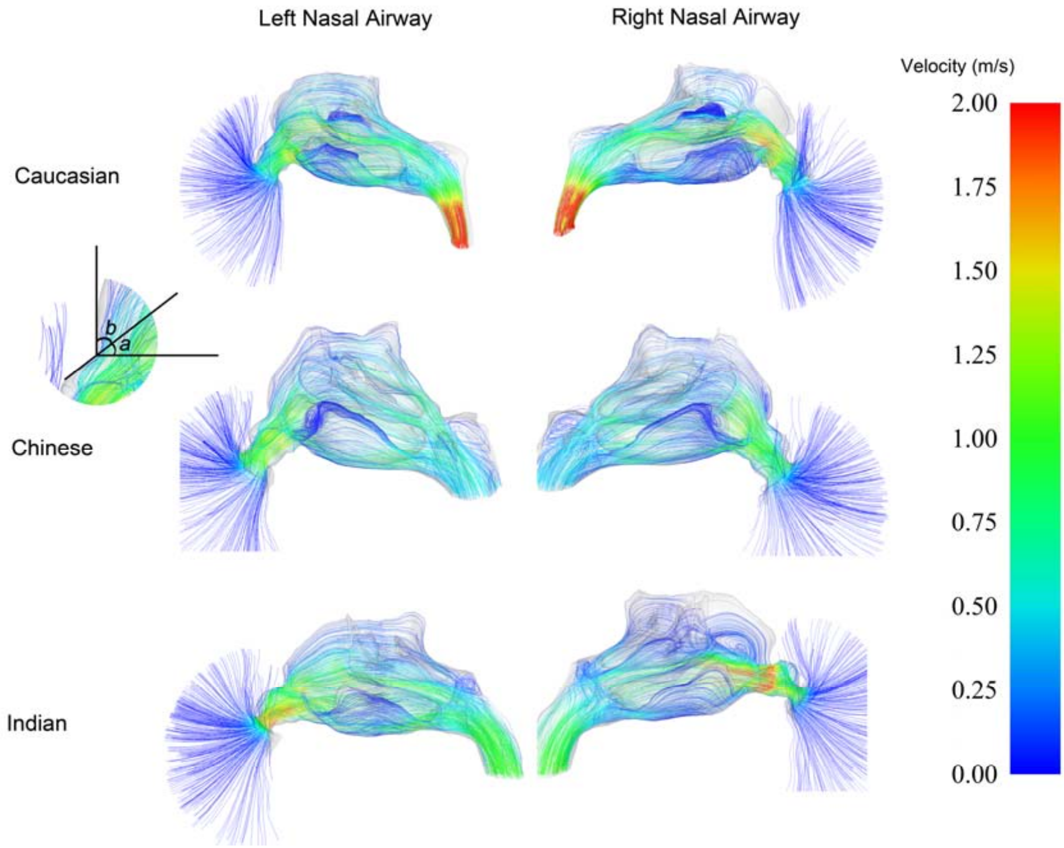

Figure 3.7 Streamlines of left and right nasal airways in the three models. *a*, the angle between the upper nasal valve wall and the bottom of the nasal cavity; *b*, the angle between the upper nasal valve wall and the anterior head of the nasal cavity.

In Table 3.4, an angle between the upper wall of the nasal valve and the bottom of the nasal cavity named *a* was defined to describe the direction of the mainstream at the nasal valve (shown in Figure 3.7). Angle *a* in the Caucasian and Chinese models are comparable, where the mainstream are guided upwards to approach the middle-height area of the airway; while in Indian model, this value is obviously smaller than the other two, and the mainstream near the anterior head of the nasal cavity even at the mid-position of the middle turbinate is flat and close to the nasal bottom.

Table 3.4 Values of angles *a* and *b* in the three models.

	Caucasian		Chinese		Indian	
	Left	Right	Left	Right	Left	Right
Angle *a* (°)	39.2	35.7	38.6	41.1	15.7	-10.4
Angle *b* (°)	97.6	118.0	50.2	96.6	66.6	130.8

With flow rate of 166.7 ml/s, swirls were found at the anterior passage airway, inferior and middle meatuses and nasopharynx. Streamlines of right nasal airways in the Caucasian and Indian models were found with larger-scale swirls at the anterior heads compared to the left airways. In the Chinese model, small-scale swirl was found in the same area of the right airway, but none in the left airway. The formation of swirls at the anterior nasal head might be due to the abrupt change of the nasal morphology. In Table 3.4, angle *b* was defined as the angle between the upper nasal valve wall and the anterior nasal head to describe the extent of the change of the anterior nasal morphology (shown in Figure 3.7). The smallest angle *b* was found in the left airway of the Chinese model, where no swirl emerges in this area. With the values of angle b ranges between 51º and 100º, small swirls were found near the anterior head of the left airways in the Caucasian and Indian models, and the right airway of the Chinese model. With angle *b* above 118º, large swirls were found near the anterior heads in the right airways of the Caucasian and Indian models.

3.3 Discussion

The results show clear differences of both nasal morphology and nasal airflow patterns, especially in the anterior nasal area among the three cases. These findings indicate that the variation of the different nasal proportions among these three subjects do have consequences on the nasal airflow patterns.

The nasal valve region was generally agreed to account for half of the total nasal resistance. In this study, with larger MCA, pressure drop at inferior turbinate head in the Chinese model is comparable with the Caucasian model. The anterior nasal morphology might be more important to anterior pressure gradient compared to MCAs. In addition, although the CSAs in the Chinese model are generally larger than the Caucasian and Indian models, the pressure gradient along coronal direction within the internal nasal cavities are similar in all the three models. The pressure gradient along the middle turbinate is insensitive to CSAs among these three models.

The main stream of the airflow initially locates at the inferior of the nasal airway between the nostrils and the turbinate head due to the bending of the nasal wall. As the airflow develops in the middle nasal airway, the mainstream shifts towards the middle passage of the coronal cross section. This is similar to the flow patterns in a curved pipe, where the high-speed area right behind the turn appears at the inner side of the pipe, while the fluid in the middle portion of the passage would be restored after the turning (Sudo et al., 1998). The Indian model was found to be with the most airflow passing through the inferior in sections A and B; the flow flux is apparently lower than the other cases through the superior. One of the reasons to explain this phenomenon might be that the jet flow at the nasal valve was guided by the nasal valve wall. With a lower angle a, airflow at the anterior nasal head tends to jet along the nasal bottom. In addition, the features of nostril shapes might be another factor to influence the distributions of flow flux in anterior nasal airway. With a longitudinal leptorrhine nostril shape in the Caucasian model, it is easy for airflow to reach the middle portion of the passage; while in the Indian model with platyrrhine nostril, airflow could be constrained in the transverse area, thus rarely flows upwards. In both section A and section B, the highest flow rate through the inferior region appears in the Indian model, followed by the Chinese and Caucasian models. On the contrary, the highest flow rate through the middle portion appears in the Caucasian model, followed by the Chinese and Indian models (Figure 3.5). The influence of anterior nasal morphology to airflow distribution in coronal CSAs could therefore reach the middle nasal airway.

The volume flow flux through the olfactory region in the Indian model (1.2%) is extremely low compared to the other models, which is abnormal according to reported studies. It is more difficult for the airflow to reach the olfactory region in the current Indian model. Despite the transverse nostril shape, relatively flat jet flow due to the smallness of angle a, and the largeness of angle b which induces large swirls in the anterior nasal area might be two other factors to account for the small flow flux in the olfactory region of the Indian model. Using a one-dimensional theoretical model, Hahn et al. (1994) reported that the odor intensity was correlated with local airflow velocity along the olfactory mucus. As lower flow rate in the olfactory region possibly implies smaller velocity magnitude along the olfactory mucus, odorants in the air might be less sensitive to the Indian subject than the other two subjects at the same inspirational flow rate. However, more models as well as evaluation of nasal odorant transport are needed to verify this in the future.

Vortexes were reported to appear around the nostrils, the nasopharynx, the anterior head and in the upper and lower meatuses (Keyhani et al., 1997; Subramaniam et al., 1998). Similarly, swirls were found near the anterior head, middle and inferior turbinates, and nasopharynx even at low flow rate (166.7 ml/s) in these three models. Since the flow regime is mainly laminar, the formation of vortexes near the turbinates and thereafter might be due to the curvature of the middle and inferior meatuses and the nasopharynx. Interestingly, the sizes of the anterior swirls were found to be correlated with the extent of the abrupt change of the anterior head. For an angle b as small as 51º, no swirl was found in the left airway of Chinese model. The size of swirls increases with the value of angle b. One of the reasons might be that a larger angle b implies larger spare volume above the main nasal passage, where the velocity of the airflow is lower and the pressure is higher. Vortexes could be easily formed due to the pressure difference between the anterior head and the main nasal passage.

Despite the difference in nasal indices, individual difference could also be vital to the variation of nasal morphology and nasal airflow patterns. Segal et al. (2008) compared the airflow patterns in four individuals at rest and found evident differences in nasal airflow distribution, pressure drop and helicity index among the subjects. Crouse and Laine-Alava (1999) indicated that gender and body mass indices were related to oral and nasal pressure and nasal airflow rate. It is therefore difficult to identify the characteristics of nasal morphology which determine nasal airflow patterns among individuals. However, during the evolution of human beings, the nasal cavity morphologies of different races do develop their own attributes either via human evolution or through human's adaptation to the environment, such as nasal index and nostril shapes, which allows us to distinguish nasal cavities of different ethnic groups and uncover the effects of these differences on the nasal airflow patterns and nasal functions.

3.4 Summary

By reconstructing three 3D nasal models, one Caucasian, one Chinese and one Indian, we evaluated nasal airflow at a flow rate of 7.5 L/min using CFD simulation. The nasal morphologies, the velocity field, the pressure filed and the airflow streamlines have been compared among these models.

External nose shapes and anterior nasal airways among the three subjects from Caucasian, Chinese and Indian are prominently different, which directly influenced the anterior airflow patterns. This influence continued along the whole nasal airway. With a longitudinal nostril shape and larger angle between upper vestibule wall and nasal bottom, flow flux in the Caucasian model tends to flow upwards at the nasal valve. On the other hand, flow flux in the Indian model tends to flow along the nasal bottom with transverse nostril and smaller angle a. Flow flux through the olfactory region in the Indian model was found to be lower than the other two models. The abrupt change of the anterior nasal airway described by angle b is one of the main determinants for the scales of the swirls near the anterior head. The decreasing pattern of pressure is insensitive to the coronal CSAs of the nasal passages.

The current models confirm that there are potential association between nasal proportions and nasal airflow patterns. However, whether this association supports the concept that, the nasal functions of different ethnic groups have been adapted to the respect climate to optimize respiratory heat and moisture exchange, is still unknown. Further investigations are needed to evaluate nasal functions among different ethnic groups.

Chapter 4 Case Studies of Airflow in Deformed Human Nasal Cavities

Chapter 3 investigated the effects of different nasal morphologies among ethnic groups on nasal airflow. Despite ethnic groups, there are many other factors that can cause significant variation of nasal morphologies among individuals, such as gender and body mass index (Crouse and Laine-Alava, 1999). Particularly, many common aesthetic or pathological reasons, such as aesthetic rhinoplasty, septal deviation, nasal trauma and facial bone fracture (Haarmann et al., 2009; Higuera et al., 2007; Kocer, 2001), can considerably deform human nasal cavity. The deformation of human nasal airway, sequentially, causes pathological consequences. For example, the deviation of nasal septum is one of the causes of nasal obstruction (Chen et al., 2009); even small change of nasal morphology around olfactory slit affects the intake of odor molecules and thus influence olfaction (Zhao et al., 2004). On the other hand, surgical intervention allows the morphology to be adapted to correct such deformation of nasal morphology. After surgical operation on patients suffered from facial bone fracture, the CSAs along the nasal cavity and the total volume of the nasal cavity were found to be largely increased, accompanied with a significant decrease of flow resistance (Haarmann et al., 2009). However, in-depth analysis on how exactly the surgical intervention changes the nasal airway morphology as well as nasal airflow patterns is still needed.

In addition, the deformation of human nasal airway can be troublesome even to surgeons, for example, deviated nose (or crooked nose). A deviated nose refers to appearance of deviated external nose due to deformity of nasal bones, upper and lower cartilages, nasal septum or a combination of any of these elements. The cause of deviated nose may be congenital or acquired secondary to previous trauma or surgery (Rohrich et al., 2002). Correction of the deviated nose has become one of the most challenging problems for septorhinoplasty due to the complex nasal structures and surgical techniques involved. A number of correction techniques have been proposed to treat crooked nose resulting from different deformed locations such as upper, middle or inferior third of external nose (Hoffmann, 1999; Okur et al., 2004; Pontius and Leach, 2004; Porter and Toriumi, 2002; Rohrich et al., 2002; Zoumalan et al., 2009). However, the current techniques are mainly concentrated on straightening and making the nose symmetrical with minimal focus on restoration of nasal airflow. Based upon the data collected from 260 patients, Foda (2005) reported that breathing was improved in 80% of the patients with both deviated nose and nasal obstruction mainly resulted from straightening of the nasal septum and widening of the nasal valve region. Still the nasal morphology in the other 20% of the patients did not obtain sufficient correction through surgical intervention to restore a normal breathing. More efforts are therefore needed for restoration of nasal airflow in deviated nose during surgery.

The current chapter evaluated two case studies of airflow in deformed nasal cavities in terms of surgical intervention and deviated nose. In section 4.1, 3D nasal models were constructed to evaluate both pre- and post-operative airflow patterns in the nasal cavity of a patient with orbito-maxillary bone fracture. CFD simulations at flow rate of 10 L/min within these two models were carried out. The airflow streamlines, wall shear stress, velocity distribution, flow partitioning and nasal resistance in nasal cavity were calculated and compared between the pre- and post-operative models. In section 4.2, 3D models of nasal cavities of four male subjects (one subject with un-deviated nose, one with S-shaped deviated nose, one with C-shaped deviated nose and one with slanted nose) were reconstructed. Laminar flow model was used to simulate calm breathing at flow rate of 167 ml/s (10 L/min), while LRN k-ω turbulent model was used to simulate breathing during light exercise at flow rate of 500 ml/s (30 L/min). Airflow properties such as flow partitioning, path-lines, wall shear stress and nasal resistance were calculated and compared among these four cases.

4.1 Effects of bone fracture and rhinoplasty on nasal airflow

4.1.1 Materials and methods

CT scans of a 27-year old Chinese male with orbito-maxillary fracture were obtained. This patient suffered from a displaced fracture of the left orbital floor, left medial maxilla, left infraorbital rim and left nasal bone due to a car accident. From an external view point his nose was straight, though there were symptoms of left sided nasal obstruction. Initial examinations show distortion of the bony pyramid with medial displacement of the left medial maxillary buttress and nasal bones. The ethmoid and the vomer regions were also fractured and displaced into the left nasal airway. The patient subsequently received ORIF operation.

Figure 4.1(a) shows axial views of the CT images of the patient before and after the surgery. Pre-operative CT scans show left medial maxillary, infraorbital rim and floor of orbit fractures with displacement of the medial buttress of the left maxilla into the left nasal cavity. During surgery, the left medial maxillary buttress was reduced anatomically and fixed with 1.5 mm plates and screws. Examinations were performed via ten coronal cross sections along the nasal airway (Figure 4.1(b) and (d)). Before the surgery, the left inferior portion and the superior region along the turbinates were collapsed. The inferior portion in post-operative model was partially restored, while the superior air space was still rather discontinuous. As shown in Figure 4.1(c), the CSAs along the right airway in pre- and post-operative models were comparable, while the CSAs of left airway in post-operative model were generally larger than pre-operative model. Particularly, the maximum increase of left CSA was found at cross section 5 (0.67 cm^2).

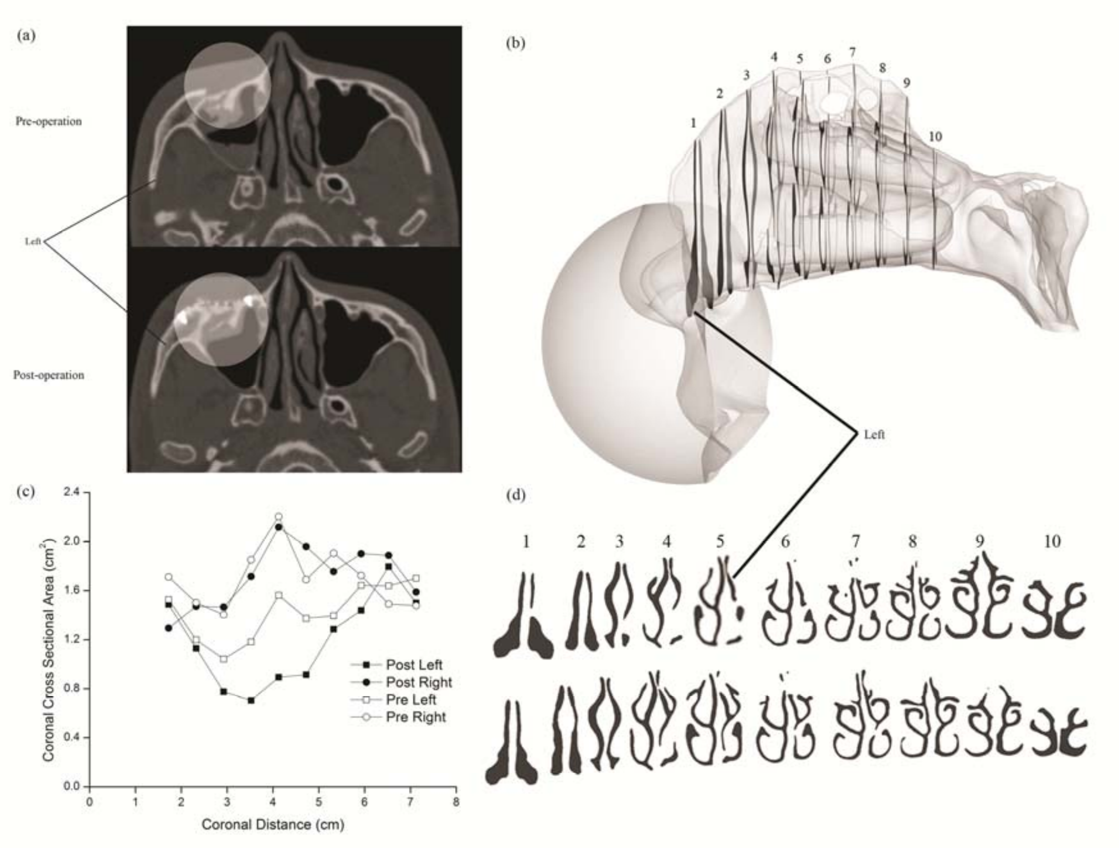

Figure 4.1 Nasal morphology. (a), axial CT image of study patient in pre- and post-operative models. (b), the post-operative model. 10 coronal cross sections were defined along the nasal airway. (c), coronal cross sectional areas along the airway. Coordinate zero was at the nasal tip. (d), front view of the 10 cross sections.

MIMICS and HYPERMESH were used to construct and discretize the models as described in sections 2.1 and 2.2 of chapter 2. Steady nasal airflow at 10 L/min was simulated in both the pre- and post-operative models. During the simulation, equations 2.1 and 2.5 were solved using ANSYS FLUENT.

4.1.2 Results

4.1.2.1 Nasal attributes

Table 4.1 shows the overall morphological properties of the nasal airways of the two models. Volumetric increase of 1.44 cm^3 was found in the left nasal airway in the post-operative model, while increase of 0.31 cm^3 was found in the right nasal airway compared to pre-operative model. The average minimum cross sectional area of nasal airway in Chinese was reported to be 0.75 cm^2 (Huang et al., 2001). The minimum cross sectional areas in left and right airways after surgery were slightly larger than they were in pre-operative model and comparable to minimum cross sectional areas in healthy nasal cavity. The surface-area-to-volume ratios of left and right airways were comparable between the pre- and post-operative models.

Table 4.1 General measurement in pre- and post-operative nasal cavities.

	Left Nasal Airway				Right Nasal Airway			
	MCA (cm^2)	Volume (cm^3)	Surface Area (cm^2)	SAVR (cm^{-1})	MCA (cm^2)	Volume (cm^3)	Surface Area (cm^2)	SAVR (cm^{-1})
Pre-operation	0.72	8.13	79.61	9.79	0.73	11.19	104.97	9.38
Post-operation	0.76	9.57	94.86	9.91	0.78	11.50	109.30	9.50

The surface area and the volume of nasal airway were measured between nostril and end of turbinates.
MCA, minimum cross sectional area of the airway.
SAVR, surface-area-to-volume ratio between nostril and turbinate end.

4.1.2.2 Velocity distribution

Figure 4.2 shows the velocity distribution of coronal cross sections at turbinate head, middle airway and turbinate end. At the turbinate head, the velocity distribution was rather symmetrical between the left and right airways with relatively smaller velocity magnitude in post-operative model due to the recovery of left inferior portion of the airway. The airflow also distributed more evenly through the middle airway, especially around the middle and inferior meatuses. However, the ORIF treatment failed to restore the airflow in superior region as the superior air space in middle airway was still quite narrow and discontinuous after the surgery. The velocity magnitude around the left middle portion of the middle and posterior airway in post-operative model was quite low due to the discontinuity along the middle portion of the left airway. Table 4.2 shows the proportional airflow through superior, middle and inferior thirds of the coronal section at the turbinate head (as depicted in Figure 4.3). Before the surgery, more than 51% airflow would tend to pass through the inferior third of both left and right airways. In the post-operative model, airflow through the middle and the inferior portions were almost identical. Airflow through the superior portion was also found to be apparently more intensive. The airflow partitioning between left and right airways was more evenly distributed as the proportional airflow through the left airway increased from 31.48% in the pre-operative model to 43.44% in the post-operative model.

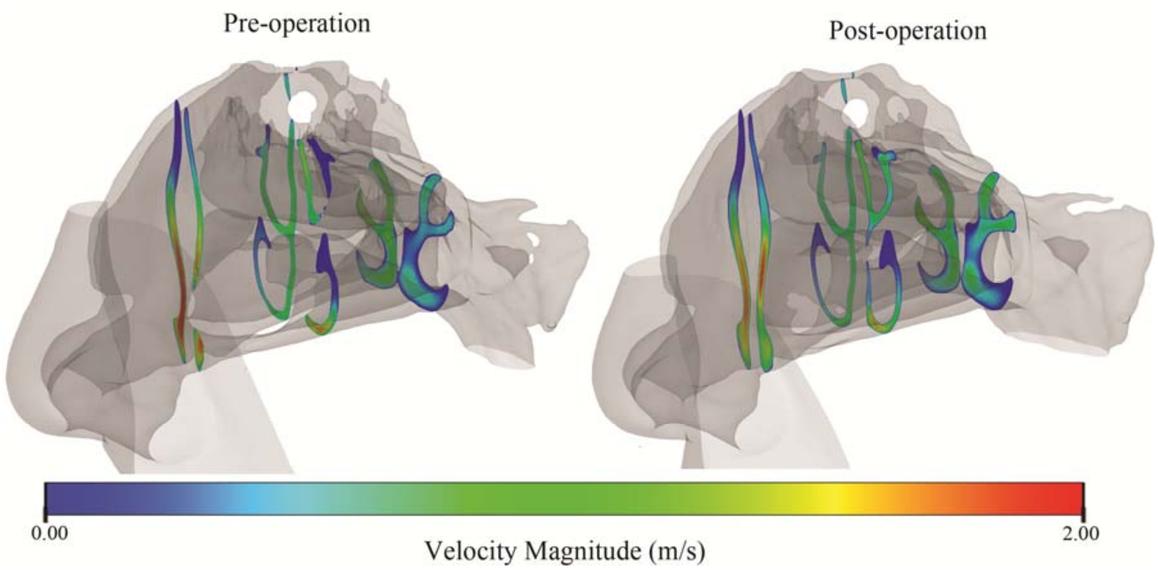

Figure 4.2 Velocity distributions of coronal cross sections at turbinate head, middle airway and turbinate end in pre- and post-operative models.

Figure 4.3 Cross sections in Table 4.2.

Table 4.2 Proportional airflow through superior, middle and inferior thirds at the turbinate head in left and right airways.

	Proportional airflow in left airway (%)				Proportional airflow in right airway (%)			
	Superior	Middle	Inferior	Total	Superior	Middle	Inferior	Total
Pre-operation	3.77	11.38	16.33	31.48	1.63	28.38	38.51	68.52
Post-operation	4.48	18.80	20.16	43.44	2.29	25.96	28.31	56.56

4.1.2.3 Pressure drop

Table 4.3 shows the mean pressure at the nasal valve and the turbinate end and nasal resistances of left and right airways. The average pressure at the turbinate end increased from negative 7.40 Pa to negative 5.35 Pa after the surgery. The nasal resistance of the left nasal airway in pre-operative model was found to be apparently larger than the right nasal airway and the airways in post-operative model due to collapse. The nasal valve region usually accounted for half of the nasal resistance. Before the surgery, the average pressure drop around left and right nasal valves were found to be 10.41% and 43.51% of the pressure drop at the turbinate end, respectively. While after the treatment, the proportions of average pressure drops at left and right nasal valves increased to 29.35% and 45.61%, respectively. The overall flow resistance increased from 0.04 Pa·s/ml in pre-operative model to 0.03 Pa·s/ml in post-operative model.

Table 4.3 Mean pressure at nasal valve and turbinate end and nasal resistance in left and right airways.

	Mean pressure at nasal valve (Pa)		Mean pressure at turbinate end (Pa)	Nasal Resistance (Pa.s/ml)		
	Left	Right		Left	Right	Total
Pre-operation	-0.77	-3.22	-7.40	0.14	0.06	0.04
Post-operation	-1.57	-2.44	-5.35	0.07	0.06	0.03

4.1.2.4 Streamlines

Figure 4.3 shows the streamlines of left and right airways in the pre- and post-operative models. In the left nasal airway, the airflow was separated into two branches along the turbinates due to the collapse of the airway of superior and middle regions in pre-operative model. High velocity magnitude was found around the collapsed area of the anterior airway. The left streamlines were partially restored in middle and superior regions in post-operative model, but still not as continuous as streamlines in the other nasal airway due to regional collapse. In the right nasal airway, the velocity magnitude was lower in post-operative model than pre-operative model due to lower volume flow rate. The airflow circulation in right anterior airway was found to shift towards the anterior head of the airway with the size of vortex to be decreased.

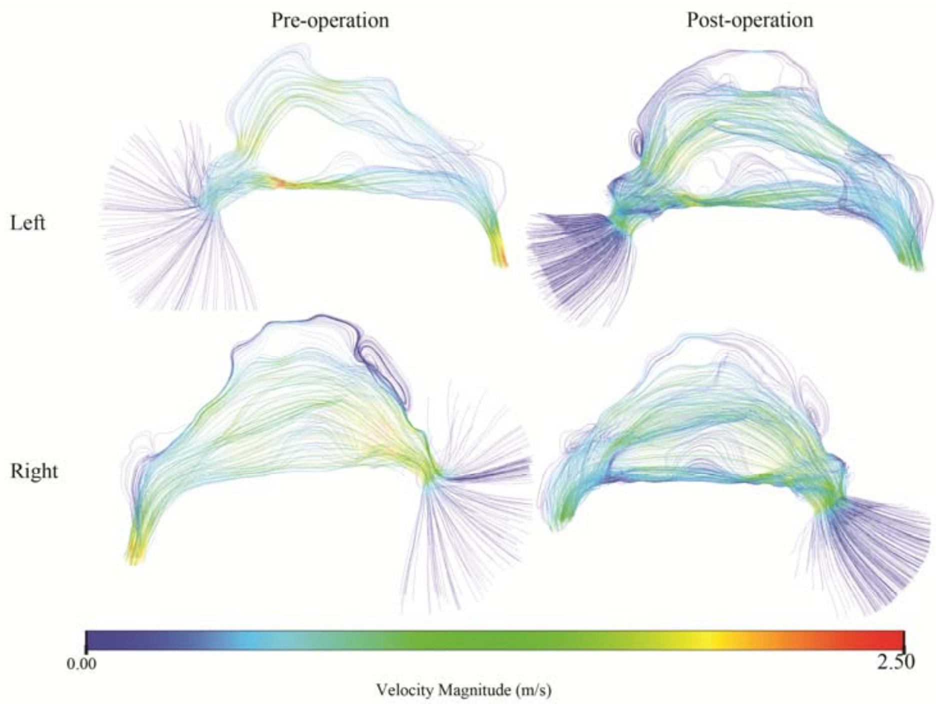

Figure 4.4 Streamlines of left and right airways in pre- and post-operative models.

4.1.2.5 Wall shear stress distribution

Figure 4.5 shows the wall shear stress contours of the nasal wall in the two models. From the left view, high wall shear stress magnitude was found around the collapsed region possibly due to higher velocity magnitude in pre-operative model. While in post-operative model, the left wall shear stress magnitude decreased as the air space was restored after the surgery. From the right view, the wall shear stress was generally larger in pre-operative model than post-operative model due to higher airflow rate through the right airway. Maximum wall shear stress decreased from 0.49 Pa in pre-operative model to 0.42 Pa in post-operative model at flow rate of 167 ml/s.

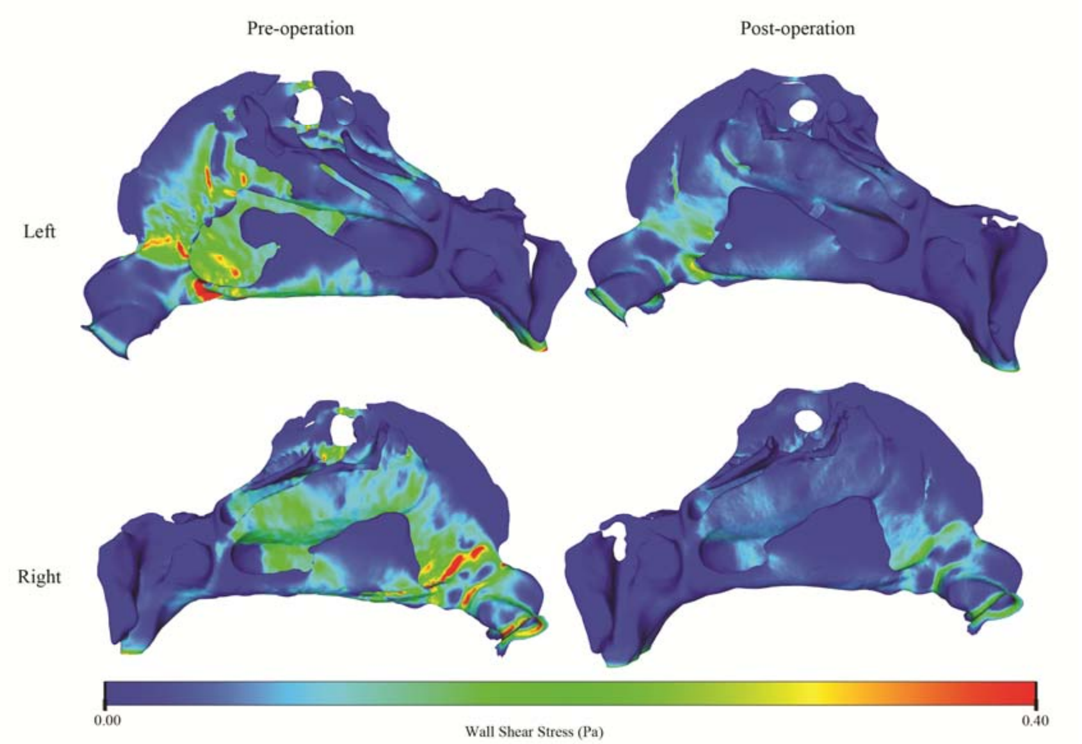

Figure 4.5 Wall shear stress contours of left and right airways in pre- and post-operative models.

4.1.3 Discussion

Traumatic distortion of the nasal airway anatomy can occur with facial bone fractures, leading to obstruction of nasal airflow. Facial bone fracture and reduction of the fracture might significantly change the airflow patterns. In this study, the flow patterns in models before and after the fracture reduction from one patient with orbito-maxillary bone fracture were compared in order to assess the effectiveness of fracture reduction to nasal airflow.

Morphologically, the orbito-maxillary fracture distorted the left inferior portion and superior region of middle nasal airway with a considerable decrease of left nasal volume as compared to right nasal airway. Zhang et al. (2008) reported that the rhinomanometric nasal airflow resistances were significantly close correlated with acoustic rhinometric nasal airway volumes. Therefore, the collapsed space in left nasal airway might significantly increase the overall nasal resistance. The surgical intervention generally increased the left CSAs along the nasal airway with less change in right nasal morphology. Based upon four healthy human nasal cavities in Garcia et al. (2007)'s report, the average volume per nasal airway between nostril and end of the septum was found to be 10.61 cm^3. The average volume of left and right nasal airways has been increased from 9.66 cm^3 in pre-operative model to 10.54 cm^3 in post-operative model. However, the operation failed to fully restore some detailed morphology of the nasal airway, such as the collapsed superior region of the airway and the discontinuous middle portion of the left middle airway.

33.3% decrease of nasal resistance was found in post-operative model compared to pre-operative model. This is possibly due to the increased left nasal volume and increased minimum cross sectional area around the nasal valve. Compared to post-operative model, the collapse of left airway in pre-operative model also resulted in less proportion of nasal resistance from left nasal valve due to increased resistance in middle airway. The flow partitioning between the two airways, the velocity magnitude through the airways and the wall shear stress distribution of the nasal wall were restored after the operation. However, some of the local distributions of flow properties in post-operative model still show abnormity. There was still limited airflow passing through the superior portion of the airway such as the olfactory region which might influence the efficiency of olfaction. However, as Zhao et al. (2006) reported improved olfactory capability after surgical intervention even much of the olfactory cleft and superior meatus in post-operation model were blocked, further study of olfaction such as simulation of odorant delivery and clinical measurements of olfactory capability are needed to evaluate the effects of orbito-maxillary fracture and surgical intervention on olfactory efficiency. The collapsed area of the middle portion of left middle airway in post-operative model resulted in fewer streamlines through this region compared to right nasal cavity. The discontinuity of the middle airway also induced low velocity magnitude at the middle portion around the turbinate end (Figure 4.2).

The formation of circulation flow in anterior airway was found to be correlated with the morphology of the anterior nasal head (Zhu et al., 2011). Compared to pre-operative model, the size of the right anterior vortex in post-operative model was reduced with the vortex location shifted towards the anterior nasal head. This might be due to the decreased airflow in right airway of post-operative model which could decrease the size of the vortex and move it upstream (Keyhani et al., 1997).

4.2 Effects of deviated external nose on nasal airflow

4.2.1 Materials and methods

4.2.1.1 Study Patients

Subsequently, we evaluated effects of another cause of nasal deformation on airflow, namely, the deviated external nose. CT images of four male subjects aged between 21 and 56 years old were recruited. Figure 4.6 shows the external noses and the axial and coronal views of anterior nasal cavities in S-shaped, C-shaped and slanted cases. The external noses denoted apparently S-shaped, C-shaped and slanted deviated patterns. According to the axial view, the anterior septum cartilage was twisted in S-shaped case, while deviated to the right in C-shaped case and to the left in slanted case. In coronal view, the left anterior airways of S-shaped and C-shaped cases, and the right anterior airway of slanted case were partially compromised.

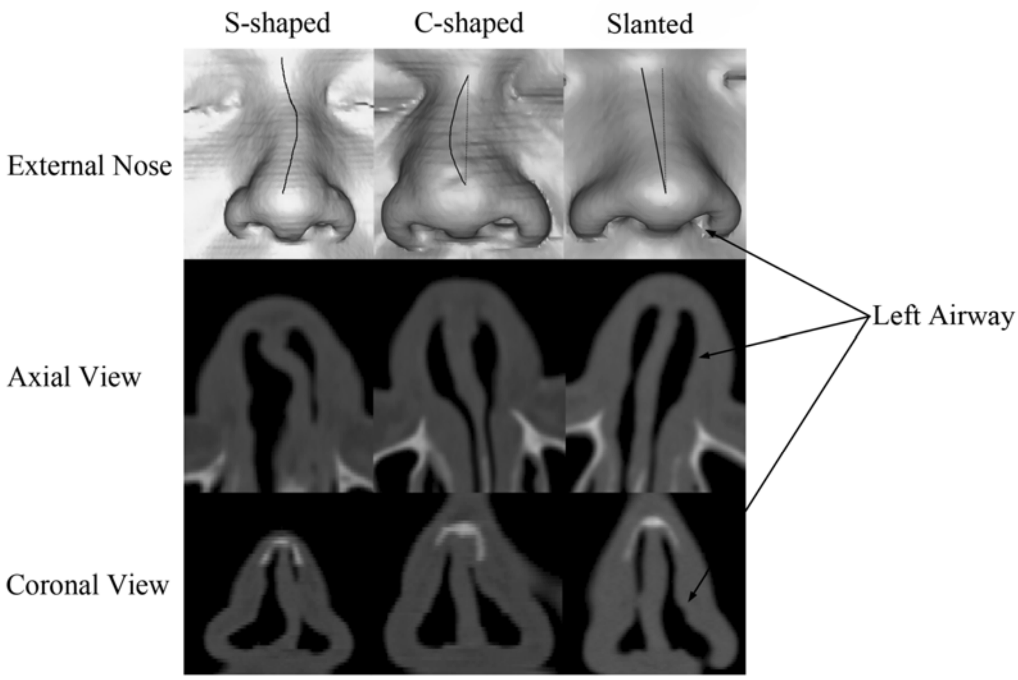

Figure 4.6 Study patients. The external shapes of nose of slanted, C-shaped and S-shaped cases were shown at the top. The images in the middle and the bottom show axial and coronal views of anterior nasal airways, respectively.

4.2.1.2 Nasal morphology

Figure 4.7 shows the reconstructed models of crooked noses. In Figure 4.7(a), one of the anterior nasal roofs was collapsed in all the three models with deviated noses, but in different manners. A sharp angle was formed between the anterior roof and upper wall of nasal vestibule in slanted case, while a right angle was formed in S-shaped case. In C-shaped case, only the upper portion of the anterior roof was collapsed. The original cross sections along the turbinate in cases with crooked noses are presented in Figure 4.7(b). The superior patency of nasal airway was discontinuous in all the three cases. The left inferior regions of S-shaped and C-shaped cases and the left middle region of S-shaped case were collapsed. The left middle airway of slanted case was severely blocked. To eliminate the influence of internal blockage in order to determine the effect of the external nasal deformity alone on nasal airflow, the collapsed region along the turbinate was artificially reopened in all the three cases with deviated noses (Figure 4.7(c)). The collapsed and reopened regions along the turbinates were indicated by arrows. This process was done by manually filling the collapsed region along the turbinate in coronal cross sections in Mimics with the anterior nasal airway remained unchanged and rebuilding the models.

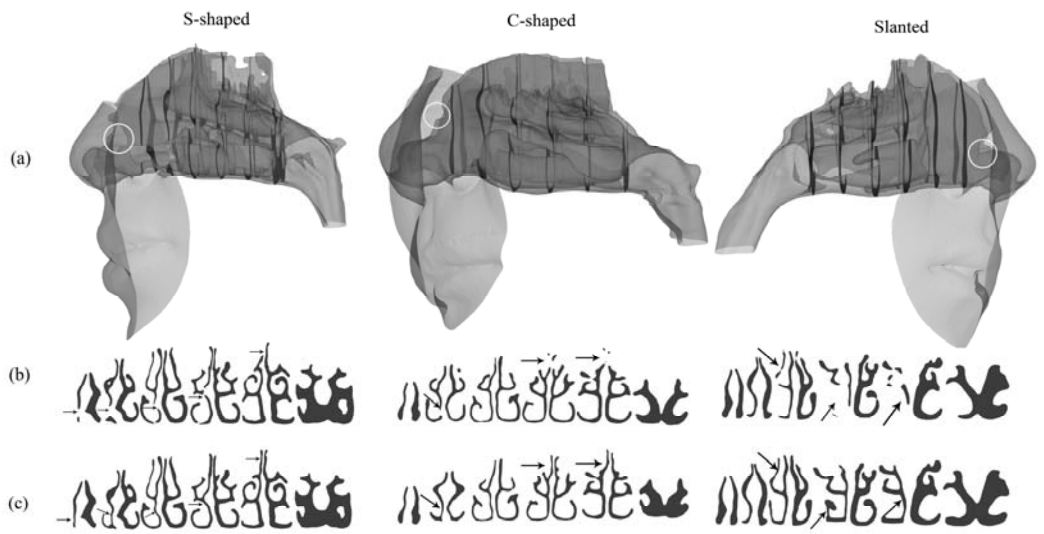

Figure 4.7 Nasal morphology. (a), transparent side views of nasal cavities, where the white circles show collapsed anterior nasal roof due to deviation of external nose. (b), cross sections along turbinates in original models. (c), cross sections along turbinates in reopened models where the collapsed regions were artificially reopened. The arrows indicate regions that have been modified.

As shown in Table 4.4, the MCAs of the left airways of S-shaped and C-shaped cases, and the right airway of slanted case were obviously smaller than un-deviated condition due to the collapse of anterior nasal roof. The MCAs in the other airways were comparable to un-deviated model.

Table 4.4 Minimum cross sectional areas (MCAs) of left and right airways around the nasal valve.

	Un-deviated	S-shaped	C-shaped	Slanted
Left MCA (cm^2)	0.93	0.31	0.49	0.83
Right MCA (cm^2)	0.88	0.99	0.93	0.44

4.2.1.3 Simulations

In this study, nasal airflow was simulated at both flow rates of 167 ml/s and 500 ml/s. Laminar model was used for flow rate of 167 ml/s, where equations 2.1 and 2.5 were solved. LRN turbulent model was used to simulate nasal airflow at 500 ml/s in case that turbulence would be presented, where equations 2.1, 2.22, 2.23 and 2.24 were solved. ANSYS FLUENT was used to obtain the solutions of these equations.

Table 4.5 shows the models that were reconstructed and simulated at both flow rates of 167 ml/s and 500 ml/s. In addition to the nasal model of un-deviated case (model U), the other models are the nasal models of original deviated cases (models C1, S1 and I1) and the models of deviated cases with reopened middle and posterior nasal cavity (models C2, S2 and I2).

Table 4.5 Descriptions of nasal models.

	Un-deviated	C-shaped		S-shaped		Slanted (I-shaped)	
Models	Model U	Model C1	Model C2	Model S1	Model S2	Model I1	Model I2
Model Description	Nasal model of the healthy subject for comparison	Original nasal model of C-shaped subject	Nasal model of C-shaped subject with reopened internal cavity	Original nasal model of S-shaped subject	Nasal model of S-shaped subject with reopened internal cavity	Original nasal model of Slanted subject	Nasal model of slanted subject with reopened internal cavity

4.2.2 Results

4.2.2.1 Flow partitioning

Flow partitioning is defined as the proportion of the airflow through left and right airways. The flow partitioning in all the models was shown in Table 4.6. Flow partitioning through the left and right airways distributed more evenly in model U than original models with deviated noses (models S1, C1 and I1). Less than 4% airflow passed through the left airway of model S1 due to severe blockage of middle portion of the airway and external deviation. In models S2 and I2, flow partitioning was more even through the two airways compared to models of S1 and I1, respectively. Nevertheless, the reopening process did not influence flow partitioning in C-shaped case (models C1 and C2). This is possibly because that the airway was less blocked compared to the other two cases (Figure 4.7(b)). Flow partitioning through the left and right airways was almost the same at flow rates of 167 ml/s and 500 ml/s in un-deviated, S-shaped and C-shaped cases (models U, S1, S2, C1 and C2), while considerable change of flow partitioning was found in both I1 and I2 models (slanted case).

Table 4.6 Flow partitioning of the models at flow rates of 167 ml/s and 500 ml/s.

	Flow Partitioning at 167 ml/s (%)		Flow Partitioning at 500 ml/s (%)	
	Left	Right	Left	Right
Model U	58.40	41.60	55.35	44.65
Model S1	2.98	97.02	3.25	96.75
Model C1	39.05	60.95	39.67	60.33
Model I1	29.33	70.67	36.17	63.83
Model S2	13.16	86.84	14.81	85.19
Model C2	39.67	60.33	39.73	60.27
Model I2	46.18	53.82	52.36	47.64

4.2.2.2 Wall shear stress

Figure 4.8 shows the wall shear stress contours of the four cases at flow rate of 167 ml/s. In model U, the high wall shear stress region was found to be around the anterior nasal wall. Wall shear stress of the remaining nasal wall was relatively smaller. In model S1, high wall shear stress region was observed near the lateral walls of the nasal valve region which might be due to the twisting of the anterior airway. The wall shear stress along the left turbinate was apparently lower than the right turbinate as the airflow was quite small. In model C1, the high wall shear stress region was found to mainly distribute around the nasal valve. In model I1, the high wall shear stress region in the right nasal airway mainly located at the inferior passage, which might be due to the decreased anterior patency and the high airflow rate. While in the left airway, the wall shear stress magnitude was relatively low in the anterior region due to the low flow rate, but high around the middle turbinate due to the blockage of the airway. It was notable that in reopened models (models S2, C2 and I2), the patterns of wall shear stress distribution did not change much compared to original models (models S1, C1 and I1), except for local regions where collapsed airway has been reopened such as the superior region of nasal airway in all the three cases and the middle portion of left nasal airway in slanted case (denoted by arrows). The anterior lateral wall near the collapsed anterior roof was found to be generally accompanied with high wall shear stress magnitude in all the three models with deviated noses (indicated within black circle).

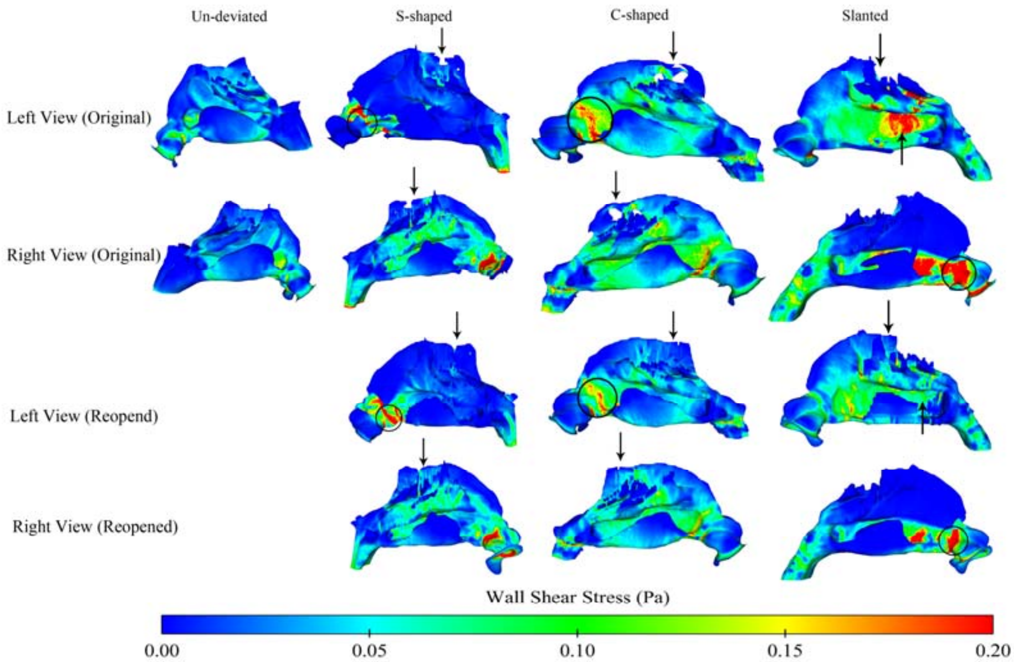

Figure 4.8 Left and right views of wall shear stress distribution along the nasal wall in the models at flow rate of 167 ml/s.

4.2.2.3 Flow resistance

Table 4.7 shows the nasal resistances in all the seven models. The resistances at flow rate of 500 ml/s were considerably larger than 167 ml/s. This is consistent with reported data where the nasal resistances increased with flow rates (Weinhold and Mlynski, 2004). The resistances in reopened deviated models (models S2, C2 and I2) were at least 1.4 times of model U for both the two flow rates. With internal blockage, the nasal resistances in original models (models C1, S1 and I1) were generally larger than reopened models, and were at least 1.7 times of the resistance of model U. With reopened internal cavity, the maximum flow resistance caused by deviation of external nose was found in model S2, followed by models I2 and C2.

Table 4.7 Flow resistances of the models at flow rates of 167 ml/s and 500 ml/s.

Flow Rate (ml/s)	Flow resistance of nasal cavity (Pa·s/ml)						
	Model U	Model S1	Model C1	Model I1	Model S2	Model C2	Model I2
167	0.019	0.048	0.039	0.056	0.040	0.031	0.034
500	0.035	0.119	0.062	0.140	0.094	0.052	0.070

4.2.2.4 Path-lines

Figure 4.9 shows the path-lines of left and right nasal airways in all the four cases at flow rate of 167 ml/s. In model U, middle and inferior portions were two main passages of airflow. This is consistent with reported study where around 10% airflow passes through the superior portion in healthy nasal cavity (Keyhani et al., 1997; Zhao et al., 2004). In model S1, high velocity magnitude appeared in the right anterior airway, and the airflow in left cavity was separated into two branches due to the collapse of the anterior inferior portion. Few path-lines reached the superior region. The path-lines in model C1 were comparable to model U, except that path-lines in the superior portion of posterior airway were disturbed due to the internal blockage. In model I1, the velocity magnitude of the left posterior region was larger than the anterior airflow due to the internal blockage. The right airflow mainly passed along the bottom of the airway. In reopened models (models S2, C2 and I2), the path-lines along the turbinates were generally more continuous compared to the original models (models S1, C1 and I1). Vortexes with considerable sizes were formed in the nasal airways with collapsed anterior nasal roof (as shown in the black circle). In addition, some of the flow patterns in original models due to crooked noses remained in reopened models, such as the two main branches in the left airway of model S2 and the main stream along the right nasal bottom of model I2.

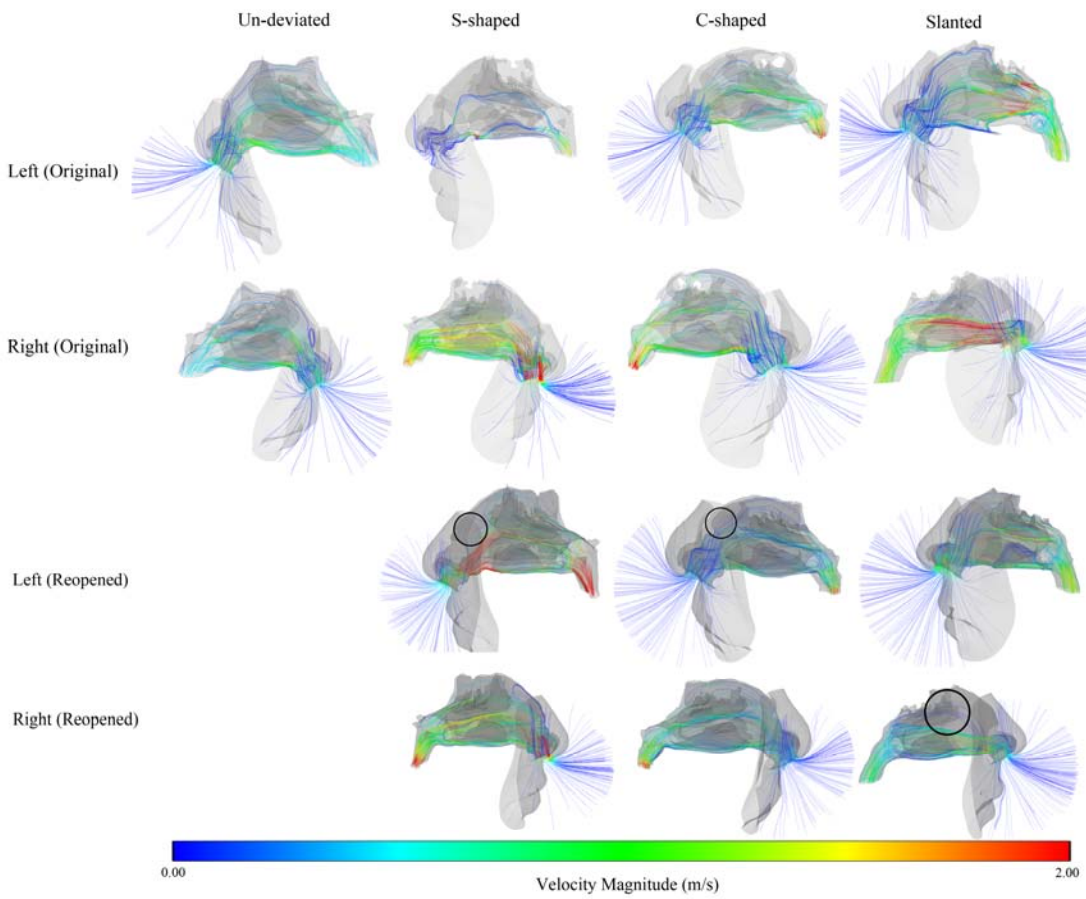

Figure 4.9 Path-lines of left and right airways of the models at flow rate of 167 ml/s.

4.2.3 Discussion

Restoration of nasal airflow has been less concerned during surgical intervention of deviated noses. By reconstructing 3D nasal models, we found that the deviation of the nose tended to collapse anterior nasal roof of one airway and leave the other airway relatively less affected in all the three cases with crooked nose. Also, the anterior airway would be more distorted compared to un-deviated nasal cavity.

The three types of deviation of external noses exhibit different manners of influences on nasal airflow patterns. With the middle and the inferior portions of external nose in S-shaped case deviated towards opposite directions, the anterior airways were twisted (Figure 4.6). The left airway was severely compromised. The MCA of the left airway decreased to the lowest among the four models. Without internal blockage, the S-shaped deviation (model S2) induced the largest nasal resistance among the three cases with deviated noses. In addition, the anterior airway twisting restricted the airflow through the left airway to a minimum of the three deviated cases. This might be quite serious as one of the cavities was nearly dysfunctional leading the other cavity to be overloaded during respiration. The anterior collapse of airway extended to the middle of the turbinates, which further increased the nasal resistance (model S1). In slanted case, the whole external nose deviated towards the left side that caused the MCA to be the second lowest. Regardless of the internal blockage, the slanted deviation induced second largest nasal resistance (model I2). Moreover, the severe internal blockage on the left side of turbinates in model I1 increased the nasal resistance to be the maximum of all the models. The collapse of anterior nasal roof constrained the air to flow along the nasal roof. With only the middle portion of external nose deviated, airflow through the C-shaped case was quite comparable to the un-deviated case in terms of airflow partitioning, path-lines and wall shear stress distribution. The larger flow resistance compared to un-deviated case might be due to the decreased MCA of the left airway. It is reasonable to observe such considerable diversities of flow patterns among the three types of external deviations, since even minor changes of anterior portions of nasal valve could significantly affect the whole course of the flow (Zhao et al., 2004). Garcia et al. (2010) also confirmed that the anterior septal deviation increased nasal resistance more than middle and posterior deviations.

The flow partitioning did not vary much with flow rates in un-deviated and the original and reopened S-shaped and C-shaped cases. However, considerable difference of flow partitioning at the two flow rates was found in both models I1 and I2. One of the possible reasons might be due to the flat right upper nasal wall which constrained the airflow along the nasal bottom inducing smaller increasing pace of nasal resistance against flow rate compared to left cavity. As the flow partitioning varies among individuals and flow rates, it is essential to extend the nasal cavity to external atmospheric region to naturally develop airflow into nostrils in order to accurately simulate nasal airflow. Moreover, the inflow boundary condition could affect nasal airflow properties as well (Taylor et al., 2010).

Vortexes could usually be found around the anterior nasal roof, which is associated with the angle between the upper wall of nasal vestibule and the anterior roof (Zhu et al., 2011). In this study, vortexes emerged around the collapsed anterior roof in all the three cases. However, the location of the vortex in nasal cavity with crooked nose was more posterior than healthy subjects in previous study which might be due to the different location and the different extent of abrupt change of anterior nasal morphology. The anterior distortion and collapse also affected the flow distribution in middle nasal airway, e.g. the airflow was constrained along the nasal bottom region in the right airway of slanted case, and two airflow branches were generated in the left airway of S-shaped case.

The airflow properties in C-shaped case, with relatively smaller compromise of anterior roof, were more symmetric in the left and right airways.

Compared to model U, the deviation of external nose induced asymmetric distribution of wall shear stress along the two nasal airways, especially in S-shaped and slanted cases. This is reasonable since the wall shear stress is proportional to the near-wall velocity gradient which is affected by deviation of anterior morphology. The collapsed region of anterior nasal roof induced high wall shear stress in this region in all the three cases with deviated nose. It appeared that the collapse of anterior airway influenced the downstream middle and posterior airflow patterns, while the internal blockage along the turbinates further disturbed the flow properties.

Based upon 260 patients with external nasal deviations, Foda (2005) reported that 75% of them had various degrees of nasal obstructions. Consistently, our findings show at least 40% increase of nasal resistance in reopened models with external deviated noses compared to un-deviated case. The nasal obstruction or increased nasal resistance in deviated noses might be due to the distortion and collapse of anterior airway. Despite the external deviation, the interaction between internal blockage and deviation of external nose could considerably change the flow partitioning, increase wall shear stress around the blocked area and increase nasal resistance.

In the past, techniques for correcting crooked nose were mainly concentrated on straightening and symmetrising the external noses with less focus on the restoration of nasal airflow (Hoffmann, 1999; Okur et al., 2004; Pontius and Leach, 2004; Porter and Toriumi, 2002; Rohrich et al., 2002; Zoumalan et al., 2009). In particular, breathing in

20% of the patients with preoperative nasal obstruction was not fully restored after correction of crooked nose (Foda, 2005). Based upon the current three CFD cases with crooked nose, we suggest that there are possibly two situations that need to be taken care of during surgical intervention. Firstly, the anterior airways of all the S-shaped, C-shaped and slanted cases are distorted and collapsed which would certainly increase nasal resistance, especially the one with minimal MCA. Secondly, the collapse of the internal airway disturbs the flow properties and causes the nasal obstruction to be more severe.

4.3 Summary

This chapter investigated two case studies of nasal airflow in deformed nasal airways. In the first study, airflows in nasal cavity with orbito-maxillary bone fracture before and after surgical intervention were compared with each other. The bone fracture collapsed the superior and the left middle portions of the airway. The ORIF surgical intervention significantly restored the collapsed left nasal airway induced by left orbito-maxillary fracture with decreased nasal resistance, more even flow partitioning and more continuous streamlines. However, local discontinuity of air space still existed in post-operative nasal cavity that disturbed the airflow distribution especially around the superior region.

In the second study, airflows in three nasal cavities with typical deviated noses (one S-shaped, one C-shaped and one slanted) have been examined. Based upon the current models, we found that one anterior nasal roof in each of the deviated cases was collapsed, leaving the patency of the other anterior nasal roof less affected. The internal airways along the turbinates were partially collapsed in all the three cases with crooked noses.

The collapse of anterior nasal roof produced vortexes around the collapsed region of anterior roof. It also induced high wall shear stress near the collapsed region. Compared to un-deviated nose, the deviation of external nose caused higher nasal resistance. For example, increase of at least 40% resistance in all the crooked noses was found. On the other hand, the blockage of the airway along turbinates increased the nasal resistance further and disturbed the airflow properties such as wall shear stress and streamlines.

As indicated in chapter 3, the human nasal cavity has been adapted to the environment to optimize breathing activities and upper airway functions. Any deformation of the original geometry of the nasal airway would change the respiratory airflow patterns and may affect the efficiency of nasal functions. For example, in both of the current two cases, the deformation of nasal airway induced discontinuous streamlines, higher nasal resistance and uneven distribution of airflow through the airway. Surgical intervention can be performed to correct deformed nasal morphology and restore abnormal nasal airflow patterns. However, it is still difficult to determine how successful the operation is merely based upon self report from the patient without any quantitative analysis. The current chapter shows that CFD simulation is an efficient tool for such analysis. In addition, CFD simulation could also play as a pre-diagnosis tool to identify the most urgent airflow-related problem that need to be treated during the surgical intervention, such as correction of deviated external nose.

Chapter 5 Air Ventilation through Human Maxillary Sinuses

Despite the nasal airflow, locating beside the middle meatus, the airflow ventilation through human maxillary sinuses is also vital. On the one hand, the maxillary sinuses are susceptible to infection since excess mucus cannot be easily drained out of them by gravity. The resulted sinusitis is a painful and often chronic condition that affects approximately 15% of the United Kingdom population (Hood et al., 2009; Kaliner et al., 1997). On the other hand, since natural ostium, usually as the only conduit for mass exchange between maxillary sinus and nasal airway, is shielded from direct access of physical investigations by the uncinate process, turbinates and ethmoid cells, physical measurements of maxillary sinus ventilation are difficult without sinus puncture. To study the maxillary sinus ventilation is therefore urgent but complex. Moreover, additional ostia, namely, accessory ostia (AO) can exist as other links between maxillary sinuses and nasal airway. The prevalence of AO was estimated to be between 4 and 50 percent (Jog and McGarry, 2003). The existence of AO was associated with mucus circulation between AO and NO (Chung et al., 1999), which was thought to be one of the main causes of persistent rhinosinusitis and chronic maxillary sinusitis (Kaliner et al., 1997). Xiong et al. (2008), constructed a 3D model of a normal nasal cavity and paranasal sinuses, and showed very little air exchange between the paranasal sinuses and nasal cavity during stable airflow. Hood et al. (2009) built simplified 3D CFD models with/without AO by characterizing the sinus as a large truncated cone joining to a rectangular channel to evaluate maxillary sinus gas exchange. They found that the presence of an AO could increase the sinus ventilation rate by several orders of magnitude. Their findings were confirmed by experiments with a replica of this simplified model (Rennie et al., 2011). However, since any minor change of nasal geometry (Garcia et al., 2010; Zhao et al., 2004) or differences of boundary conditions (Taylor et al., 2010) in these prior studies could significantly influence their output of numerical simulation of nasal airflow and sinus ventilation, a high resolution, life-like 3D nasal cavity and maxillary sinus model, with and without AO, is preferred to accurately assess the sinus ventilation through NO and effects of AO on sinus ventilation.

In the present chapter, we evaluated, by CFD simulations, sinus ventilation through NO in the absence of AO, and effects of AO on maxillary sinus ventilation. A 3D nasal model was constructed from CT scans of a female adult with two left maxillary AOs (sinus I) and one right AO (sinus II), then compared to an identical control model with all AOs sealed (sinuses III and IV). Transient simulations corresponding to both respiratory airflow rate of 15 L/min and nasal blow at 48 L/min were carried out using these two models. Flow rates through all the ostia, streamlines through the sinuses, velocity contours of both the nasal airways and the sinuses have been evaluated and compared among the four sinuses.

5.1 Materials and methods

CT images of the sinuses and nasal cavity of a 43 year old female non-smoker with mild chronic allergic rhinitis, recurrent sinusitis, and no nasal surgery, were used for model construction. She had one maxillary AO on the right and two on the left (Figure 5.1). Model construction and discretization was performed as mentioned in sections 2.1 and 2.2 of chapter 2, using MIMICS and HYPERMESH.

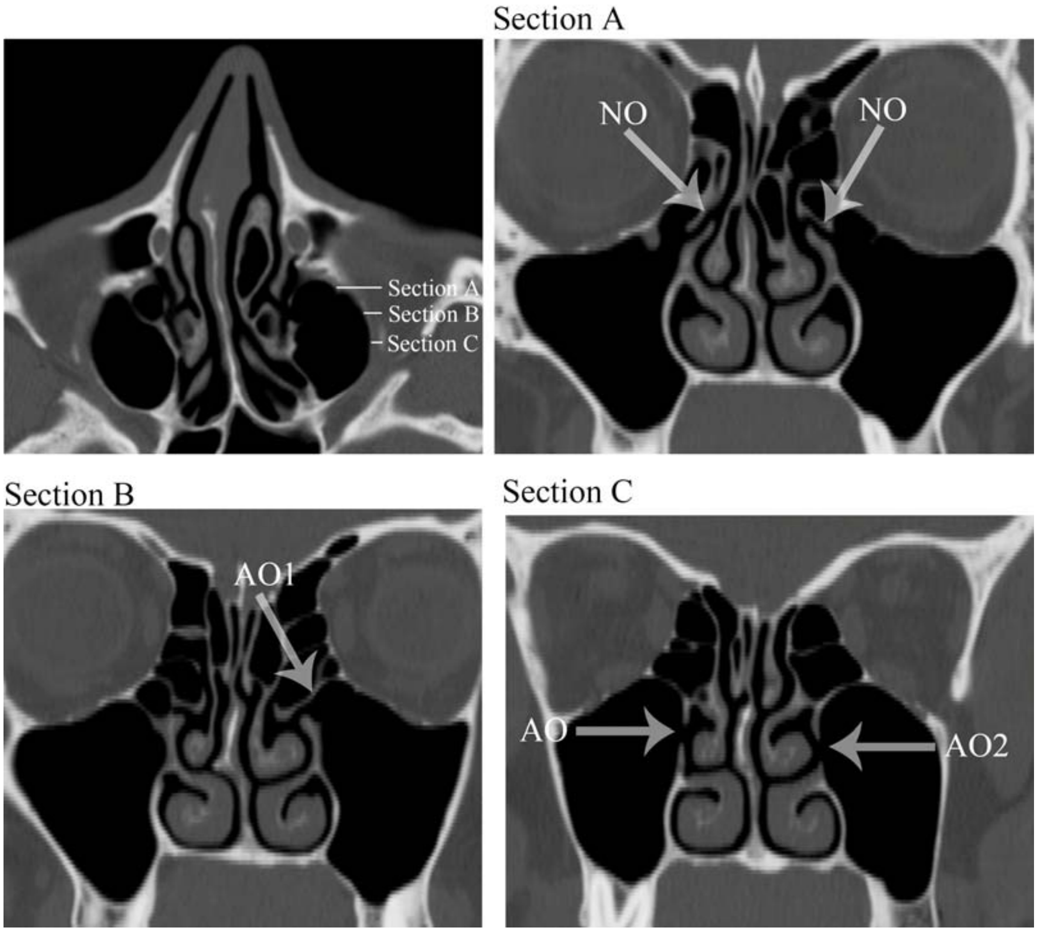

Figure 5.1 Axial and selected coronal CT sections showing ostia. NO, natural ostium; AO, accessory ostium; AO1, first left accessory ostium; AO2, second left accessory ostium.

Figure 5.2(A) shows the 3D model. A hemisphere with radius of 45 mm was integrated around the face for prescription of zero gauge pressure on the external surfaces. Velocity magnitude was applied at the internal, hypopharyngeal boundary. Figure 5.2B shows the superior-inferior view of the left (sinus I) and right (sinus II) sinuses, and enlarged medial views of the openings of the five ostia. On the left sinus, the first AO (AO1) is located very close to the NO, and the second AO (AO2) is far posterior. On the right sinus, the

NO and AO are also far apart. Control models with all AOs sealed off, were created for comparison (Figure 5.2C), in which sinus III is the same as sinus I, but with AO1 and AO2 sealed off, and sinus IV is the same as sinus II, but with AO sealed off.

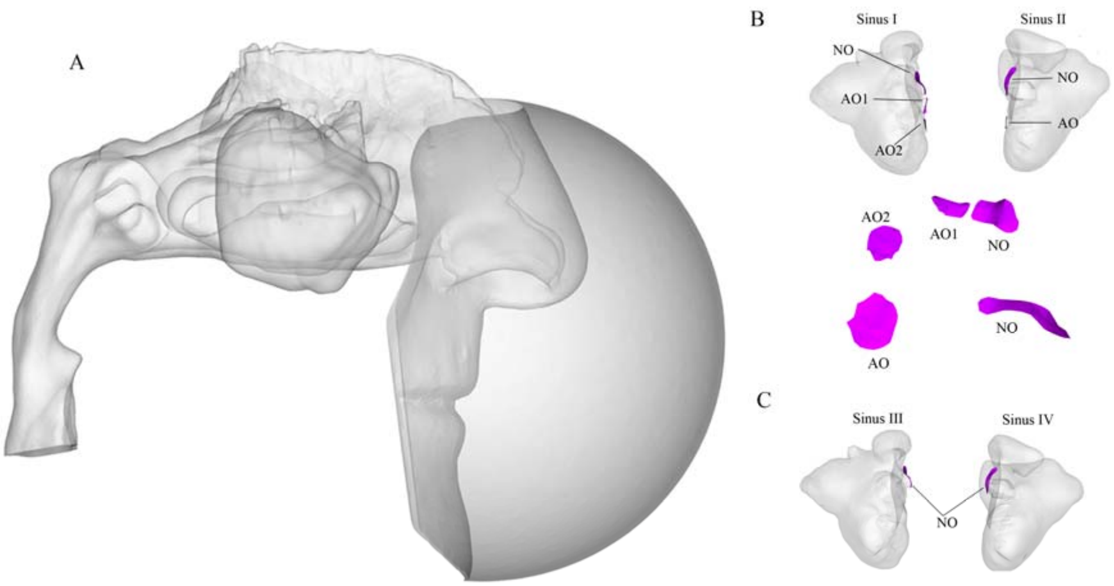

Figure 5.2 3D constructed model. A, Lateral view of sinus II. Superior-inferior views: B, sinuses I and II. C, sinuses III and IV.

Since the air ventilation of maxillary sinuses might be sensitive to unsteadiness of nasal airflow during respiration, simulations of transient airflow were carried out. As shown in Figure 5.3, the inspirational and expiratory phases during breathing are usually different regarding both the magnitude of airflow rate and the period. Benchetrit et al. (1989) reported that normal breathing cycles are similar within the same individual, while the difference of breathing cycles among individuals could be significant. Therefore it is hard to find one single standard breathing cycle representing for all the human breathing activities. To simplify, a sinusoidal variation of flow rate corresponding to ventilation rates of 15 L/min was applied at the hypopharynx representing for human breathing cycle (Figure 5.4). The numerical results based upon this simplification would surely be different from the real airflow patterns during breathing. However, we believe that the current sinusoidal signal should be able to predict the overall trend of nasal and sinus ventilations during inspiration and expiration. Two cycles of respiration, with duration of 4 seconds for each cycle, were simulated, and the second cycle was evaluated. In addition, a high flow rate nasal blow was simulated, by applying a 400 ml air volume within 0.5 second. Since our transient respiration simulations would experience the full transition from laminar to turbulent regimes, it is necessary to select a proper fluid model to handle this range. The Wilcox (Wilcox, 1998) LRN turbulent model which has been reported to be fully capable of reproducing the behavior of laminar, transitional, and turbulent flows (Zhang and Clement, 2003) was chosen. Equations 2.6, 2.7, 2.20 and 2.21 were solved by ANSYS FLUENT during the simulation.

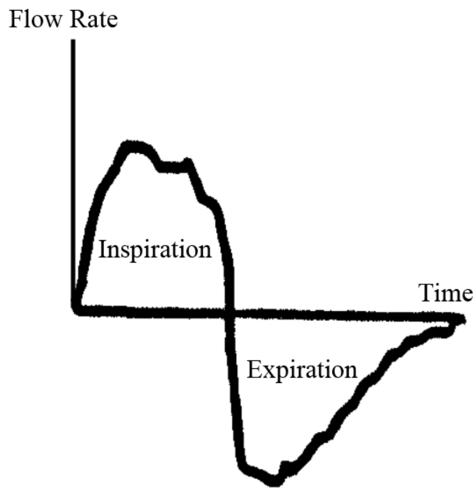

Figure 5.3 A breathing cycle of a healthy adult subject (Benchetrit et al., 1989).

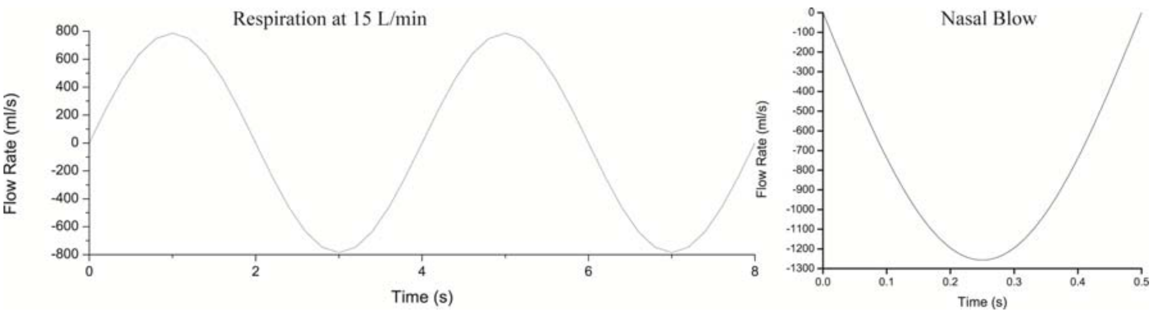

Figure 5.4 Transient velocity load.

5.2 Results

5.2.1 Airflow through ostia

Figure 5.5 presents the direction and flow rates through each ostium during simulated respiration. Since the net flow rates through ostia of sinuses III and IV are zero due to the incompressible assumption, the absolute flow rate passing through the ostium was calculated with the following equation:

$$Q_A = \frac{\int_A \left|\vec{u} \bullet \vec{n}\right| dA}{2} \tag{5.1}$$

where Q_A is the rate of flow entering the ostium, $\vec{u}$ is the velocity vector of the airflow, $\vec{n}$ is the normal vector of the maxillary ostium cross section, and A is the cross section of AO. The net flow rates in sinuses I and II were calculated as

$$Q_A = \int_A \vec{u} \bullet \vec{n} dA \tag{5.2}$$

In sinus I at 15 L/min (Figure 5.5A), airflows through NO and AO2 were in opposite directions and equal in magnitude. Flow rates through both NO and AO2 increased to a maximum within the first 0.4 second, and remained elevated throughout the whole inspiration until the last 0.4 second. The inspirational flow rate through AO1 was almost zero. Compared to inspiration, during expiration, flow directions through NO and AO2 reversed, and flow through AO1 became significant. Flow rates through all the three ostia had the same pattern seen during inspiration: rapid early increase, peaking in the middle, and decrease during the second half. Unlike inspiration, where AO1 had no flow, during expiration, flow through NO was opposite in direction, and equal in magnitude to, the summation of flows through AO1 and AO2. In both phases, flow through AO1 was less than through the other two ostia.

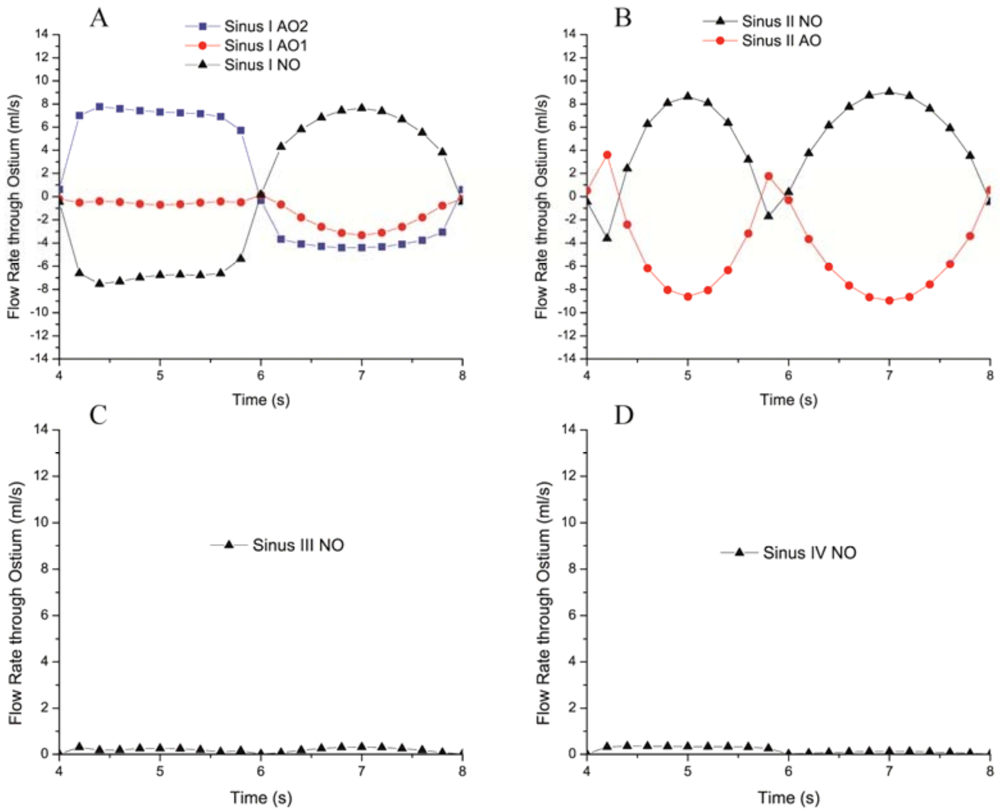

Figure 5.5 Flow rate through the ostia during respiration at 15 L/min.

In sinus II at 15 L/min (Figure 5.4B), the airflow pattern during both inspiration and expiration was very similar to that of AO2 and NO in sinus I. The only difference from sinus I was that the direction of flow through the NO was opposite in the two sinuses during inspiration, and that sinus II had two short periods of low magnitude flow reversal, in both NO and AO, at the beginning of both inspiration and expiration, a feature not seen in sinus I. In sinuses III and IV, with no AO, at 15 L/min (Figure 5.5C and D), flow rates through the NO were markedly lower, more than one order of magnitude less than in sinuses I and II.

The effect of modeling high nasal flow rates is shown in Figure 5.6. The variation of flow rate with time in sinus I during nasal blow was very different from the same sinus at 15 L/min. The flow rate through NO rapidly increased to nearly the maximum at the very beginning, while the flow in AO1 showed a short period of low magnitude flow reversal, similar to that seen in sinus II. Flow in AO1 initially held steady, then increased until the midpoint of the blow, and finally declined, while flow in AO2 increased at the very beginning, and decreased thereafter. Combined flows through AO1 and AO2 equaled the flow through NO. Most of the time, the flow rate through AO1 was proportional to the gross flow rate through the nasal cavity. Unlike sinus I during nasal blow, both the variation of flow rate with time, and the magnitude of the flow rate, for both the AO (sinus II) and the NO (sinuses II, III and IV) were comparable to the responses of the same sinuses during expiration at 15 L/min. At peak load during nasal blow, the maximum flow rate through sinus I was 0.43 L/min compared to 0.46 L/min at 15 L/min, while the maximum flow rates through sinuses II, III and IV during nasal blow were 0.74, 0.030 and 0.011 L/min, compared with 0.54, 0.019 and 0.0073 L/min at 15 L/min.

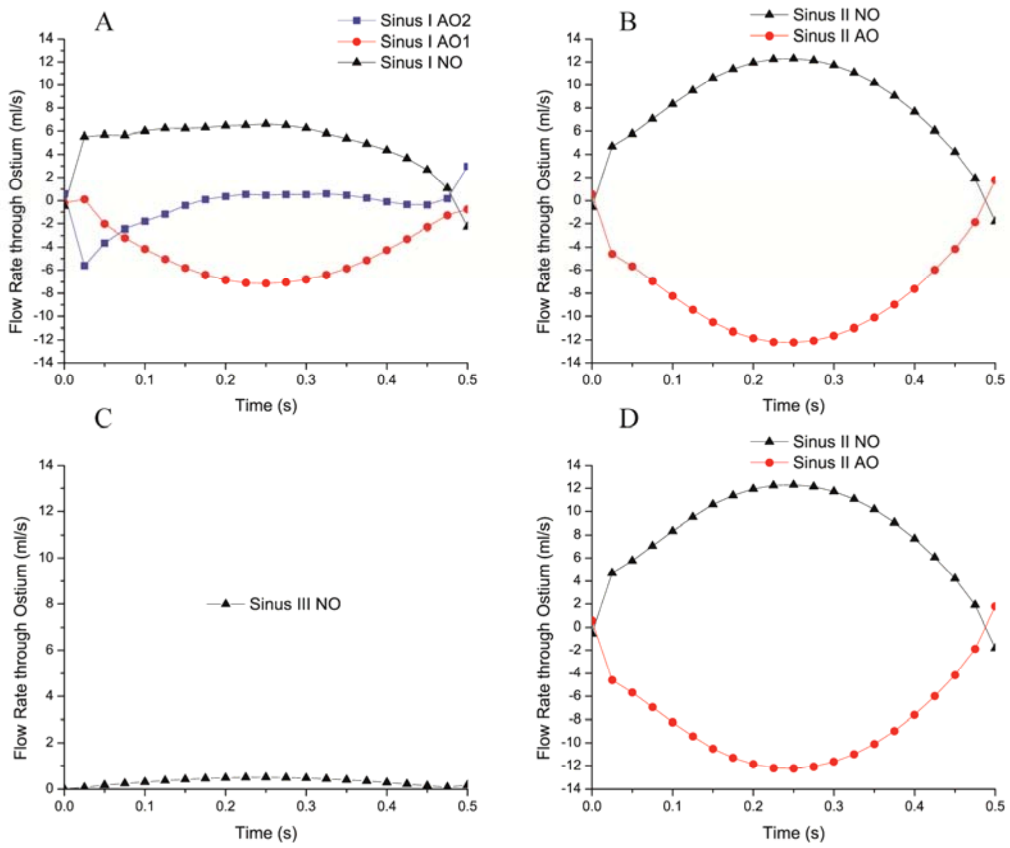

Figure 5.6 Flow rate through the ostia during nasal blow.

5.2.2 Streamlines through sinuses

Figure 5.7 shows airflow streamlines passing through the ostia into the maxillary sinuses at 15 L/min during peak inspiration and peak expiration. In sinus I, air entered NO and exited through AO2 during inspiration. No streamline was found passing through AO1 due to the low flow through AO1. During expiration, sinus airflow reversed, by entering both AO1 and AO2, and exiting through NO. In sinus II, air entered AO and exited through NO during both inspiration and expiration. Moreover, in both sinuses I and II, the streamlines through AOs were relatively parallel to the cross-sections of AOs at both peak inspiration and peak expiration. The streamlines through NOs, however, were almost perpendicular to the cross-sections of NOs. The streamline contours in sinuses III & IV were not presented here since it was not possible to generate continuous streamlines in these sinuses using the current models due to very low flow rate (models with much finer mesh is required).

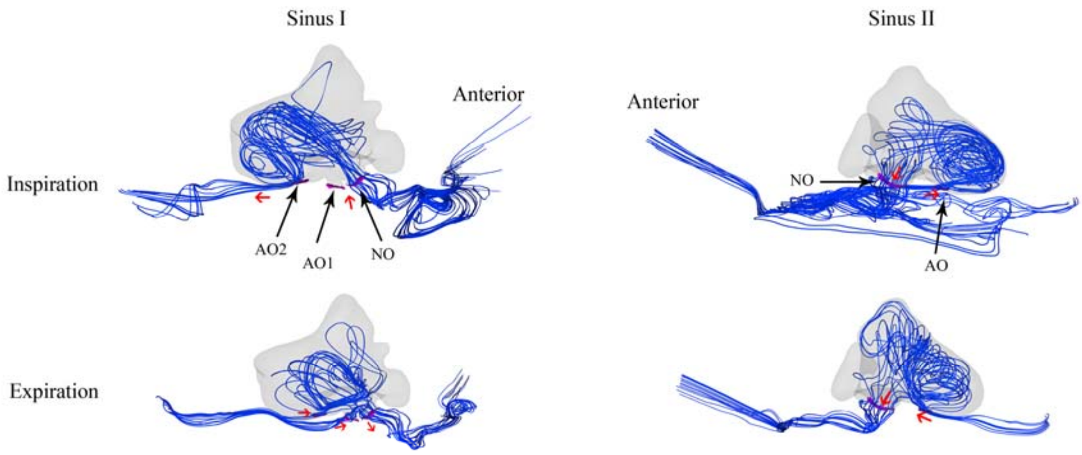

Figure 5.7 Superior-inferior view of ostial streamlines at peak inspiratory and expiratory flows. Red arrows show airflow direction. Projections of ostial cross sections shown in black.

5.2.3 Nasal airway velocity contours

Figure 5.8 shows velocity contours, at 15 L/min, of nasal airway cross-sections at NO (section A), AO1 (section B) and AO2 (section C) of sinus I, at the peak loads of inspiration and expiration. The air mainly passed through the middle and inferior portions of the nose, and especially around the middle turbinates, which is consistent with prior results (Lee et al., 2010). In addition, airflow was more uniform during expiration than inspiration, while the velocity was greater during inspiration. Air velocity within the sinuses was minimal compared to nasal flows.

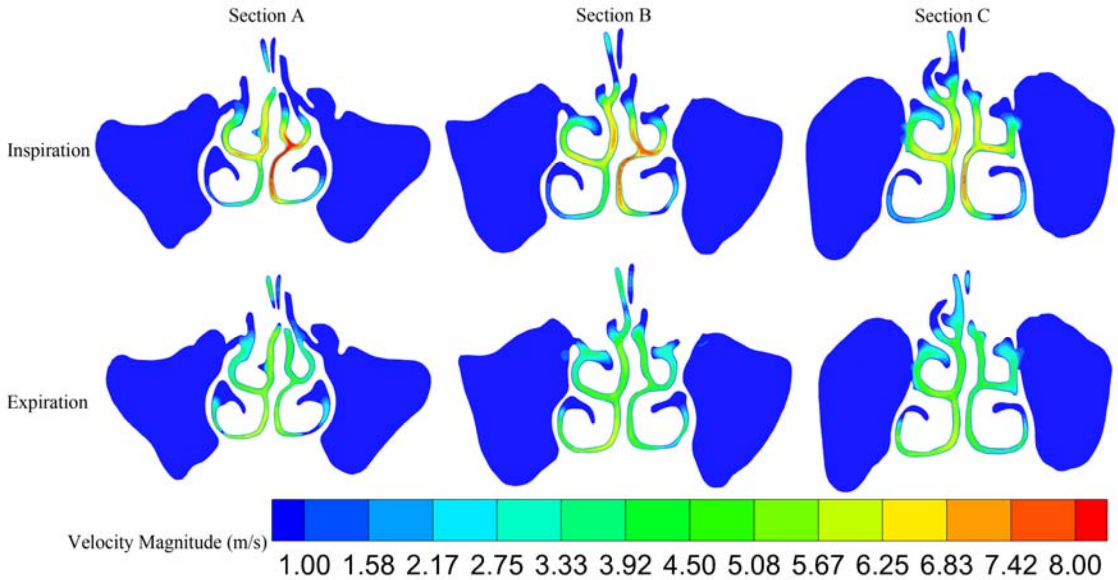

Figure 5.8 Velocity contours of the nasal cavity at sinus ostia. A, around NO of sinus I; B, around AO1 of sinus I; C, around AO2 of sinus I.

5.2.4 Sinus velocity contours

Figure 5.9 shows velocity contours of sagittal cross-sections near the ostia (section 1) and at interior of the sinuses (section 2) at peak inspiration and peak expiration. The velocity magnitudes around AO2 of sinus I, and AO of sinus II were significantly larger than around NOs at both peak inspiration and peak expiration. During inspiration, the velocity magnitude around AO1 of sinus I was quite minimal compared to AO2 and NO. Within sinus I, relatively high velocity was observed in the region between AO2 and NO (section 2). In sinus II, a jet-like flow pattern towards the posterior of sinus II was formed around AO in section 1. This jet-like flow is possibly generated by the shear force of the airflow nearby. Within sinus II, the jet-like flow moved further towards the posterior wall and rebounded in section 2. During expiration, the velocity magnitude through AO1 of sinus I significantly increased as shown in section 1. In the interior, relatively high velocity magnitude was found around NO (section 2). This is because the two flow branches from AO1 and AO2 merged together towards NO during expiration (as shown in Figure 5.7). While in sinus II, there was no jet-like flow pattern during expiration. High velocity magnitude was observed in the region between AO and NO. In comparison, airflow of the whole Sinus III (in the absence of any AO) (Figure 5.9C) is barely detectable.

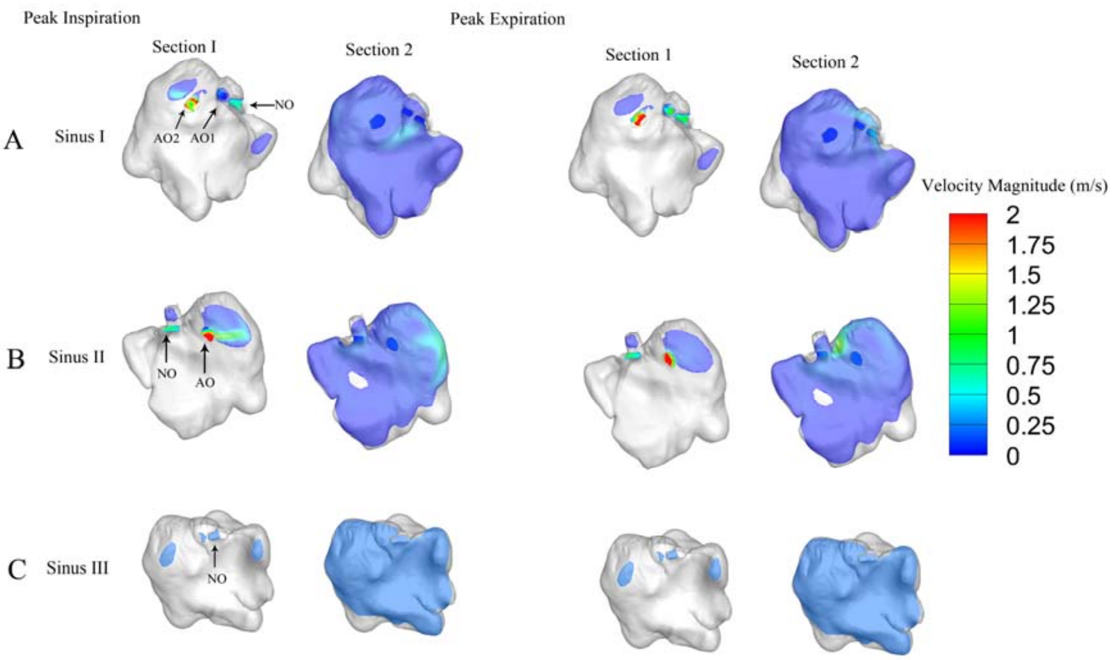

Figure 5.9 Velocity magnitude contour of sagittal cross sections around the ostia (section 1) and within the sinus (section 2) of sinuses at peak inspiration and peak expiration. A, sinus I. B, sinus II. C, sinus III.

5.2.5 Average ostia pressure

Figure 5.10 shows the average pressure of CSAs of the ostia at peak inspiration/expiration in sinuses I and II. In sinus I, during inspiration, since the NO was located upstream of AO1 and AO2, the pressure gradually decreased in the streamwise direction. During expiration, the sinus airflow direction changed with global nasal airflow where the airflow entered AO1 and AO2, and exited through NO, therefore it was reasonable to observe that the average pressure upstream (at AO2 and AO1) was larger than downstream (NO). In sinus II, since the airflow always entered AO and exited through NO, the average pressure was larger around AO than NO at both peak inspiration and expiration. In addition, due to the low velocity magnitude around sinuses, the pressure differences between upstream and downstream ostia were quite small (less than 1.9 Pa) compared to the pressure gradient along the nasal airway.

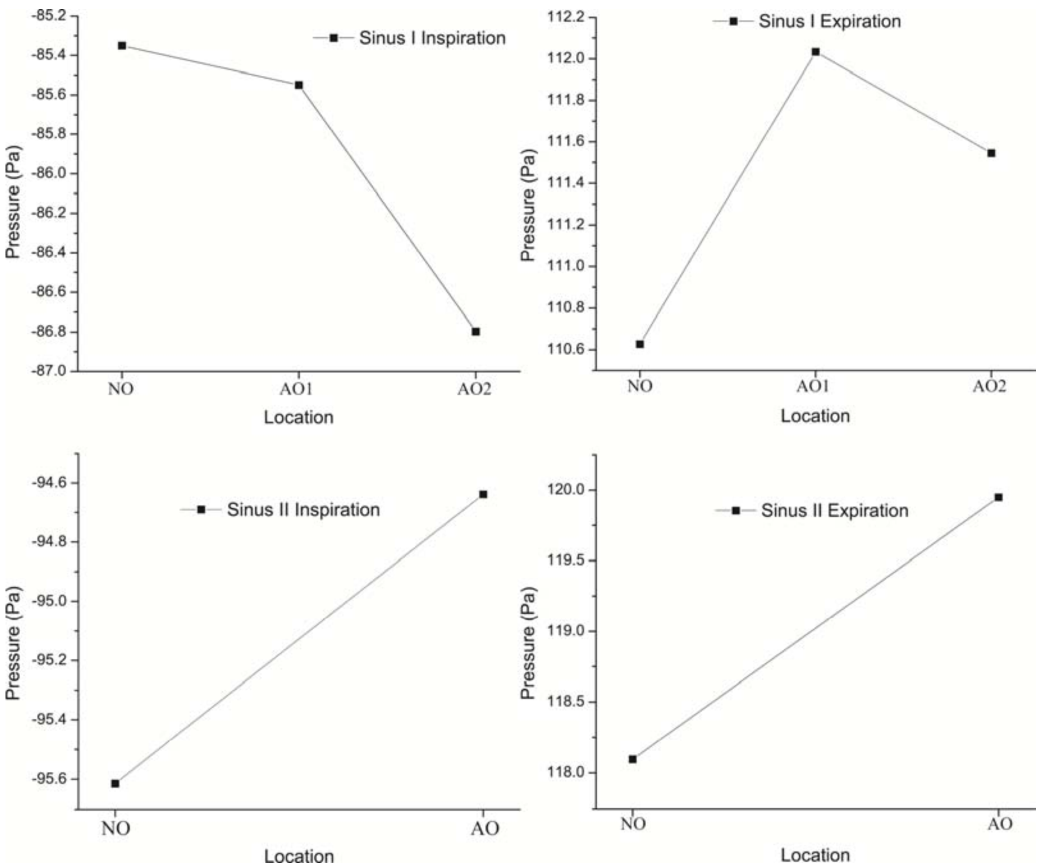

Figure 5.10 Average pressure of cross sectional area around sinus ostia at peak inspiration and peak expiration.

5.3 Discussion

This simulation included analysis of both nasal and sinus airflow. In the nasal cavity, there was a noticeable difference, in both air velocity and airflow distribution, between inspiration and expiration: during expiration, flows were slower, distributed more evenly, and contacted more airway surfaces (i.e., far into the inferior meatus). This finding indicates that the anterior-posterior 3D nasal shape is significantly asymmetric, resulting in these observed differences. Since water is regained from the saturated and warmed expired air on the mucosa for conditioning of the air during the following inspiration (Pless et al., 2004), from an anthropologic perspective, improved contact of the airstream with the nasal surface during expiration could be interpreted as an adaptation for reducing respiratory water and heat loss. Compared to expiration, the efficiency of air conditioning during inspiration might be lower due to less contact between the airstream and the mucosal surface. However, further *in vivo* investigation is needed to verify this observation.

The most striking effect of having one or more maxillary sinus AOs is a very large increase in ventilation through the sinus, compared with sinuses having only the NO. The absence of any AO almost completely prevented air from passing through the maxillary sinus. There are several reasons for the significant increase of air ventilation through a sinus with AO compared to sinus without AO. Firstly, the length of AO is much shorter than the length of NO, and therefore it is easier for air to penetrate into the sinus through the AO. Otherwise, in the absence of AO, the uncinate and ethmoid cells surrounding the NO act as a shield to prevent airflow in the nasal cavity from closely approaching the NO. Secondly, since the AO is usually connected more inferiorly in the middle meatus than the NO, the velocity magnitude around the AO is much higher than around the NO (Figure 5.9A and B). Thirdly, the pressure difference between NO and AO drives the air to flow through sinus. The mechanism of air ventilation through a sinus with AO is complex. Other than the pressure difference among the ostia, the shear force also plays an important role in driving the air into sinus. Evidence for shear driven flow includes the fact that vortexes appear near AOs (Shankar and Deshpande, 2000). In addition, our observed streamlines were parallel to the cross-sections of AOs, while perpendicular to the cross-sections of NOs (Figure 5.7). This effect was also clearly observed in an idealized model of Hood et al. (2009).

Existence of more than two ostia is not necessarily associated with further increased flow, since the flow through sinus I (with two AOs) was comparable to flow through sinus II (with one AO). The increased ventilation of sinuses with AOs is complex. Under high flow conditions mimicking nose blowing, in sinuses II, III, and IV, the airflow rate in the sinuses increased, compared to the same sinuses at 15 L/min. Uniquely, the maximum sinus flow rates remained the same in sinus I, with three ostia, under both high and low nasal flow conditions. Our simulations also show small transient airflow reversals at both the beginning and end of respiratory phases, during high airflow conditions in sinus I, and at both high and low flow conditions in sinus II. This finding could be caused by inertia of local airflow. Under low nasal flow conditions, in both sinuses I and II, airflow through the NO and through the combined AOs, was equal in magnitude and opposite in direction. The sinuses differed in the direction of airflow with respiratory phase. Sinus I (two AOs) exhibited flow reversal, with the flow through the NO moving in the same direction as the gross nasal flow for both inspiration and expiration; while sinus II (one AO) showed the opposite, with airflow through the AO always moving into the sinus, despite the change of nasal airflow direction. The reason for that the flow direction in sinus II was different from the gross nasal flow during inspiration could be due to the pressure difference between the two ostia and the shear force of the nasal flow passing by the AO. As shown in Figure 5.7 and Figure 5.9B, the velocity of the nasal airflow was so high that the air within sinus was forced to flow towards the posterior sinus wall and rebounded to exit through the NO. The airflow in sinus II always entered AO and exited through NO. Similar patterns of mucus flow were observed in recurrent sinusitis patients, where mucus entered AO and exited through NO (Matthews and Burke, 1997). Also, mucus transport speed was reported to be proportional to sinus airflow rate (Kim et al., 1986). With only two examples, it is not possible to extrapolate to all multi-ostial sinuses, but the present study has indicated that the presence of more than one ostium can radically change sinus ventilation, and this could affect, in some adverse manner, sinus function, mucus drainage, and susceptibility to disease. Considering the reported significant prevalence of AO, there will need to be systematic investigation of the influences of AO on sinus pathologies.

The physiology and pathologies of maxillary sinuses are not yet well understood. Air ventilation of a maxillary sinus can influence the sinus in several ways. Firstly, since nitric oxide within the paranasal sinuses provides an antibacterial environment and modulates mucociliary clearance function (Deja et al., 2003), the gas exchange between sinus and nasal airway may influence the concentration of nitric oxide in sinus. Secondly, air ventilation also determines sinus particle deposition patterns, such as deposition of bacteria and drugs on sinus wall (Möller et al., 2010). Thirdly, the airflow influences mucus clearance (Kim et al., 1986). Compared to sinuses without AO, the considerably larger airflow rate in sinuses I and II will therefore affect nitric oxide concentration, vulnerability to bacteria and drug delivery efficiency, and also influence the mucus clearance process. However, *in vivo* and functional studies are needed in order to confirm these CFD findings, and evaluate the actual impact of AO on sinus physiology and pathophysiology.

5.4 Summary

Although sinus is a rather complex region for physical examination, CFD simulations provide an easy and efficient way for the investigation of sinus ventilation. In the absence of AO, the sinus ventilation through NO was found to be limited to a particularly low level due to the long length of NO, the relatively low velocity magnitude around the binding site between NO and the superior of middle meatus, and the curvature of the airway around NO. The existence of both one and two AOs, compared to a single NO, increased the ventilation rate through maxillary sinuses by more than an order of magnitude. The flow rate through a sinus with two AOs is comparable to a sinus with one AO, however, the presence of two AOs complicates the flow partitioning of the gross maxillary sinus ventilation among the ostia. Accessory ostia also may affect the direction of flow through the NO. Whether these alterations have an impact on physiology or pathophysiology of the sinuses remains unknown, and needs to be investigated by future human studies.

Chapter 6 Interaction between Pharyngeal Airflow and Movement of Human Soft Palate

In chapters 3, 4 and 5 we studied respiratory airflow in human nasal cavity and maxillary sinus. Recently, the airflow patterns in human pharyngeal also have drawn much attention due to the complicated mechanisms of fluid-structure interaction (FSI) between pharyngeal airflow and surrounded soft tissues. Particularly, the obstructive sleep apnea hypopnea syndrome (OSAHS), as a troublesome disease resulted from the interaction, affects 2% adult women and 4% adult men (Young et al., 1993). The OSAHS is characterized by recurrent episodes of upper airway collapse during sleep, and involves cessation or significant decrease in airflow in the presence of breathing effort (Guilleminault et al., 1976). The OSAHS can produce excessive daytime sleepiness, chocking or gasping during sleep, daytime fatigue and impaired concentration (Randerath et al., 2006).

The causes of collapse of upper airway are still not fully understood. One possibility is that, the sub-atmospheric air pressure during inspiration produces inward force on the surrounded wall of the pharynx to collapse the airway; while the above atmospheric air pressure during expiration produces outward force on the surrounded wall to dilate the airway. This explanation has been proven by evaluating CSAs along the pharynx during respiration (Schwab et al., 1993; Schwab et al., 1996; Schwartz et al., 1988). On the contrary, researchers also observed that the upper airway collapse appears during expiration (Caballero et al., 1998; Morrell et al., 1998; Yucel et al., 2005). A more in-depth investigation on pharyngeal airflow/soft tissue interaction is therefore needed.

In the current chapter, we examined the airflow/soft tissue interaction in human pharynx. The retropalatal region of the oropharynx, as the most common site of collapse, was chosen for investigation (Dempsey et al., 2010). Particularly, the interaction between retropalatal airflow and human soft palate was evaluated using FSI simulation.

6.1 Materials and methods

6.1.1 Model reconstruction and discretization

MRI images of a 35 years old healthy Chinese male were obtained for model reconstruction. The subject was 183 cm tall with a body mass index of 23.9. He did not have any nasal symptoms and did not take any medications upon MRI examination. The subject was under supine condition and was asked to hold the breath during MRI process. As shown in Figure 6.1(a), the soft palate in the green lies behind the human tongue. The air space of pharynx is enclosed by the posterior surface of human tongue and the pharyngeal wall. The anterior side of the soft palate is attached to the hard palate (shown as red line).

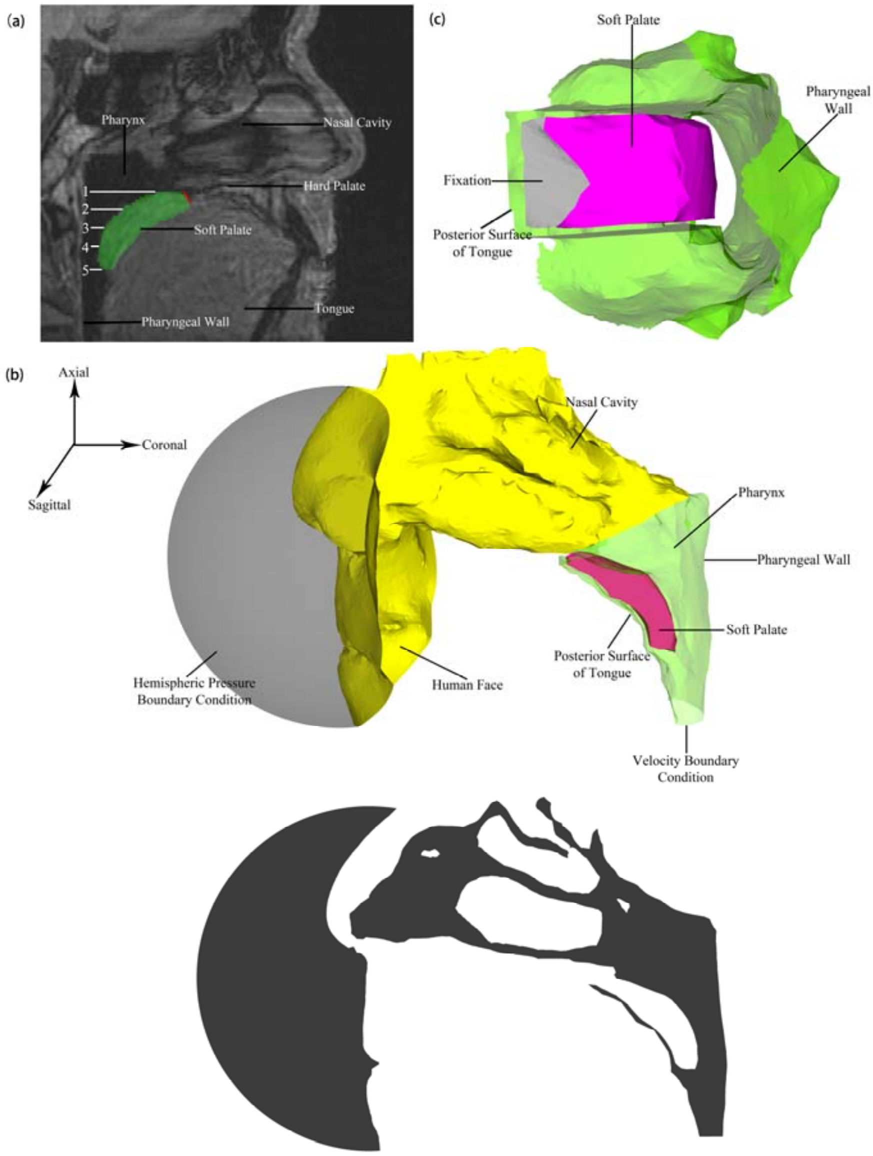

Figure 6.1 (a) Sagittal image of human upper airway. The fluid domain consists of the nasal cavity, the nasopharynx and the oropharynx. The interface between soft palate and hard palate was fixed (shown as red line). CSAs of 1 to 5 in retropalatal airway were defined along the palate. (b) Fluid model. The lower image shows the sagittal cross section of the fluid domain where the soft palate is totally immersed within the airway except for the interface between soft palate and hard palate. (c) Structural model. Contact condition was prescribed between the soft palate and surrounded walls (posterior surface of tongue and pharyngeal wall).

MIMICS and HYPERMESH were used for model reconstruction and discretization as described in sections 2.1 and 2.2. As shown in Figure 6.1(b), the computational fluid domain consists of the nasal cavity, nasopharynx and oropharynx. Depicted in the sagittal cross section of the fluid domain, the soft palate is immersed within the airway except for the interface between the soft palate and hard palate. The interface between the soft palate and hard palate was assumed to be fixed (Figure 6.1(c)).

6.1.2 Mathematical modeling of the human soft palate

Successful structural simulation requires accurate mathematical description of material property. However, measurement of in vivo human soft tissue properties remains a challenge. Recently, Birch and Srodon (2009) reported a mean elastic modulus of 585 Pa at the posterior free edge and 1409 Pa at regions of attachment of the soft palate with viscoelastic behavior by ex vivo measurements of human soft palate. Without residual muscle tension, the ex vivo elastic modulus could be different from in vivo elastic modulus. Cheng et al. (2011), by measuring in vivo viscoelastic property of soft palate, reported a shear modulus of 2530 Pa under 80Hz oscillatory loading. As a preliminary study, we simplified the property of human soft palate as linear elastic, isotropic and homogeneous with Poisson ratio of 0.49 and Young's modulus calculated as:

$$E = 2G(1+\nu) \tag{6.1}$$

where E is the Young's modulus (7539 Pa), G is the measured in vivo viscoelastic shear modulus reported by Cheng et al. (2011) and ν is the poison ratio. FSI model with a much lower Young's modulus (3000 Pa) was also simulated to evaluate how the motion of soft palate varies with Young's modulus. CFD simulation of the fluid domain was carried out for comparison. Equations 2.25, 2.26 and 2.27 were solved to predict the displacement of human soft palate.

In the structure domain, a contact condition, defined as

$$g \geq 0; \lambda \geq 0; g\lambda = 0 \tag{6.2}$$

where g is the gap function between two points of the contact surfaces and λ is the normal contact force function on the contact surfaces, was applied between the FSI interface of the soft palate and the surrounded walls (such as human tongue and pharyngeal wall) to prohibit the soft palate from moving outside of the fluid domain during FSI iteration due to excessive displacement. This is a realistic physical condition since the movement of soft palate is restricted by the surrounded walls. In addition, the elements in the fluid domain progressively distort due to the movement of the FSI interface, especially for those near-wall elements. An offset of 0.5 mm was applied on the contact surface of the surrounded wall to prevent the near-wall elements in the fluid domain from being too distorted. More details on contact condition could be found in Bathe (1995).

6.1.3 Mathematical modeling of the upper airway

Periodic sinusoidal variation of velocity magnitude was applied at the end of the oropharynx in the model which corresponds to ventilation rate of 7.5 L/min. As shown in Figure 6.2, each cycle of respiration takes 4 seconds corresponding to about 15 breaths per minute.

Table 6.1 shows the Reynolds numbers in cross sections along the nasal airway at peak inspiration/expiration calculated using equation 3.2. The highest Reynolds number was found to be 1002.62 around the nostril. In addition, it was reported that fully developed turbulence would not be reached until a flow rate of 30 L/min (Schreck et al., 1993), while the peak flow rate in the current study was less than 24 L/min. Therefore the airflow was presumed as incompressible and laminar. The surface of the nasal cavity, pharyngeal wall and tongue were assumed as fixed walls. During the simulation, equations 2.28 and 2.29 were solved to obtain airflow properties in the fluid domain.

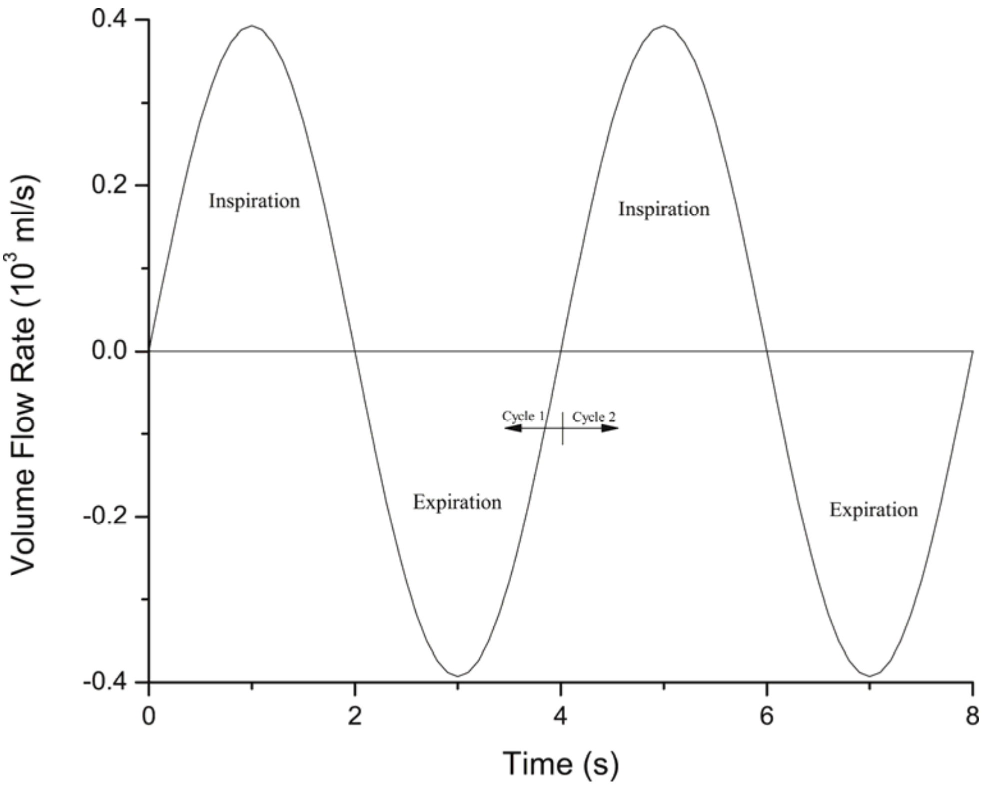

Figure 6.2 Velocity load. Sine pattern of velocity magnitude was applied at the oropharynx which corresponds to ventilation rate of 7.5 L/min. Each cycle of respiration takes 4 seconds corresponding to 15 breaths per minute. Within one cycle, inspiration happens in the first 2 seconds followed by expiration.

Table 6.1 Reynolds number along the nasal cavity at peak inspiration/expiration.

Cross Sections	Areas (mm^2)	Perimeter (mm)	Hydraulic Diameter (mm)	Reynolds Number
Nostril	268.39	107.25	10.01	1002.62
Middle Turbinate	347.63	794.40	1.75	135.37
Oropharynx	195.24	108.41	7.20	991.92

6.1.4 FSI simulation

Commercial software ADINA was used for solving all the equations of fluid, structure, contact of the structure and FSI. Due to consecutive displacement of the structure during simulation, some of the elements in fluid domain would become excessively distorted or even overlapped. Once this condition happened, the adaptive mesh function in ADINA would be applied to re-mesh the collapsed element and map the results from the previous step to the current fluid domain. The results before and after mapping process were carefully verified. The simulation was then restarted for the remaining time steps.

As shown in Table 6.2, three models have been simulated: model I is the CFD model of the fluid domain for comparison; model II is the FSI model with palatal modulus of 7539 Pa; and model III is the FSI model with palatal modulus of 3000 Pa.

Table 6.2 Numerical models.

	Model I	Model II	Model III
Description	Fluid	Fluid/Structure Interaction $E = 7539\text{Pa}\ \ \nu = 0.49$	Fluid/Structure Interaction $E = 3000\text{Pa}\ \ \nu = 0.49$

6.2 Results

6.2.1 Integrated forces over interface of soft palate

Figure 6.3 shows the integrated forces over the FSI interface in sagittal/coronal/axial directions of the three models. The total integrated force consists of integrated force from shear stress and integrated force from pressure of the airflow. The integrated shear force was much smaller than the corresponding integrated pressure force. The total integrated force in sagittal direction was much smaller than the other two directions. In sagittal direction, Sine-like shape with 180 degree phase shift of total force variation with time was found in model I, while the force patterns were more irregular in models II and III. Sine-like shape of the total force variation with time was found in coronal direction. The absolute total coronal force was generally larger during inspiration than expiration at the same interval. The shape of coronal force during expiration was flatter in FSI models. Sine-like shape with 180 degree phase shift of axial force variation with time was shown in all the three models. The maximum total axial forces were comparable among the three models.

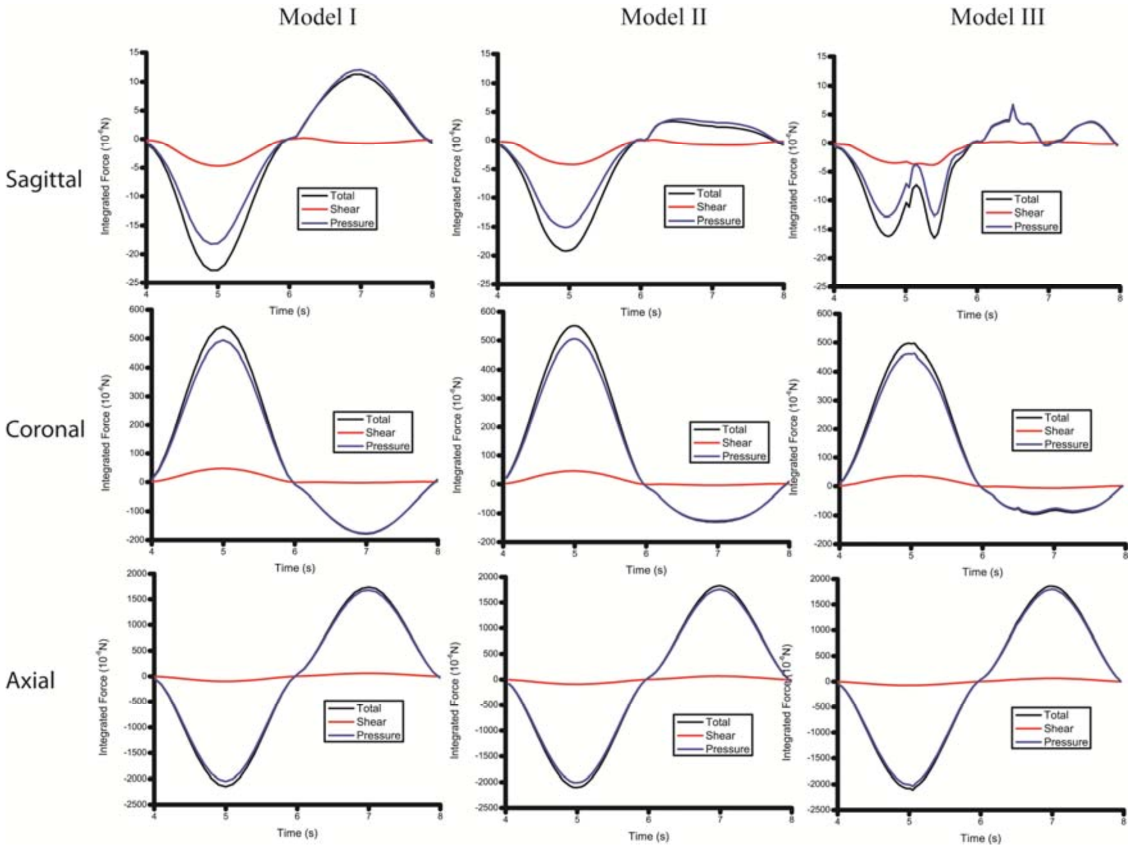

Figure 6.3 Total integrated forces (Total), forces integrated from shear stress (Shear) and normal pressure (Pressure) in sagittal, coronal and axial directions of the three models.

6.2.2 Pressure contours on interface of soft palate

Figure 6.4 shows the pressure distribution on FSI interface at the time of peak load. During inspiration, the anterior pressure was lower than posterior pressure in superior region at the same axial level (solid line 1) while larger in inferior region (solid line 2). At the same coronal level (dash line), the pressure around the superior surface was larger than the inferior surface along the soft palate. During expiration, the pressure on the lower surface was similar to the upper surface. The largest pressure appeared around the inferior-anterior side of the palate (black circle). The distributive patterns of pressure were alike between models II and III.

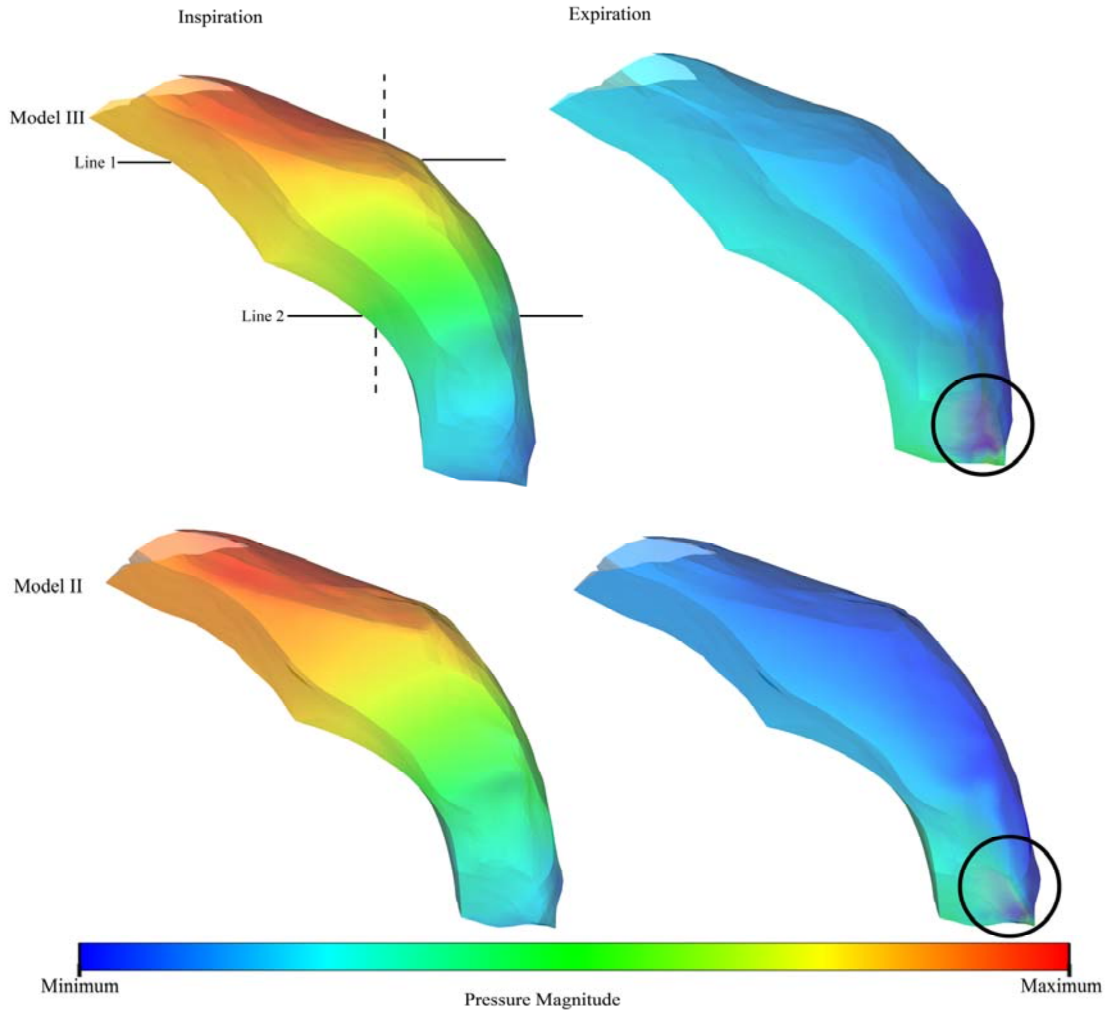

Figure 6.4 Transparent view of pressure distribution on the FSI interface at the time of peak load during inspiration/expiration in models II and III.

6.2.3 Displacement contours of interface of soft palate

Figure 6.5 shows the displacement of the FSI interface at peak loads during inspiration and expiration. The displacements in all the three directions during inspiration were quite small. The maximum absolute inspirational displacement was found to be 0.36 mm in sagittal direction in model III. During peak expiration, considerable amount of displacement was found in coronal and axial directions. The displacement in model II was generally smaller than that of model III. The maximum displacement magnitude of the soft palate was found to be 1.49 mm in model III and 0.87 mm in model II at the expiratory peak.

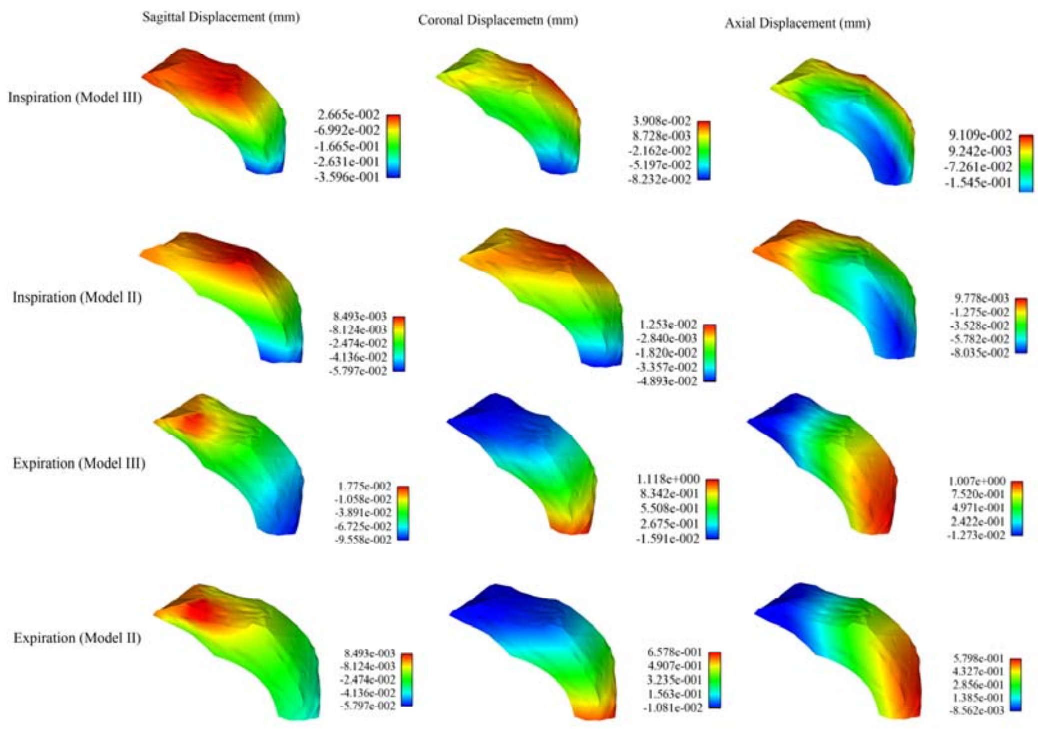

Figure 6.5 Contours of sagittal, coronal and axial displacements on FSI interface at the peak loads of inspiration and expiration in models II and III.

6.2.4 Average pressure at nasopharynx and oropharynx

Figure 6.6 shows the mean pressure of cross sections at nasopharynx and oropharynx. The mean pressures at the nasopharynx were almost the same in all the three models. However, slight difference of mean pressure was found at oropharynx between model III and models I and II. The absolute mean pressure at nasopharynx during inspiration was almost the same as expiration at the same time interval. The absolute mean pressure at oropharynx during inspiration was larger than expiration.

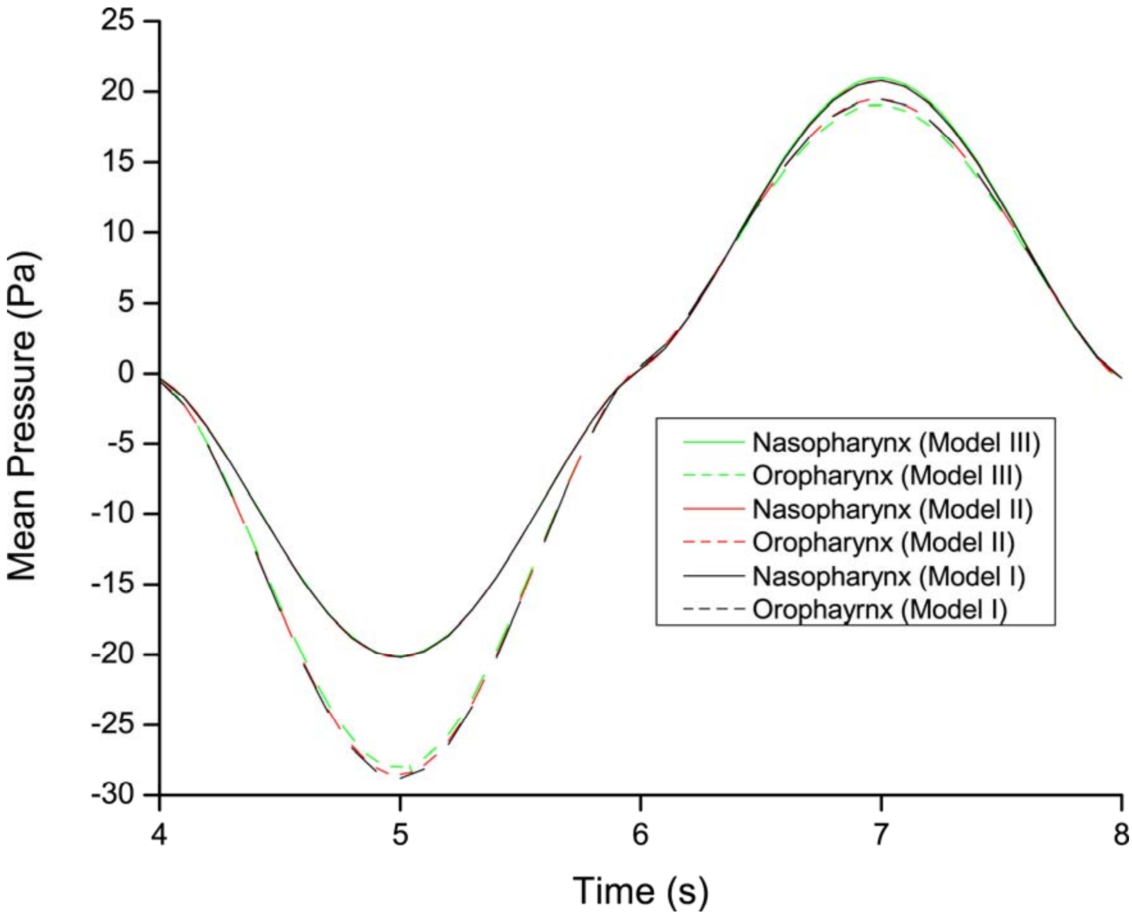

Figure 6.6 Mean pressure at the nasopharynx and oropharynx during one respiratory cycle in the three models.

6.2.5 CSAs of retropalatal cross sections

Figure 6.7 shows the CSAs of the five retropalatal sections depicted in Figure 6.1(a) in all the three models. The CSAs during inspiration was quite stable in FSI models compared to expiration. CSAs of sections 1 and 2 tended to decrease during expiration with increased CSAs of sections 3 and 4 compared to the original CSAs in model I. The peak change of CSA caused by compliance of soft palate appeared at the peak load of expiration. Compared to model I, the maximum change of CSA was found to be 10.01 and 4.66 mm^2 in section 2 of model III and model II, respectively. There was an observable offset between the two CSA lines from the two FSI models in the first four sections. For example, the CSAs in sections 1 and 2 were generally larger in model II than model III, while smaller in sections 3 and 4. The CSA in section 5 between the two FSI models during respiration were comparable possibly because the CSA of the palatal tip was quite small compared to the CSA of the airway. Moreover, the CSA variation with time was smoother in model II than model III.

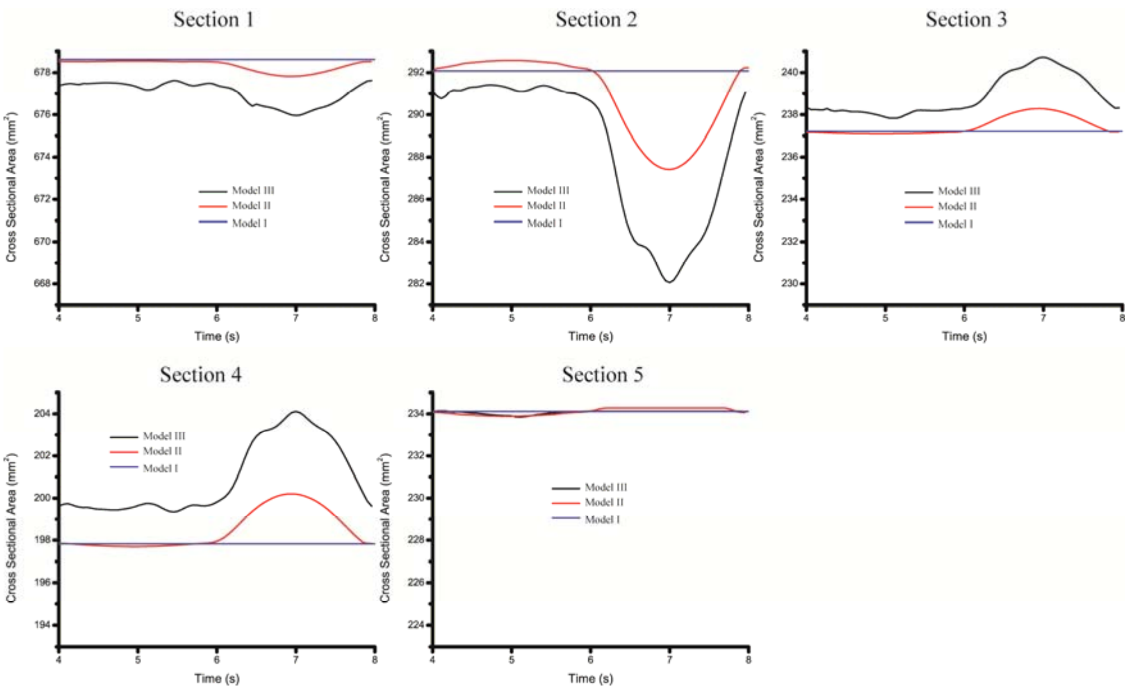

Figure 6.7 CSAs of cross sections 1 to 5 during one respiratory cycle in the three models.

6.2.6 Velocity vectors of sagittal cross section of nasal airway

Figure 6.8 shows the velocity vectors of the sagittal cross section at peak inspiration and expiration in model II. High velocity magnitude was found right before the turbinate head during inspiration, and around the nasal vestibule during expiration. At the same volume flow rate, the air centralized in the middle of the oropharynx at the peak expiration, while the velocity distributed more even through the pharynx at the peak inspiration. In addition, the velocity magnitude in the gap between soft palate and tongue is quite minimal. The distributions of velocity vectors in the other two models (models I and III) are similar.

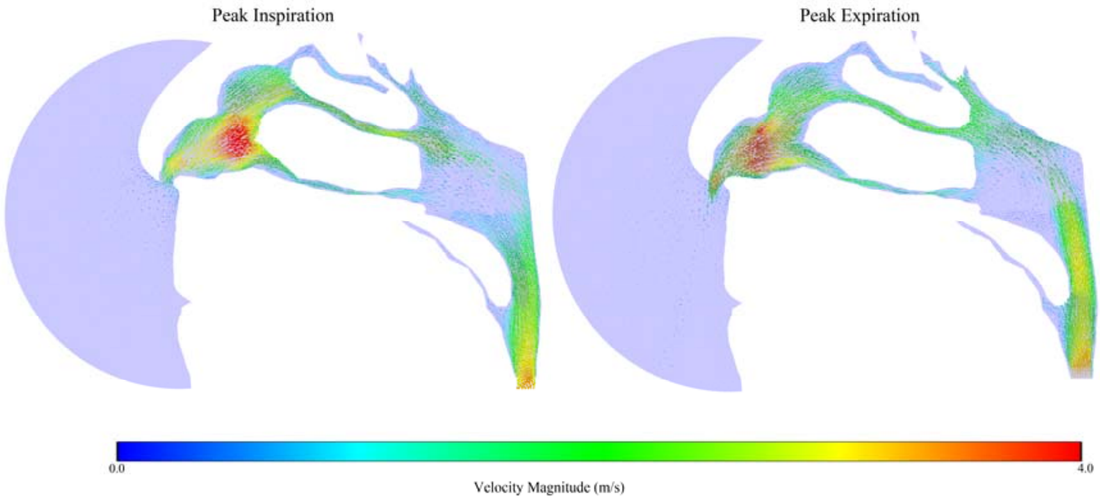

Figure 6.8 Velocity vector contours at peak inspiration and expiration in model II.

6.3 Discussion

The total forces which induced motion of the soft palate mainly resulted from the integrated pressure on the interface of soft palate. The integrated total axial force on the interface was the largest of the three forces, since the flow streamlines mainly lied in the axial direction which resulted in the largest pressure gradient. The expiratory coronal force was much smaller than inspirational coronal force at the same load. This could be because that during expiration the pressure on lower surface was similar to the pressure on upper surface of soft palate. Moreover, with larger displacement of soft palate in model III, the expiratory coronal force became smaller compared to the other two models.

In model II, the palate was almost static during inspiration with considerable posterior coronal force and tended to move posteriorly during expiration with anterior coronal force. This might be because that the integrated total axial force was nearly three times as integrated total coronal force. A resulted clockwise moment according to the fixation (Figure 6.1(c)) was formed from the summation of axial and coronal forces during inspiration rotating the soft palate clockwise towards the tongue. An anticlockwise moment was formed during expiration which moved the soft palate posteriorly and superiorly during expiration. In model II, the inspirational absolute displacement was smaller than 0.09 mm (Figure 6.5) which might be due to the contact condition between the palate and posterior surface of the tongue restricting the clockwise motion of the palate. In model III, the largest absolute displacement during inspiration was found to be the sagittal displacement (0.36 mm). As the integrated sagittal force was almost negligible, this amount of sagittal displacement might be caused by the contact force between the two contact surfaces. The tendency of expiratory posterior motion of soft palate in healthy subject could be observed with dynamic upper airway imaging (Akan et al., 2004).

Schwab et al. (1993), using dynamic imaging, reported decreased upper airway CSAs during early inspiration and increased CSAs in early expiration in normal human subjects. Upper airway occlusion was reported with sub-atmospheric nasal pressure in healthy human subjects (Schwartz et al., 1988). These phenomena are reasonable as during inspiration the sub-atmospheric pressure in upper airway produces normal forces towards the interior of the lumen on the airway surface to collapse the airway. During expiration, on the other hand, the above atmospheric pressure tended to enlarge the upper airway for the same reason. However, evidences of pharyngeal occlusion at the end of expiration were found in OSAHS patients (Dempsey et al., 2010; Morrell et al., 1998; Verbraecken and De Backer, 2009). The rationale of expiratory collapse/occlusion has not been fully understood. Based upon the current study, one of the possible reasons might be due to the posterior motion of human soft palate which decreased the air space between posterior surface of palate and posterior pharyngeal wall. Particularly, the retropalatal airway is narrower in OSAHS patients than healthy subjects and thus much easier to be occluded by the movement of palate (Ciscar et al., 2001; Isono et al., 1997). The maximum difference of CSA in retropalatal airway between inspiration and expiration in Schwab et al. (1993)'s study was around 60 mm^2. Regardless of the other tissues such as the tongue and pharyngeal wall, the change of retropalatal CSA due to the motion of the soft palate alone could be as large as 10.01 mm^2 in model III and 4.66 mm^2 in model II.

The upper airway dilator muscles are less active during sleep than awake state in both healthy subjects and OSAHS patients (Eckert et al., 2009). The muscle relaxation is directly related to airway narrowing in OSAHS patients (Pierce et al., 2007). This is reasonable since the activation hardens the upper airway dilator muscles to maintain the regular shape of the airway, while muscle relaxation softens the muscles and make the airway more collapsible. The current model did not consider the activation of the muscle fibers. However, we do observed a more compliant palate with softer material property in model III. Therefore, the relaxation of the soft palate can induce larger posterior displacement and smaller retropalatal space during expiration. Nevertheless, how much softer could the soft palate be due to muscle relaxation is still a question. As reported by Birch and Srodon (2009), the ex vivo Young's modulus could be as low as 585 Pa.

Although the changes of CSAs are larger in model III than model II, the flow fields between the two FSI models were similar based on the pressure distribution around the surface of the palate (Figure 6.4) and the average pressure along the pharynx (Figure 6.6). This might be because that the changes of CSAs are insignificant compared to the gross value of CSAs, e.g. the largest ratio between the change of CSA and the gross value of CSA is 3.43%. Therefore, in both models II and III the movement of soft palate did not change the retropalatal air space and the airflow much. This is reasonable since the current airway and structure geometry were extracted from a healthy subject. However, in some of the subjects with narrower retropalatal air space such as OSAHS patients the movement of soft palate would be troublesome. The motion of the palate was much influenced by the modulus as the maximum displacement increased from 0.87 mm in model II to 1.49 mm in model III.

There are a number of treatments which could be applied to prevent pharyngeal collapse and alleviate OSAHS. Continuous positive airway pressure is one of the main procedures. The continuous positive pressure loaded around the nostrils could keep the upper airway pressure positive to enlarge the whole airway. Uvulopalatopharyngoplasty and mandibular advancement device are therapies which also intend to enlarge the retropalatal airway patency. Soft palate stiffening via implants has been reported to be effective for mild to moderate OSAHS (Nordgård et al., 2006). However, researchers also reported that direct interventions on soft palate such as UPPP and soft palate implants were not always effective for OSAHS patients (Friedman et al., 2006). Based upon the current study, we hypothesize that there are two major causes that induce pharyngeal collapse: the negative pressure during inspiration and the posterior movement of the soft palate during expiration. The question as to which cause (or both) induces airway collapse in a specific patient should be carefully considered before making the decision on OSAHS therapy. For example, though the CPAP could enlarge the airway, the soft palate would still move posteriorly during expiration as long as the anticlockwise moment resulted from expiratory airflow exists. Moreover, if the inspirational negative pressure is the main inducement of airway collapse, the effect of stiffening of soft palate might be unsatisfactory.

6.4 Summary

This chapter, by reconstructing a 3D FSI upper airway model from MRI images, studied the movement of human soft palate during respiration at 7.5 L/min. A tendency of posterior movement of the soft palate toward the posterior pharyngeal wall was found during expiration, which could be one of the reasons for expiratory upper airway occlusion; while the soft palate tended to move anteriorly during inspiration. The displacement of human soft palate during respiration was mainly driven by respiratory air pressure around the surface of palate with effects of shear stress to be minimal. Referring to the FSI, the fluid stress on the interface caused considerable displacement of the soft palate, while the influence of palatal movement on flow properties was quite limited. The displacement of soft palate increased with decreased Young's modulus, indicating that with a softer soft palate during sleep compared to wake state, the airway is more collapsible.

Chapter 7 Conclusion and Recommendations

7.1 Conclusions of the results

This work aimed to study airflow patterns in human nasal and pharyngeal airways during respiration using numerical simulation such as CFD and FSI. 3D nasal models of Caucasian, Chinese and Indian individuals were firstly reconstructed to evaluate effects of the variation of nasal morphologies among ethnic groups on nasal airflow patterns. We then studied nasal airflow in deformed nasal cavities, such as airflow patterns in nasal cavities with bone fracture and nasal cavities with crooked external noses. Besides nasal cavity, the airflow ventilation through human maxillary sinuses with accessory ostium was also assessed. A 3D FSI model including both the nasal cavity and pharynx was reconstructed to study the dynamic displacement pattern of human soft palate during respiration. These studies provide a comprehensive understanding on human upper airway respiration. In addition, the successful implementation of numerical methods on human upper airway flow, using CT and MRI scans, indicates that numerical simulation is a useful tool for investigating upper airway flow and diagnosing air-related upper airway diseases.

7.1.1 Nasal airflow patterns among Caucasian, Chinese and Indian individuals

By comparing airflow through nasal airways of three individuals from Caucasian, Chinese and Indian ethnic groups, the airflow patterns were found to be much different in these nasal cavities. For example, more airflow tended to pass through the middle passage of the nasal airway in Caucasian, and through the inferior portion in the Indian model. These differences of airflow distribution might be associated with different nasal structures, especially the nasal indices among races. Compared to the other two races, extremely low airflow was found around the olfaction region in Indian model. The nasal airflow is much influenced by the anterior nasal structures, such as the angle between the upper vestibule wall and the anterior nasal roof, and the angle between the upper vestibule wall and the nasal bottom.

7.1.2 Case studies of airflow in deformed human nasal cavities

Besides the congenital difference of nasal morphologies among ethnic groups, other factors, such as bone fracture can severely deform nasal cavity and affect breathing activity which require cautious surgical operation. In this work, 3D nasal models of a patient with orbito-maxillary fracture were reconstructed and simulated. The results show that the surgical intervention significantly restored the collapsed nasal airway by fracture with decreased nasal resistance, more even flow partitioning and more continuous streamlines. However, local discontinuity of air space still existed in post-operative model which disturbed the airflow distribution especially around the superior region. This finding suggests that surgeons shall pay more attention on the continuity of the nasal geometry along the turbinates especially in the superior region.

The crookedness of external noses is another cause of nasal airway deformation. By examining nasal airflow in individuals with three typical deviation patterns of external noses (S-shape, C-shape and slanted), one anterior nasal roof was found to be collapsed in each of these individuals, leaving the anterior portion of the other nasal airway less affected. The external deviation also caused internal airway blockage along the turbinates.

The anterior airway collapse produced vortexes around the anterior nasal roof. It also induced high wall shear stress near the collapsed region, and higher nasal resistance compared to un-deviated nasal nose. The largest nasal resistance was found in the S-shaped case, followed by the slanted and C-shaped cases. The internal blockage, on the other hand, further increased the nasal resistance and disturbed the airflow properties such as wall shear stress and streamlines.

7.1.3 Air ventilation through human maxillary sinus

Despite nasal airflow, the air ventilation through human maxillary sinus is of equal importance considering the high prevalence of sinusitis among human beings. Particularly, the existence of AO was thought to be one of the main causes of sinus diseases. Through our simulation, the existence of AO was found to markedly boost air ventilation through maxillary sinus. In the absence of AO, however, the airflow reaching the interior of maxillary sinus is very limited. The flow rate through a sinus with two AOs is comparable to a sinus with one AO; the presence of two AOs complicates the flow partitioning of the gross maxillary sinus ventilation among the ostia. Accessory ostia also may affect the direction of flow through the NO. Whether these alterations have an impact on physiology or pathophysiology of the sinuses remains unknown, and needs to be investigated by future human studies.

7.1.4 Interaction between pharyngeal airflow and movement of human soft palate

Other than geometry of nasal cavity, the dynamic movement of tissues during breathing in human pharynx brings more complicated issues. For example, the displacement of soft tissues at retropalatal level would occlude the whole airway in OSA patients. A comprehensive 3D FSI upper airway model was reconstructed to evaluate the dynamic movement of human soft palate during respiration. The palate was found to move towards the posterior pharyngeal wall during expiration and towards the tongue during inspiration. This finding implies that the expiratory occlusion of the upper airway could be triggered by the posterior displacement of the soft palate. In addition, the displacement of human soft palate was mainly driven by respiratory air pressure around the surface of soft palate with limited contribution of shear stress. The displacement of soft palate increased with decreased Young's modulus, indicating that with a softer soft palate during sleep compared to wake state, the airway is more collapsible.

7.2 Recommendation for future work

There could be several tasks for future work as listed below:

1. Due to the scope of this dissertation, currently we mainly focused on the airflow patterns through human nasal and pharyngeal airways. However, the other functions of human upper airway, such as filtration of deleterious particles and bacteria, olfaction, humidification and temperature regulation of respiratory air are also very important to maintain a healthy life quality. Particularly, different races have adapted their nasal morphology to the environment, which might exhibit different efficiencies of nasal functions. In the next stage, we could evaluate differences of efficiencies of nasal functions among races using numerical simulation.

2. The present FSI model only evaluated dynamic movement of human soft palate during respiration, which showed a prominent anterior-posterior motion of the palate. However, the lateral upper airway dimensional changes were also reported to be vital (Schwab et al., 1996). A more complete structural model including all the surrounding pharyngeal soft tissues (the tongue, the soft palate and the pharyngeal wall) is needed to arrive at the whole picture of respiratory compromise of human upper airway.

3. Some of the medicines are designed to be taken through nasal or oral airway such as asthma powder. However, due to the nature of human upper airway as a filter to prevent inhaled particles from reaching the lower airways, the efficiency of the intake of medical powder is greatly compromised. In the future, numerical simulations can be carried out to investigate the interaction between inhaled particles and upper airway flow to optimize the efficiency of the intake of medical powder.

REFERENCES

ADINA R & D Inc.,（2010）. ADINA System Online Manuals.

Akan Huseyin, Aksoz Tolga, Belet Umit, Sesen Teoman, 2004. Dynamic Upper Airway Soft-Tissue and Caliber Changes in Healthy Subjects and Snoring Patients. AJNR Am J Neuroradiol 25, 1846-1850.

ANSYS Inc.,（2009）. ANSYS FLUENT 12.0/12.1 Documentation.

Aust R, Drettner B, 1974a. The Functional Size of the Human Maxillary Ostium in Vivo. Acta Oto-laryngologica 78, 432-435.

Aust R, Drettner B, 1974b. Oxygen tension in the human maxillary sinus under normal and pathological conditions. Acta Otolaryngol 78, 264-269.

Bailie N., Hanna B., Watterson J., Gallagher G., 2006. An overview of numerical modelling of nasal airflow. Rhinology 44, 53-57.

Bathe Klaus-Jürgen,（1995）. Finite Element Procedures.

Bathe Klaus-Jürgen, Zhang Hou, 2004. Finite element developments for general fluid flows with structural interactions. International Journal for Numerical Methods in Engineering 60, 213-232.

Benchetrit G., 2000. Breathing pattern in humans: diversity and individuality. Respir Physiol 122, 123-129.

Benchetrit G., Shea S. A., Dinh T. Pham, Bodocco S., Baconnier P., Guz A., 1989. Individuality of breathing patterns in adults assessed over time. Respiration Physiology 75, 199-209.

Bennett William D, Zeman Kirby L, 2005. Effect of Race on Fine Particle Deposition for Oral and Nasal Breathing. Inhalation Toxicology 17, 641-648.

Birch M J, Srodon P D, 2009. Biomechanical Properties of the Human Soft Palate. The Cleft Palate-Craniofacial Journal 46, 268-274.

Caballero P, Alvarez-Sala R, Garcia-Rio F, Prados C, Hernan M A, Villamor J, Alvarez-Sala J L, 1998. CT in the evaluation of the upper airway in healthy subjects and in patients with obstructive sleep apnea syndrome. Chest 113, 111-116.

Chen X B, Lee H P, Chong V F H, Wang D Y, 2012. Drug delivery in the nasal cavity after functional endoscopic sinus surgery: a computational fluid dynamics study. The Journal of Laryngology & Otology 126, 487-494.

Chen Xiao Bing, Lee Heow Pueh, Chong Vincent Fook Hin, Wang De Yun, 2009. Assessment of septal deviation effects on nasal air flow: A computational fluid dynamics model. The Laryngoscope 119, 1730-1736.

Chen Xiao Bing, Lee Heow Pueh, Chong Vincent Fook Hin, Wang De Yun, 2011. Assessments of nasal bone fracture effects on nasal airflow: A computational fluid dynamics study. American Journal of Rhinology Allergy 25, e39-e43.

Cheng S, Gandevia S C, Green M, Sinkus R, Bilston L E, 2011. Viscoelastic properties of the tongue and soft palate using MR elastography. J Biomech 44, 450-454.

Cheng Yongguang, Oertel Herbert, Schenkel Torsten, 2005. Fluid-Structure Coupled CFD Simulation of the Left Ventricular Flow During Filling Phase. Annals of Biomedical Engineering 33, 567-576.

Chouly F, Van Hirtum A, Lagrée P Y, Pelorson X, Payan Y, 2008. Numerical and experimental study of expiratory flow in the case of major upper airway obstructions with fluid-structure interaction. Journal of Fluids and Structures 24, 250-269.

Chun K W, Han S K, Kim S B, Kim W K, 2009. Influence of nasal bone fracture and its reduction on the airway. Ann Plast Surg 63, 63-66.

Chung S K, Cho D Y, Dhong H J, 2002. Computed tomogram findings of mucous recirculation between the natural and accessory ostia of the maxillary sinus. Am J Rhinol 16, 265-268.

Chung S K, Dhong H J, Na D G, 1999. Mucus circulation between accessory ostium and natural ostium of maxillary sinus. The Journal of Laryngology & Otology 113, 865-867.

Ciscar M A, Juan G, Martinez V, Ramon M, Lloret T, Minguez J, Armengot M, Marin J, Basterra J, 2001. Magnetic resonance imaging of the pharynx in OSA patients and healthy subjects. Eur Respir J 17, 79-86.

Croce Céline, Fodil Redouane, Durand Marc, Sbirlea-Apiou Gabriela, Caillibotte Georges, Papon Jean-François, Blondeau Jean-Robert, Coste André, Isabey Daniel, Louis Bruno, 2006. In Vitro Experiments and Numerical Simulations of Airflow in Realistic Nasal Airway Geometry. Annals of Biomedical Engineering 34, 997-1007.

Crouse Ulla, Laine-Alava M T, 1999. Effects of Age, Body Mass Index, and Gender on Nasal Airflow Rate and Pressures. The Laryngoscope 109, 1503-1508.

Davies A, 1932. A Re-Survey of the Morphology of the Nose in Relation to Climate. The Journal of the Royal Anthropological Institute of Great Britain and Ireland 62, 337-359.

Deja Maria, Busch Thilo, Bachmann Sebastian, Riskowski Kerstin, Câmpean Valentina, Wiedmann Brigitte, Schwabe Michael, Hell Bertold, Pfeilschifter Josef, Falke Konrad J., Lewandowski Klaus, 2003. Reduced Nitric Oxide in Sinus Epithelium of Patients with Radiologic Maxillary Sinusitis and Sepsis. American Journal of Respiratory and Critical Care Medicine 168, 281-286.

Dempsey Jerome A, Veasey Sigrid C, Morgan Barbara J, O'Donnell Christopher P, 2010. Pathophysiology of Sleep Apnea. Physiological Reviews 90, 47-112.

Doorly D J, Taylor D J, Schroter R C, 2008a. Mechanics of airflow in the human nasal airways. Respiratory Physiology & Neurobiology 163, 100-110.

Doorly D, Taylor D J, Franke P, Schroter R C, 2008b. Experimental investigation of nasal airflow. Proceedings of the Institution of Mechanical Engineers, Part H: Journal of Engineering in Medicine 222, 439-453.

Doyle Matthew, Tavoularis Stavros, Bourgault Yves, (2010). Application of Parallel Processing to the Simulation of Heart Mechanics.

Eckert Danny J., Malhotra Atul, Lo Yu L., White David P., Jordan Amy S., 2009. The Influence of Obstructive Sleep Apnea and Gender on Genioglossus Activity During Rapid Eye Movement Sleep. Chest 135, 957-964.

Foda H M, 2005. The role of septal surgery in management of the deviated nose. Plast Reconstr Surg 115, 406-415.

Fontanari P, Burnet H, Zattara-Hartmann M C, Jammes Y, 1996. Changes in airway resistance induced by nasal inhalation of cold dry, dry, or moist air in normal individuals. J Appl Physiol 81, 1739-1743.

Franciscus Robert G., Long Jeffrey C., 1991. Variation in human nasal height and breadth. American Journal of Physical Anthropology 85, 419-427.

Friedman M, Schalch P, Joseph N J, 2006. Palatal stiffening after failed uvulopalatopharyngoplasty with the Pillar Implant System. Laryngoscope 116, 1956-1961.

Garcia Guilherme J M, Bailie Neil, Martins Dario A, Kimbell Julia S, 2007. Atrophic rhinitis: a CFD study of air conditioning in the nasal cavity. J Appl Physiol 103, 1082-1092.

Garcia Guilherme J M, Rhee John S, Senior Brent A, Kimbell Julia S, 2010. Septal deviation and nasal resistance: An investigation using virtual surgery and computational fluid dynamics. American Journal of Rhinology & Allergy 24, e46-e53.

Ge Qin Jiang, Inthavong Kiao, Tu Ji Yuan, 2012. Local deposition fractions of ultrafine particles in a human nasal-sinus cavity CFD model. Inhalation Toxicology 24, 492-505.

Gosepath J, Belafsky P, Kaldenbach T, Rolfe K W, Mann W J, Amedee R G, 2000. The use of acoustic rhinometry in predicting outcomes after sinonasal surgery. Am J Rhinol 14, 97-100.

Granqvist S, Sundberg J, Lundberg J O, Weitzberg E, 2006. Paranasal sinus ventilation by humming. J Acoust Soc Am 119, 2611-2617.

Guilleminault C., Tilkian A., Dement W. C., 1976. The sleep apnea syndromes. Annu Rev Med 27, 465-484.

Haarmann S, Budihardja A S, Wolff K D, Wangerin K, 2009. Changes in acoustic airway profiles and nasal airway resistance after Le Fort I osteotomy and functional rhinosurgery: a prospective study. Int J Oral Maxillofac Surg 38, 321-325.

Hahn I, Scherer P W, Mozell M M, 1993. Velocity profiles measured for airflow through a large-scale model of the human nasal cavity. J Appl Physiol 75, 2273-2287.

Hahn Intaek, Scherer Peter W, Mozell Maxwell M, 1994. A Mass Transport Model of Olfaction. Journal of Theoretical Biology 167, 115-128.

Higuera S, Lee E I, Cole P, Hollier Jr. L H, Stal S, 2007. Nasal trauma and the deviated nose. Plast Reconstr Surg 120, 64S-75S.

Hirschberg A, Roithmann R, Parikh S, Miljeteig H, Cole P, 1995. The airflow resistance profile of healthy nasal cavities. Rhinology 33, 10-13.

Hoffmann John F, 1999. Management of the twisted nose. Operative Techniques in Otolaryngology - Head and Neck Surgery 10, 232-237.

Hollandt Jan H, Mahlerwein Malte, 2003. Nasal Breathing and Continuous Positive Airway Pressure (CPAP) in Patients with Obstructive Sleep Apnea (OSA). Sleep and Breathing 7, 87-93.

Hood C M, Schroter R C, Doorly D J, Blenke E J, Tolley N S, 2009. Computational modeling of flow and gas exchange in models of the human maxillary sinus. J Appl Physiol 107, 1195-1203.

Hörschler I, Schröder W, Meinke M, 2010. On the assumption of steadiness of nasal cavity flow. Journal of Biomechanics 43, 1081-1085.

Höschler I, Meinke M, Schröer W, 2003. Numerical simulation of the flow field in a model of the nasal cavity. Computers & Fluids 32, 39-45.

Huang Y, Malhotra A, White D P, 2005a. Computational simulation of human upper airway collapse using a pressure-/state-dependent model of genioglossal muscle contraction under laminar flow conditions. J Appl Physiol 99, 1138-1148.

Huang Y, White D P, Malhotra A, 2005b. The impact of anatomic manipulations on pharyngeal collapse: results from a computational model of the normal human upper airway. Chest 128, 1324-1330.

Huang Z. L., Wang D. Y., Zhang P. C., Dong F., Yeoh K. H., 2001. Evaluation of Nasal Cavity by Acoustic Rhinometry in Chinese, Malay and Indian Ethnic Groups. Acta Oto-laryngologica 121, 844-848.

Isono Shiroh, Remmers John E, Tanaka Atsuko, Sho Yasuhide, Sato Jiro, Nishino Takashi, 1997. Anatomy of pharynx in patients with obstructive sleep apnea and in normal subjects. Journal of Applied Physiology 82, 1319-1326.

Jeong S J, Kim W S, Sung S J, 2007. Numerical investigation on the flow characteristics and aerodynamic force of the upper airway of patient with obstructive sleep apnea using computational fluid dynamics. Med Eng Phys 29, 637-651.

Jog M, McGarry G W, 2003. How frequent are accessory sinus ostia? J Laryngol Otol 117, 270-272.

Kaliner Michael A, Osguthorpe J David, Fireman Philip, Anon Jack, Georgitis John, Davis Mary L, Naclerio Robert, Kennedy David, 1997. Sinusitis: Bench to bedside: Current findings, future directions. Journal of Allergy and Clinical Immunology 99, S829-S847.

Kane Kevinj, 1997. Recirculation of Mucus as a Cause of Persistent Sinusitis. American Journal of Rhinology 11, 361-369.

Keyhani K, Scherer P W, Mozell M M, 1995. Numerical simulation of airflow in the human nasal cavity. J Biomech Eng 117, 429-441.

Keyhani K, Scherer P W, Mozell M M, 1997. A numerical model of nasal odorant transport for the analysis of human olfaction. J Theor Biol 186, 279-301.

Kim C S, Greene M A, Sankaran S, Sackner M A, 1986. Mucus transport in the airways by two-phase gas-liquid flow mechanism: continuous flow model. Journal of Applied Physiology 60, 908-917.

Kocer U, 2001. Effect of aesthetic rhinoplasty on respiratory functions. Aesthetic Plast Surg 25, 202-206.

Koren A, Groselj L D, Fajdiga I, 2009. CT comparison of primary snoring and obstructive sleep apnea syndrome: role of pharyngeal narrowing ratio and soft palate-tongue contact in awake patient. Eur Arch Otorhinolaryngol 266, 727-734.

Kumar H, Choudhary R, Kakar S, 2001. Accessory maxillary ostia: topography and clinical application. Journal of the Anatomical Society of India 50, 3-5.

Lee C H, Mo J H, Kim B J, Kong I G, Yoon I Y, Chung S, Kim J H, Kim J W, 2009. Evaluation of soft palate changes using sleep videofluoroscopy in patients with obstructive sleep apnea. Arch Otolaryngol Head Neck Surg 135, 168-172.

Lee Jong-Hoon, Na Yang, Kim Sung-Kyun, Chung Seung-Kyu, 2010. Unsteady flow characteristics through a human nasal airway. Respiratory Physiology & Neurobiology 172, 136-146.

Leong S C, Eccles R, 2009. A systematic review of the nasal index and the significance of the shape and size of the nose in rhinology. Clinical Otolaryngology 34, 191-198.

Leung J. H., Wright A. R., Cheshire N., Crane J., Thom S. A., Hughes A. D., Xu Y., 2006. Fluid structure interaction of patient specific abdominal aortic aneurysms: a comparison with solid stress models. Biomed Eng Online 5, 33.

Li Zheng, Kleinstreuer Clement, Zhang Zhe, 2007. Particle deposition in the human tracheobronchial airways due to transient inspiratory flow patterns. Journal of Aerosol Science 38, 625-644.

Liu Yuan, Matida Edgar A, Gu Junjie, Johnson Matthew R, 2007. Numerical simulation of aerosol deposition in a 3-D human nasal cavity using RANS, RANS/EIM, and LES. Journal of Aerosol Science 38, 683-700.

Macfarlane Eileen W E, Sarkar S S, 1941. Blood groups in India. American Journal of Physical Anthropology 28, 397-410.

Malve M, del Palomar A P, Lopez-Villalobos J L, Ginel A, Doblare M, 2010. FSI analysis of the coughing mechanism in a human trachea. Ann Biomed Eng 38, 1556-1565.

Matthews B L, Burke A J, 1997. Recirculation of mucus via accessory ostia causing chronic maxillary sinus disease. Otolaryngol Head Neck Surg 117, 422-423.

Möller Winfried, Münzing Wolfgang, Canis Martin, 2010. Clinical potential of pulsating aerosol for sinus drug delivery. Expert Opinion on Drug Delivery 7, 1239-1245.

Molony David, Callanan Anthony, Kavanagh Eamon, Walsh Michael, McGloughlin Tim, 2009. Fluid-structure interaction of a patient-specific abdominal aortic aneurysm treated with an endovascular stent-graft. BioMedical Engineering OnLine 8, 24.

Morrell M J, Arabi Y, Zahn B, Badr M S, 1998. Progressive retropalatal narrowing preceding obstructive apnea. Am J Respir Crit Care Med 158, 1974-1981.

Na Yang, Kim Kyunghun, Kim Sung Kyun, Chung Seung-Kyu, 2012. The quantitative effect of an accessory ostium on ventilation of the maxillary sinus. Respiratory Physiology & Neurobiology 181, 62-73.

Newman Marshall T, 1953. The Application of Ecological Rules to the Racial Anthropology of the Aboriginal New World. American Anthropologist 55, 311-327.

Niinimaa V., Cole P., Mintz S., Shephard R. J., 1980. The switching point from nasal to oronasal breathing. Respiration Physiology 42, 61-71.

Nordgård Ståle, Stene Brit Kari, Skjøstad Ketil Wichman, 2006. Soft Palate Implants for the Treatment of Mild to Moderate Obstructive Sleep Apnea. Otolaryngology -- Head and Neck Surgery 134, 565-570.

Okur E, Yildirim I, Aydogan B, Akif Kilic M, 2004. Outcome of surgery for crooked nose: an objective method of evaluation. Aesthetic Plast Surg 28, 203-207.

Ottaviano G., Scadding G. K., Coles S., Lund V. J., 2006. Peak nasal inspiratory flow; normal range in adult population. Rhinology 44, 32-35.

Pierce R., White D., Malhotra A., Edwards J. K., Kleverlaan D., Palmer L., Trinder J., 2007. Upper airway collapsibility, dilator muscle activation and resistance in sleep apnoea. European Respiratory Journal 30, 345-353.

Pless D., Keck T., Wiesmiller K., Rettinger G., Aschoff A. J., Fleiter T. R., Lindemann J., 2004. Numerical simulation of air temperature and airflow patterns in the human nose during expiration. Clinical Otolaryngology & Allied Sciences 29, 642-647.

Pontius Allison T, Leach Joseph L, 2004. New Techniques for Management of the Crooked Nose. Archives of Facial Plastic Surgery 6, 263-266.

Porter Jennifer, Toriumi Dean M, 2002. Surgical Techniques for Management of the Crooked Nose. Aesthetic Plastic Surgery 26, S18-S18.

Randerath Winfried J, Scanner B. M., Somers V. K., (2006). Sleep apnea current diagnosis and treatment.

Rennie Catherine E, Hood Christina M, Blenke Esther J S M, Schroter Robert S, Doorly Denis J, Jones Hazel, Towey David, Tolley Neil S, 2011. Physical and Computational Modeling of Ventilation of the Maxillary Sinus. Otolaryngology -- Head and Neck Surgery 145(1), 165-170.

Rohrich Rod J, Gunter Jack P, Deuber Mark A, Adams William P Jr., 2002. The Deviated Nose: Optimizing Results Using a Simplified Classification and Algorithmic Approach. Plastic and Reconstructive Surgery 110, 1509-1523.

Roithmann Renato, Cole Philip, Chapnik Jerry, Shpirer Isaac, Hoffstein Victor, Zamel Noe, 1995. Acoustic rhinometry in the evaluation of nasal obstruction. The Laryngoscope 105, 275-281.

Roy M, Becquemin M H, Bertholon J F, Bouchikhi A, 1994. Annexe B. Respiratory physiology. Annals of the ICRP 24, 167-201.

Sauerland E K, Harper R M, 1976. The human tongue during sleep: Electromyographic activity of the genioglossus muscle. Experimental Neurology 51, 160-170.

Schreck S, Sullivan K J, Ho C M, Chang H K, 1993. Correlations between flow resistance and geometry in a model of the human nose. J Appl Physiol 75, 1767-1775.

Schwab R J, Gefter W B, Pack A I, Hoffman E A, 1993. Dynamic imaging of the upper airway during respiration in normal subjects. J Appl Physiol 74, 1504-1514.

Schwab R J, Gupta K B, Gefter W B, Metzger L J, Hoffman E A, Pack A I, 1995. Upper airway and soft tissue anatomy in normal subjects and patients with sleep-disordered breathing. Significance of the lateral pharyngeal walls. Am. J. Respir. Crit. Care Med. 152, 1673-1689.

Schwab R J, Pack A I, Gupta K B, Metzger L J, Oh E, Getsy J E, Hoffman E A, Gefter W B, 1996. Upper airway and soft tissue structural changes induced by CPAP in normal subjects. Am. J. Respir. Crit. Care Med. 154, 1106-1116.

Schwab R J, Pasirstein M, Kaplan L, Pierson R, Mackley A, Hachadoorian R, Arens R, Maislin G, Pack A I, 2006. Family aggregation of upper airway soft tissue structures in normal subjects and patients with sleep apnea. Am J Respir Crit Care Med 173, 453-463.

Schwartz A R, Smith P L, Wise R A, Gold A R, Permutt S, 1988. Induction of upper airway occlusion in sleeping individuals with subatmospheric nasal pressure. Journal of Applied Physiology 64, 535-542.

Segal R A, Kepler G M, Kimbell J S, 2008. Effects of differences in nasal anatomy on airflow distribution: a comparison of four individuals at rest. Ann Biomed Eng 36, 1870-1882.

Shankar P. N., Deshpande M. D., 2000. Fluid Mechanics in the Driven Cavity. Annual Review of Fluid Mechanics 32, 93-136.

Shim Eun Bo, Yeo Jong Young, Ko Hyung Jong, Youn Chan Hyun, Lee Young Ro, Park Chan Young, Min Byoung Goo, Sun Kyung, 2003. Numerical Analysis of the Three-Dimensional Blood Flow in the Korean Artificial Heart. Artificial Organs 27, 49-60.

Shome B, Wang L P, Santare M H, Prasad A K, Szeri A Z, Roberts D, 1998. Modeling of airflow in the pharynx with application to sleep apnea. J Biomech Eng 120, 416-422.

Simmen D, Scherrer J L, Moe K, Heinz B, 1999. A dynamic and direct visualization model for the study of nasal airflow. Arch Otolaryngol Head Neck Surg 125, 1015-1021.

Subramaniam R P, Richardson R B, Morgan K T, Kimbell J S, Guilmette R A, 1998. Computational fluid dynamics simulations of inspiratory airflow in the human nose and nasopharynx. Inhalation Toxicology 10, 473-502.

Sudo K, Sumida M, Hibara H, 1998. Experimental investigation on turbulent flow in a circular-sectioned 90-degree bend. Experiments in Fluids 25, 42-49.

Sun Xiuzhen, Yu Chi, Wang Yuefang, Liu Yingxi, 2007. Numerical simulation of soft palate movement and airflow in human upper airway by fluid-structure interaction method. Acta Mechanica Sinica 23, 359-367.

Sung S J, Jeong S J, Yu Y S, Hwang C J, Pae E K, 2006. Customized three-dimensional computational fluid dynamics simulation of the upper airway of obstructive sleep apnea. Angle Orthodontist 76, 791-799.

Tang D, Yang C, Zheng J, Woodard P K, Sicard G A, Saffitz J E, Yuan C, 2004. 3D MRI-based multicomponent FSI models for atherosclerotic plaques. Ann Biomed Eng 32, 947-960.

Tang Dalin, Yang Chun, Huang Yan, N. Ku David, 1999a. Wall stress and strain analysis using a three-dimensional thick-wall model with fluid–structure interactions for blood flow in carotid arteries with stenoses. Computers & Structures 72, 341-356.

Tang Dalin, Yang Chun, N. Ku David, 1999b. A 3-D thin-wall model with fluid–structure interactions for blood flow in carotid arteries with symmetric and asymmetric stenoses. Computers & Structures 72, 357-377.

Taylor D J, Doorly D J, Schroter R C, 2010. Inflow boundary profile prescription for numerical simulation of nasal airflow. Journal of The Royal Society Interface 7, 515-527.

Tobin M J, Chadha T S, Jenouri G, Birch S J, Gazeroglu H B, Sackner M A, 1983. Breathing patterns. 1. Normal subjects. Chest 84, 202-205.

Valencia Alvaro, Baeza Fernando, 2009. Numerical simulation of fluid–structure interaction in stenotic arteries considering two layer nonlinear anisotropic structural model. International Communications in Heat and Mass Transfer 36, 137-142.

Valencia Alvaro, Solis Francisco, 2006. Blood flow dynamics and arterial wall interaction in a saccular aneurysm model of the basilar artery. Computers & Structures 84, 1326-1337.

Verbraecken J A, De Backer W A, 2009. Upper airway mechanics. Respiration 78, 121-133.

Weinhold Ivo, Mlynski Gunter, 2004. Numerical simulation of airflow in the human nose. European Archives of Oto-Rhino-Laryngology 261, 452-455.

Weitzberg E, Lundberg J O, 2002. Humming greatly increases nasal nitric oxide. Am J Respir Crit Care Med 166, 144-145.

Wen Jian, Inthavong Kiao, Tu Jiyuan, Wang Simin, 2008. Numerical simulations for detailed airflow dynamics in a human nasal cavity. Respiratory Physiology & Neurobiology 161, 125-135.

Wilcox D C,（1998）. Turbulence Modeling for CFD.

Xi Jinxiang, Longest P Worth, 2008. Numerical predictions of submicrometer aerosol deposition in the nasal cavity using a novel drift flux approach. International Journal of Heat and Mass Transfer 51, 5562-5577.

Xiong G X, Zhan J M, Jiang H Y, Li J F, Rong L W, Xu G, 2008. Computational fluid dynamics simulation of airflow in the normal nasal cavity and paranasal sinuses. American Journal of Rhinology 22, 477-482.

Yokley Todd R, 2009. Ecogeographic variation in human nasal passages. American Journal of Physical Anthropology 138, 11-22.

Young T, Palta M, Dempsey J, Skatrud J, Weber S, Badr S, 1993. The occurrence of sleep-disordered breathing among middle-aged adults. N Engl J Med 328, 1230-1235.

Yucel Aylin, Unlu Mehmet, Haktanir Alpay, Acar Murat, Fidan Fatma, 2005. Evaluation of the Upper Airway Cross-sectional Area Changes in Different Degrees of Severity of Obstructive Sleep Apnea Syndrome: Cephalometric and Dynamic CT Study. AJNR Am J Neuroradiol 26, 2624-2629.

Zachow S, Muigg P, Hildebrandt T, Doleisch H, Hege H C, 2009. Visual Exploration of Nasal Airflow. IEEE Transactions on Visualization and Computer Graphics 15, 1407-1414.

Zhang G., Solomon P., Rival R., Fenton R. S., Cole P., 2008. Nasal airway volume and resistance to airflow. Am J Rhinol 22, 371-375.

Zhang Zhe, Clement Kleinstreuer, 2003. Low-Reynolds-number turbulent flows in locally constricted conduits: A comparison study. AIAA Journal 41, 831-840.

Zhao K, Scherer P W, Hajiloo S A, Dalton P, 2004. Effect of anatomy on human nasal air flow and odorant transport patterns: implications for olfaction. Chem Senses 29, 365-379.

Zhao Kai, Pribitkin Edmund A, Cowart Beverly J, Rosen David, Scherer Peter W, Dalton Pamela, 2006. Numerical modeling of nasal obstruction and endoscopic surgical intervention: Outcome to airflow and olfaction. American Journal of Rhinology and Allergy 20, 308-316.

Zhu Jian Hua, Lee Heow Pueh, Lim Kian Meng, Lee Shu Jin, Wang De Yun, 2011. Evaluation and comparison of nasal airway flow patterns among three subjects from Caucasian, Chinese and Indian ethnic groups using computational fluid dynamics simulation. Respiratory Physiology & Neurobiology 175, 62-69.

Zoumalan Richard A, Carron Michael A, Tajudeen Bobby A, Miller Philip J, 2009. Treatment of Dorsal Deviation. Otolaryngologic Clinics of North America 42, 579-586.

LIST OF PUBLICATIONS

Journal Articles:

JH Zhu, HP Lee, KM Lim, SJ Lee, DY Wang. 2011. Evaluation and comparison of nasal airway from patterns among three subjects from Caucasian, Chinese and Indian ethnic groups using computational fluid dynamics simulation. Respiratory Physiology & Neurobiology. 175(1): 62-69.

JH Zhu, HP Lee, KM Lim, SJ Lee, LS Teo, DY Wang. 2012. Passive movement of human soft palate during respiration: a simulation of 3D fluid/structure interaction. Journal of Biomechanics. 45: 1992-2000.

JH Zhu, HP Lee, KM Lim, BR Gordon, DY Wang. 2012. Effect of accessory ostia on maxillary sinus ventilation: a computational fluid dynamics (CFD) study. Respiratory Physiology and Neurobiology. 183: 91-99.

JH Zhu, HP Lee, KM Lim, SJ Lee, LS Teo, DY Wang. 2012. Inspirational airflow patterns in deviated noses: a numerical study. Computer Methods in Biomechanics and Biomedical Engineering. In press. DOI: 10.1080/10255842.2012.670850

Conference Presentations:

JH Zhu, HP Lee, KM Lim, DY Wang, SJ Lee, TC Lim. A Comparison of post-operational nasal patency after open reduction internal fixation and closed reduction with internal fixation using computational fluid dynamics. CMBBE, Feb, 2010, Spain.

JH Zhu, HP Lee, KM Lim, DY Wang, SJ Lee. Evaluation and comparison of nasal airway flow patterns among Caucasian, Indian, Chinese and Malay ethnic groups using Computational Fluid Dynamics Simulation. WCB, Aug, 2010, Singapore.

HP Lee, **JH Zhu**, KM Lim, SJ Lee, LS Teo, DY Wang, Airflow ventilation through human maxillary sinuses with single/twin accessory ostia: a CFD simulation study. CMBBE, April, 2012, Germany.